SCIENCE & TECHNOLOGY

ARS JOURNAL

A PUBLICATION OF THE AMERICAN ROCKET SOCIETY

VOLUME 30 NUMBER 9 SEPTEMBER 1960

LOS ANGELES PUBLIC LIBRARY

OCT 3 - 19

CONTRIBUTED ARTICLES

Particle Impacts on the Melt Layer of an Ablating Body . . . . E. W. Ungar 799

Ablation of Glassy Material Around Blunt Bodies of Revolution . . . . Henry Hidalgo 806

Materials for Re-Entry Heat Protection of Satellites . . . . Leo Steg 815

Analysis of the Ablation of Plastic Heat Shields That Form a Charred Surface Layer . . . . R. J. Barriault and J. Yos 823

Measurements of Heat Transfer and Friction Coefficients for Helium Flowing in a Tube at Surface Temperatures up to 5900 R . . . . Maynard F. Taylor and Thomas A. Kirchgessner 830

Controlled Recovery of Nonlifting Satellites . . . . R. W. Dutra, F. R. Riddell and P. H. Rose 892

BIND

TECHNICAL NOTES

Escape in the Equatorial Plane of an Oblate Planet . . . . Maurice L. Anthony and George E. Fosdick 898

Geodetic Latitude and Altitude of a Satellite . . . . W. J. Berger and J. R. Ricupito 901

Terminal Guidance Technique for Satellite Interception Utilizing a Constant Thrust Rocket Motor . . . . Martin L. Nason 902

Extension of the Transient Heating Charts . . . . A. N. Baxter 904

Stability of Some Potential Rocket Fuels in the Molten State . . . . R. P. Rastogi, R. K. Nigam and Harbans Lal 905

Insulation Temperature for the Transient Heating of an Insulated Infinite Metal Slab . . . . William H. Heiter and John H. Grover 907

Acoustic Instability in Solid Fuel Rockets . . . . F. T. McClure, R. W. Hart and J. F. Bird 908

DEPARTMENTS

Technical Comments 910

Book Reviews 912

Technical Literature Digest 916

RUSSIAN SUPPLEMENT 833-888

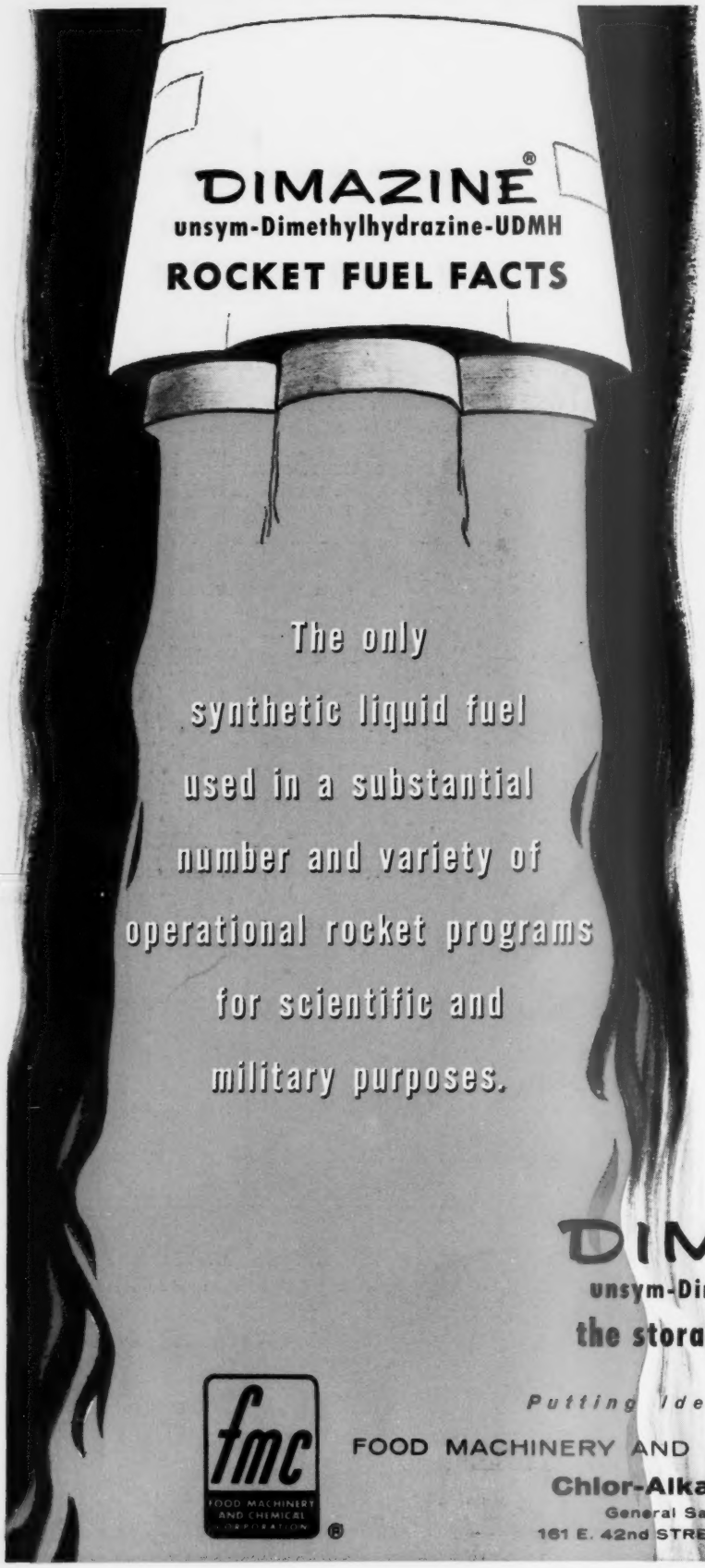
DIMAZINE®
unsym-Dimethylhydrazine-UDMH
ROCKET FUEL FACTS
The only synthetic liquid fuel used in a substantial number and variety of operational rocket programs for scientific and military purposes.

and here are some of the many reasons why:

OUTSTANDING ALL-ROUND PERFORMANCE

- Fast, reliable hypergolic ignition with most storable and high-energy oxidants
- Smooth, safe starting and shut-down transients
- Excellent combustion stability
- High resistance to liquid-phase decomposition and vapor detonation in injectors, coolant tubes
- High specific impulse:

355	80/20 Fluorine/LOX
344	Fluorine
310	LOX
290	Perchloryl Fluoride
286	Nitrogen Tetroxide
282	98% Hydrogen Peroxide
280	Chlorine Trifluoride
276	IRFNA

(Theoretical I_{sp}, sec—1,000/14.7 psia, optimum expansion, shifting equil.)

- Excellent efficiency, high *actual* I_{sp}
- Low viscosity, good pumping and fluid-flow properties
- High heat capacity, good coolant characteristics
- Density comparable to hydrocarbon fuels

PLUS

- Outstanding storability
- Ease of handling
- Simplified equipment design and conversion from other fuels
- Extensive background of testing and operational experience
- Rapidly expandable production to meet large-scale requirements

DIMAZINE
unsym-Dimethylhydrazine-UDMH
the storable high energy fuel

Putting Ideas to Work

FOOD MACHINERY AND CHEMICAL CORPORATION
Chlor-Alkali Division
General Sales Offices:
161 E. 42nd STREET, NEW YORK 17

fmc
FOOD MACHINERY AND CHEMICAL CORPORATION
®

CREATIVE ELECTRONICS FOR DEFENSE

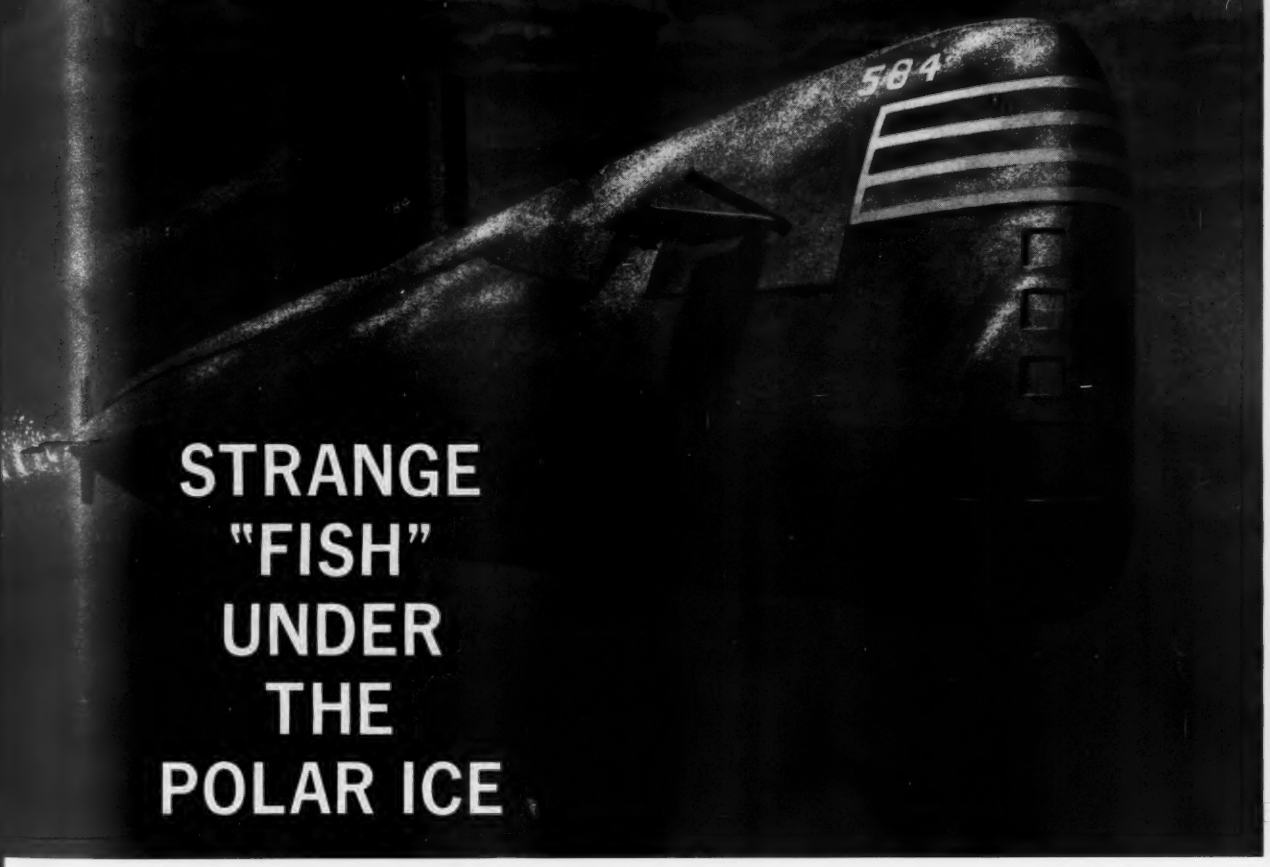

STRANGE "FISH" UNDER THE POLAR ICE

Revolutionary RCA Magnetic Video Tape Recorder to Speed Navigation Training of Submariners

Aboard the nuclear submarine Sea Dragon, the first undersea magnetic video tape recorder will record and store data on under-the-ice characteristics from externally installed TV cameras. Upon return to base the recorded information will be displayed for the benefit of undersea service trainees.

The RCA undersea recorder is a marvel of compact design (dimensions 20" x 20" x 100"). It nestles in a torpedo rack, and represents a 60% space reduction over existing video tape equipment.

Among the exclusive RCA developments are: the now famous "Tiros" satellite recorder; a radar system designed to take the first pictures of a nose cone re-entry vehicle; a unique tape cartridge completely adaptable to any size recorder. For literature describing new RCA defense and commercial products developments, write Defense Electronic Products, Radio Corporation of America, Camden, N. J.

Out of today's defense needs...tomorrow's electronic advances

RCA®

The Most Trusted Name in Electronics

RADIO CORPORATION OF AMERICA

ARS JOURNAL

A PUBLICATION OF THE AMERICAN ROCKET SOCIETY

EDITOR — Martin Summerfield

ASSOCIATE TECHNICAL EDITOR — Irvin Glassman

MANAGING EDITOR — Barbara Nowak

ART EDITOR — John Culin

ASSOCIATE EDITORS

Ali Bulent Cambel, *Northwestern University, Book Reviews;* **Igor Jurkevich,** *G. E. Space Sciences Laboratory, Russian Supplement;* **George F. McLaughlin,** *Patents;* **Charles J. Mundo Jr.,** *Raytheon Co., Guidance;* **Bernard H. Paiewonsky,** *Aeronautical Research Associates of Princeton, Flight Mechanics;* **M. H. Smith,** *Princeton University, Technical Literature Digest*

ASSISTANT EDITORS

Julie Hight, Carol Rubenstein, Estelle Viertel

ADVERTISING PRODUCTION MANAGER

Walter Brunke

ADVERTISING REPRESENTATIVES

New York
D. C. Emery and Associates
400 Madison Ave., New York, N. Y.
Telephone: Plaza 9-7460

Los Angeles
James C. Galloway and Co.
6535 Wilshire Blvd., Los Angeles, Calif.
Telephone: Olive 3-3223

Chicago
Jim Summers and Associates
35 E. Wacker Dr., Chicago, Ill.
Telephone: Andover 3-1154

Detroit
R. F. Pickrell and Vincent Purcell
318 Stephenson Bldg., Detroit, Mich.
Telephone: Trinity 1-0790

Boston
Robert G. Melendy
17 Maugus Ave., Wellesley Hills, Mass.
Telephone: Cedar 5-6503

Pittsburgh
John W. Foster
239 4th Ave., Pittsburgh, Pa.
Telephone: Atlantic 1-2977

American Rocket Society

500 Fifth Avenue, New York 36, N. Y.

Founded 1930

OFFICERS

President	Howard S. Seifert
Vice-President	Harold W. Ritchey
Executive Secretary	James J. Harford
Treasurer	Robert M. Lawrence
General Counsel	Andrew G. Haley
Director of Publications	Irwin Hersey

BOARD OF DIRECTORS

Terms expiring on dates indicated

Ali B. Cambel	1962	William H. Pickering	1961
Richard B. Canright	1962	Simon Ramo	1960
James R. Dempsey	1961	William L. Rogers	1960
Herbert Friedman	1962	David G. Simons	1961
Robert A. Gross	1962	John L. Sloop	1961
Samuel K. Hoffman	1960	Martin Summerfield	1962
A. K. Oppenheim	1961	Wernher von Braun	1960
Maurice J. Zucrow	1960		

TECHNICAL COMMITTEE CHAIRMEN

G. Daniel Brewer, Solid Rockets
Ali B. Cambel, Magnetohydrodynamics
William H. Dorrance, Hypersonics
James S. Farrior, Guidance and Navigation
Herbert Friedman, Physics of the Atmosphere and Space
George Gerard, Structures and Materials
Martin Goldsmith, Liquid Rockets
Andrew G. Haley, Space Law and Sociology
Samuel Herrick, Astrodynamics
Maxwell W. Hunter, Missiles and Space Vehicles
David B. Langmuir, Ion and Plasma Propulsion
Max A. Lowy, Communications
Irving Michelson, Education
Peter L. Nichols Jr., Propellants and Combustion
Eugene Perchonok, Ramjets
Richard A. Schmidt, Test, Operations and Support
C. J. Wang, Nuclear Propulsion
Stanley C. White, Human Factors and Bioastronautics
George F. Wislicenus, Underwater Propulsion
John E. Witherspoon, Instrumentation and Control
Abe M. Zarem, Power Systems

Scope of ARS JOURNAL

This Journal is devoted to the advancement of astronautics through the dissemination of original papers disclosing new scientific knowledge and basic applications of such knowledge. The sciences of astronautics are understood here to embrace selected aspects of jet and rocket propulsion, spaceflight mechanics, high speed aerodynamics, flight guidance, space communications, atmospheric and outer space physics, materials and structures, human engineering, overall system analysis, and possibly certain other scientific areas. The selection of papers to be printed will be governed by the pertinence of the topic to the field of astronautics, by the current or probable future significance of the research, and by the importance of distributing the information to the members of the Society and to the profession at large.

Information for Authors

Manuscripts must be as brief as the proper presentation of the ideas will allow. Exclusion of dispensable material and conciseness of expression will influence the Editors' acceptance of a manuscript. In terms of standard-size double-spaced typed pages, a typical maximum length is 22 pages of text (including equations), 1 page of references, 1 page of abstract and 12 illustrations. Fewer illustrations permit more text, and vice versa. Greater length will be acceptable only in exceptional cases.

Short manuscripts, not more than one quarter of the maximum length stated for full articles, may qualify for publication as Technical Notes or Technical Comments. They may be devoted to new developments requiring prompt disclosure or to comments on previously published papers. Such manuscripts are published within a few months of the date of receipt.

Sponsored manuscripts are published occasionally as an ARS service to the industry. A manuscript that does not qualify for publication, according to the above-stated requirements as to subject, scope or length, but which nevertheless deserves widespread distribution among jet propulsion engineers, may be printed as an extra part of the Journal or as a special supplement, if the author or his sponsor will reimburse the Society for actual publication costs. Estimates are available on request. Acknowledgment of such financial sponsorship appears as a footnote on the first page of the article. Publication is prompt since such papers are not in the ordinary backlog.

Manuscripts must be double spaced on one side of paper only with wide margins to allow for instructions to printer. Include a 100 to 200 word abstract. State the authors' positions and affiliations in a footnote on the first page. Equations and symbols may be handwritten or typewritten; clarity for the printer is essential. Greek letters and unusual symbols should be identified in the margin. If handwritten, distinguish between capital and lower case letters, and indicate subscripts and superscripts. References are to be grouped at the end of the manuscript and are to be given as follows. For journal articles: Authors first, then title, journal, volume, year, page numbers; for books: Authors first, then title, publisher, city, edition and page or chapter numbers. Line drawings must be clear and sharp to make clear engravings. Use black ink on white paper or tracing cloth. Lettering should be large enough to be legible after reduction. Photographs should be glossy prints, not matte or semi-matte. Each illustration must have a legend; legends should be listed in order on a separate sheet.

Manuscripts must be accompanied by written assurance as to security clearance in the event the subject matter lies in a classified area or if the paper originates under government sponsorship. Full responsibility rests with the author.

Preprints of papers presented at ARS meetings are automatically considered for publication.

Submit manuscripts in duplicate (original plus first carbon, with two sets of illustrations) to the Managing Editor, ARS JOURNAL, 500 Fifth Avenue, New York 36, N.Y.

ARS JOURNAL is published monthly by the American Rocket Society, Inc. and the American Interplanetary Society at 20th & Northampton Sts., Easton, Pa., U. S. A. Editorial offices: 500 Fifth Ave., New York 36, N. Y. Price: $12.50 per year, $2.00 per single copy. Second-class postage paid at Easton, Pa., with additional entry at New York, N. Y. This publication is authorized to be mailed at the special rates of postage prescribed by Section 132.122. Notice of change of address should be sent to the Secretary, ARS, at least 30 days prior to publication. Opinions expressed herein are the authors' and do not necessarily reflect the views of the Editors or of the Society.

© Copyright 1960 by the American Rocket Society, Inc.

The Air Force Missile Family...Scions of Space Technology

Science and technology, especially as they relate to missile art, have advanced further in the last six years than in the preceding six centuries. Any review of the many milestones successfully attained since 1954 reveals an epic of hard work, inventiveness, accomplishment, and singleness of objective. This single objective—the achievement of operational weapon capability at the earliest possible date—is being realized.

The Air Force missile family including Atlas, Thor, Titan, and Minuteman, has achieved progress beyond expectation in a program unmatched for magnitude and complexity.

Space Technology Laboratories has had the responsibility since 1954 for the over-all systems engineering and technical direction of these programs. STL's scientific and technical management capabilities have not only helped to hasten the day of operational capability for Air Force ballistic missiles, but have also been applied in carrying out related space probe and satellite projects.

Scientists and engineers with outstanding qualifications find unusual opportunities for their skills and disciplines at STL. Positions on STL's technical staff are now available for those who wish to add a new dimension to their careers. Resumes and inquiries are invited.

SPACE TECHNOLOGY LABORATORIES, INC.

P. O. Box 95004, Los Angeles 45, California • STL Florida offers immediate opportunities to outstanding Assistant Test Supervisors. Write: Mr. George S. Cherniak, STL, P. O. Box 4277, Patrick Air Force Base, Florida

Announcing the formation of AEROSPACE CORPORATION a new and vital force engaged in accelerating the advancement of space science and technology

Aerospace Corporation has been brought into being to serve the United States government by concentrating the full resources of modern science and technology on rapidly achieving those advances in space systems indispensable to the national security.

The corporation is non-profit, will share the findings of its research and laboratory experiments with all appropriate organizations involved in the government's missile-space program, and is not organized for manufacturing purposes.

The immediate responsibility of Aerospace Corporation is to aid the United States Air Force in bringing about the best possible ballistic missiles and military space systems on a continuing basis and within the shortest possible time.

In addition, it may furnish the National Aeronautics and Space Administration and other governmental agencies appropriate services whenever its participation in space exploration and related activities is desired.

THE MISSION of Aerospace Corporation, according to the Secretary of the Air Force, encompasses "the field of ballistic missile and space programs. Within this complete area, it has the responsibility for advanced systems analysis, research and experimentation, and initial systems engineering. It will also exercise such general technical supervision of ballistic systems as is appropriate. In special cases, and with the consent of the Secretary of the Air Force, Aerospace Corporation may assume broader responsibility for an Air Force military system."

The new corporation also provides support to the Air Force in its effort to achieve maximum interchange of knowledge with other military services and among universities, research foundations, and the scientific community in general.

THE FUNCTIONS of Aerospace Corporation in carrying out its responsibilities for the Air Force's missile-space programs include the performance of a wide range of scientific, technical, and administrative tasks.

The corporation will conduct extensive laboratory and field activities aimed at advancing the state-of-the-art and will augment these research and development activities by coordination with industry, universities, laboratories, and other agencies. It is intended that this combined effort will push forward the boundaries of technology on a broad front to fulfill military and other national requirements.

Aerospace Corporation will study the application of the advancing technology to military weapons, support systems, and other systems serving the national need. These studies will culminate in preliminary design and in recommendations for development programs.

Aerospace Corporation will then assist the Air Force or other appropriate government agencies in establishing space programs and in bringing the force of American industry to bear in carrying them out. Once development is initiated, Aerospace Corporation will assume responsibilities for the broad technical aspects of these new programs through their critical phases.

THE FACILITIES of Aerospace Corporation include a research and development center located near the Los Angeles International Airport and within easy reach of several attractive residential communities.

They constitute a modern administrative, scientific, and engineering headquarters which house some of the world's most advanced instrumentation and experimental apparatus.

In addition, the operations of Aerospace Corporation will be directly supported around the globe by a vast array of resources created by the government over the past six years. These will include: The Atlantic Missile Range in Florida; The Pacific Missile Range in California; The Rocket Engine Test Site at Edwards Air Force Base in California; and numerous other missile test facilities sponsored by the government in cooperation with private industry.

THE PEOPLE who make up Aerospace Corporation have been selected from industry, universities, and government. They constitute a cross-section of highly-developed engineering and scientific skills in the missile and space fields.

Extensive recruiting will continue as the new corporation assumes more and more responsibility. From the outset, the corporation is built on a foundation of proven scientific competence, imagination, and objectivity.

THE OPPORTUNITY awaiting those scientists and engineers who qualify to join Aerospace Corporation is equalled only by the magnitude of the corporation's mission – magnitude mirrored by the highly advanced nature of the programs in which Aerospace Corporation is engaged.

Typical systems projects include: advanced ballistic missiles; advanced military space boosters; recoverable boosters and satellites; space defense systems; early-warning satellites; reconnaissance satellites; communications satellites; and manned satellite systems.

Typical research programs concern: nuclear propulsion; astrodynamics; magnetohydrodynamics; inertial elements; millimeter waves; hypersonics; combustion kinetics; and materials research.

Those capable of contributing to state-of-the-art advances in these and related areas are invited to consider the advantages of becoming a part of the new Aerospace Corporation. Their resumes should be directed to: Mr. James M. Benning, P. O. Box 95081-I, Los Angeles 45, California.

AEROSPACE CORPORATION 2400 East El Segundo Boulevard • El Segundo, California

AVCO-EVERETT RESEARCH LABORATORY IS EXPANDING

to meet the needs of three major projects

1. **MHD POWER GENERATOR**—In cooperation with 10 leading utilities, AERL is working toward a prototype electrical power generating station using the revolutionary Magnetohydrodynamic technique.
2. **RECOVERABLE SATELLITES**—Under contract with the U.S. Air Force, AERL is developing and flight-testing recoverable satellites based on the unique Avco Drag Brake principle.
3. **ICBM DEFENSE**—AERL's superior background in laboratory and inflight studies of re-entry phenomena is being applied to the vital problem of the design of practical systems for defense against ICBM's, under several contracts with the Department of Defense.

CONTINUING RESEARCH PROGRAM—These expanding projects are results of AERL's basic research effort. To provide general support for existing projects, and to supply new fundamental knowledge for our further growth, we are seeking scientists and research-oriented engineers. In particular, we are looking for: Aerodynamicists with some background in high-temperature gas phenomena, Physicists and Physical Chemists interested in plasma and associated high-temperature gas phenomena.

Avco EVERETT RESEARCH LABORATORY

TO SPEED THESE PROJECTS, WE ARE SEEKING:

Aerodynamicists—Theoretical & Experimental
Senior Rocket Combustion Engineers
Mechanical Engineers
Engineering Physicists
Systems Engineers
Flight Test Specialists
Electronic & Electrical Engineers
Communications & Telemetry Specialists
Physicists—Theoretical & Experimental
Aeronautical Engineers
Missile and Satellite Designers
Physical Chemists
Flight Control Specialists

FOR FURTHER INFORMATION

write to:
Mr. R. E. McDonald,
Avco-Everett
Research Laboratory,
Everett, Massachusetts.

Particle Impacts on the Melt Layer of an Ablating Body[1]

E. W. UNGAR[2]

Battelle Memorial Institute
Columbus, Ohio

An analysis has been made of the effects of high velocity particle impacts on a melting body, such as might occur if atmospheric particles are encountered during atmospheric entry. The surface material considered in the analysis is a composite of glass and a plastic which evolves a large quantity of gas. An equation is developed relating the increase in erosion rate, as a result of particle impacts, to flight and material parameters. It was assumed in the derivation that the liquid melt layer protects the underlying solid body by decelerating the particles. The extent of the melt layer protection was found to be dependent on the particle size and melt layer thickness. One experimental check on the analysis was possible by inspection of the order of magnitude of the experimental liquid melt layer thickness on fired Micarta specimens. The computed melt layer thickness agreed with that observed on glass-reinforced Micarta 259-2 test specimens which were exposed in a rocket exhaust jet. Finally, it was assumed that the effect of the particle impacts was to transfer energy to the plastic, thus increasing the decomposition rate of the plastic filler in Micarta 259-2. It was possible to compute erosion rates, based on this analysis, which were in agreement with experimental results. The analysis shows that the particle impacts influence the thermal energy transfer to the body.

A VEHICLE entering a planetary atmosphere will be subject to extreme heating. The extent of this heating, which results from dissipation of vehicle potential and kinetic energy, is dependent on initial entry velocity, nature of the atmosphere, gravitational attraction of the planet and the weight to drag ratio of the vehicle. Entry into the atmospheres of Mercury and Mars will be less severe than entry into Earth's atmosphere. Entry into the atmosphere of Venus is comparable with entry into Earth's atmosphere; whereas entry into the Jovian atmospheres will probably be much more severe. In order to relieve aerodynamic heating, the leading edges of the vehicles used for missions requiring atmospheric entry will usually be blunted so that a large amount of the vehicle energy will be dissipated by heating the gas behind a detached shock wave. However, there still may be sufficient energy transferred to the body from the hot gas behind the detached shock wave to vaporize most materials. Thus, a thermal protection system is required so that the interior of the vehicle remains at a sufficiently low temperature to allow operation of equipment and the well-being of passengers. Past experience with ballistic missiles has shown that ablating materials are practical and reliable for use in thermal protection systems.

There are at present many uncertainties with regard to the exact nature of the various planetary atmospheres. Atmospheric moisture particles in the form of clouds and rain are present in Earth's atmosphere. There is evidence of moisture in the atmospheres of Venus and Mars (1).[3] A layer of minute matter exists between 35,000 and 50,000 ft in the Martian atmosphere; this matter is likely to be ice crystals. There is also the strong possibility of the presence of significant quantities of dust in the atmospheres of Venus and Mars. The Martian dust may be in the form of dust clouds. Thus, in addition to the purely theemal consideration of atmospheric entry, some thought must be given to the effects produced by the impact of high velocity vehicles upon atmospheric particles. These impacts are likely to occur during the aerodynamic heating phase of the entry mission. The effect of these impacts might be to increase the ablation rate to such an extent that the interior temperature of the vehicle would exceed the limit allowed for personnel or equipment. Furthermore, the increased rate of ablation might occur at locations where only small amounts of material loss would otherwise be expected. In an extreme situation, the geometry of the vehicle might be altered sufficiently by particle impacts to affect the flight path. In the other extreme, if the particles are composed of water, it is possible that the effect of the particles might be to cool the surface, resulting in a net decrease in the ablation rate.

This paper presents the results of a study of the impact of small particles on ablating bodies. The experimental approach and test results are briefly outlined. The impact phenomenon is then analyzed, and the experimental data correlated with the proposed theory. Finally, implications of the study with respect to atmospheric entry vehicles are briefly discussed.

General Research Procedure

The extent of the damage that might be caused by impact of a melting aerodynamic surface with suspended particles during an atmospheric entry is influenced by a number of variables. Among these variables are particle size, particle density, impact velocity, surface material and surface condi-

---

Presented at the ARS Structural Design of Space Vehicles Conference, Santa Barbara, Calif., April 6–8, 1960.

[1] The investigation reported herein was carried out for the Army Ballistic Missile Agency under Contract DA-33-019-ORD-2774.

[2] Principal Mechanical Engineer, Aeronautics and Thermodynamics Division. Member ARS.

[3] Numbers in parentheses indicate References at end of paper.

tion. In addition to these variables, there are additional variables associated with the effects of the shock wave and shock layer gas on the particles, namely, particle deceleration and deflection, particle deformation and particle evaporation. An investigation of the effects of the shock layer gas on moisture particles has shown that, for a first-order approximation, they may be neglected in the case of a vehicle entering Earth's atmosphere (2). Therefore, the effects of the shock layer gas on the particles are not considered in this paper.

Although perfect simulation of all pertinent variables is not feasible in a ground test facility, a reasonable approximation of the pertinent variables can be obtained in a rocket engine test facility. Rocket engines provide a stream of high velocity, high temperature gas into which particles may be introduced. High stagnation temperatures, of the order of 3000 to 6000 R, are easily obtained through the release of chemical energy within the combustion chamber. Although these temperatures may in some cases be lower than those at the atmospheric entry condition being simulated, they are high enough to melt most materials. Exhaust Mach numbers between 2 and 4 are obtainable at reasonable chamber pressures for sea-level operation. Although the Mach number in a rocket engine exhaust at sea level is generally not as high as those experienced by a vehicle entering an atmosphere, it is sufficiently high to produce a flow, geometrically similar to that obtained in flight, about a properly located blunt body. The initial relative velocity between the particle and the shock layer gas will usually be less in the rocket engine facility than in flight, since rocket engine exhaust velocities are of the order of 7000 fps at sea level, resulting in particle velocities less than 7000 fps. Energy and momentum considerations, therefore, require particles of greater mass than atmospheric particles.

In summary, when the effect of the high velocity particles on a melting body is considered, a rocket engine test facility shows appreciable merit. Although impact velocities are not so great as those which might occur in flight, the particle energy or momentum can be simulated by adjusting the particle density. Furthermore, the stagnation temperatures and heat fluxes available in a rocket engine exhaust jet are high enough to maintain a reasonable test specimen thermal ablation rate. By controlling the size of the particles used in the experiment, it is possible to maintain the relationship between particle size and melt layer thickness required for simulation. Solid or liquid particle impacts might be obtained by varying combustion temperature or particle material.

To gain some understanding of the physical phenomena associated with the impact of high velocity particles on an ablating body, experiments were conducted at the Army Ballistic Missile Agency. The facility used in these studies was the ABMA 3.5 AHT rocket engine. This engine burns a mixture of kerosene and hydrogen peroxide and is designed so that a slurry of additional kerosene and fine particle can be injected directly into the combustion chamber. The particles are accelerated by the hot exhaust gases and impact on test specimens.

Fused aluminum oxide particles were used in a large number of the tests in the 3.5 AHT exhaust. Since these particles remain solid during passage through the engine, they were used to simulate the impacts of solid ice particles. Particles composed of a low-melting-point glass were used in the remainder of the tests. The glass particles melted in the exhaust jet and thus simulated the impact of liquid droplets.

Micarta 259-2 is the material studied most extensively under this program, since it is considered to be typical of the thermal shield materials used on some atmospheric entry vehicles. Thermal ablation of Micarta in the 3.5 AHT exhaust took place as a result of the melting of the glass laminates and the decomposing of the melamine resin filler. The melting glass resulted in the generation of a thin layer of flowing molten glass on the surface of the specimen, whereas the thermal decomposition of the plastic filler resulted in the blowing of gaseous decomposition products through this molten glass into the gaseous boundary layer.

Experimental Results

The exposed surfaces of the specimens were first studied under a binocular microscope using powers of magnification from 2 to 150×. Comparisons were made between specimens which were fired both with and without particles in the hot gas stream. Particles could not be identified by this type of examination. The solidified melt was observed to become more dense as the particle exposure became more severe. Some unmelted glass fibers could be seen in the melt layer on specimens exposed to particle impact; this was not observed on control specimens fired without particles.

Samples were scraped from the melted layers of representative specimens and analyzed microscopically. Samples from the specimens impacted by aluminum oxide particles showed aluminum oxide was present in the melt as discrete particles. The index of refraction of the melt was only slightly affected by the presence of the oxide. In addition, the size of the alumina particles found in the samples were measured, and it was found that the average size of these particles was less than the original size by 35 to 50 per cent. Cracks were also noticed in these alumina particles. The inferences to be drawn from these observations are that:

1 The alumina did not melt in the rocket engine.

2 Many of the particles fractured on impact.

Thus, it is felt that solid particle impacts were adequately simulated by alumina in the 3.5 AHT facility.

Samples taken from the melt layer of specimens which had been impacted by the low-melting-point glass particles in the 3.5 AHT facility were examined. These examinations showed that particle melting had occurred prior to impact on the specimens during the tests. It is to be recalled that liquid particle impacts were desired so as to provide simulation of liquid-water impact. The reason for believing that the glass particles impinged on the specimens while in the liquid state is that the microscopic examination indicated an intimate mixing of the glass from the Micarta and the glass particles. If the particles had struck the surface as solids, then the last particles to impact as the specimen was removed from the test would be found as discrete particles. The melt layer on the specimens impacted by glass particles had indexes of refraction which were consistently less than either the index of refraction of the glass particles prior to the tests or the index of refraction of the melt on a specimen which was not exposed to particle impact. The decreased index of refraction is believed to be the result of some volatilization of the lead and boron constituents of the mixed glasses.

In addition, observations of cross sections of the melt on several specimens were made. The cross sections were obtained by cutting the specimens with a diamond saw. Melt thicknesses were found to be generally of the order of 70 μ. A charred layer was beneath the melt; its thickness was three to five times the melt thickness and generally thicker on specimens that were hit with particles. The particles might carry energy deeper into the body than would normal thermal conduction. Microscopic examination of samples scraped from the charred layer showed the presence of aluminum oxide particles in the charred layer of those specimens which had been impacted on by aluminum oxide particles.

Fig. 1 shows magnifications of the cross section through two typical test specimens. The melt layer on the specimen exposed to particle impact is considerably more nonuniform than the one on the specimen not exposed to particles. This is believed to occur during cooling. The melt is probably relatively uniform in thickness during the test; however,

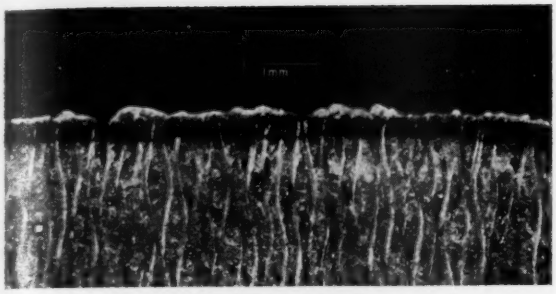

a No particles

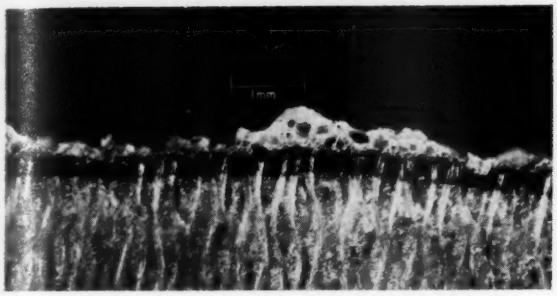

b 0.625 per cent concentration of 7.6-μ glass particles

Fig. 1 Cross sections through melt layer on specimens

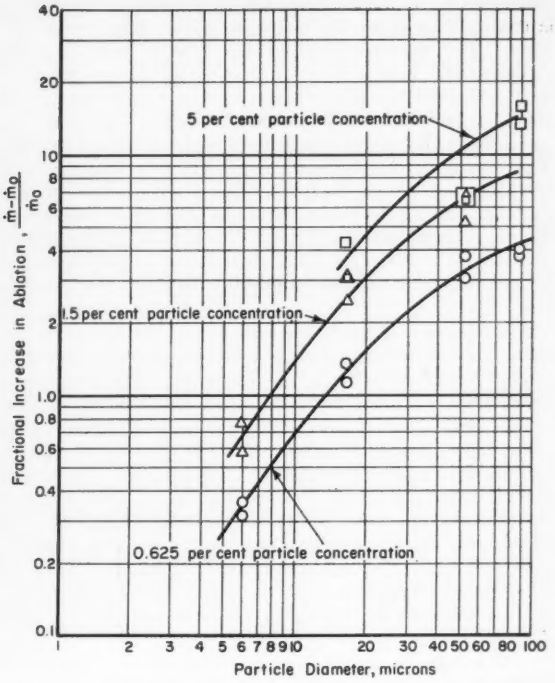
5 per cent particle concentration
1.5 per cent particle concentration
0.625 per cent particle concentration
Fractional Increase in Ablation, $\frac{\dot{m}-\dot{m}_0}{\dot{m}_0}$
Particle Diameter, microns

Fig. 2 Fractional increase in ablation rate for test specimens and aluminum oxide particles

the melt layer on the specimen exposed to particles is probably thicker than on the control specimen during exposure. Several unmelted glass fibers can be seen on the specimen which was exposed to the particle-laden gas stream.

Fig. 2 shows the fractional increase in ablation rate due to particle impacts as a function of particle diameter for the Micarta test specimens hit by aluminum oxide particles. For each test the ablation rate obtained with particles $\dot{m}$ was normalized with respect to the ablation rate with no particles $\dot{m}_0$ corresponding to the conditions of motor operation used for that test. Two different severities of test were utilized, yielding $\dot{m}_0$ values differing by 50 per cent. The additional erosion resulting from particle impacts is seen to increase in a nonlinear manner with both increasing particle size and increasing particle concentration. Fig. 3 shows the particle impact velocity as a function of size calculated for conditions in the 3.5 AHT experiments. It shows that the absolute particle velocity decreases with increasing particle size. Therefore the total energy and momentum transport for a fixed weight concentration of particles decreases with increasing particle size. Thus, at first glance, an increase in the particle size with a fixed weight concentration of particles would not be expected to cause an increase in ablation rate. Fig. 2, however, shows that an increase in ablation rate was obtained with the larger particle sizes. This cannot be explained solely on the basis of an increasing impaction efficiency with increasing particle size, because it has been shown that the impaction efficiency in these tests was close to 100 per cent (2). Extremely large variations in impaction efficiency would be required to explain the results shown in Fig. 2.

The cause of the nonlinear variation of the ablation rate with concentration was also not immediately apparent, since both particle energy and momentum transport vary in a linear manner with particle concentration. These experimental data are discussed further in the next section.

Correlation of Data

A melt protection mechanism is proposed to explain the results presented in the previous section. In some respects the proposed protection mechanism is similar to the protection offered by thermal ablation. The mechanism is such that an increase in the ablation rate resulting from particle impact results in a thicker melt layer. This thicker melt layer offers resistance to the particle and decelerates it, thus decreasing the impact energy and momentum of the particle as it strikes the solid underlying surface. A correlating equation based on this mechanism is developed.

During the course of analysis based on the melt protection mechanism, it was found that the particle kinetic energy which is not dissipated in the liquid melt layer may be

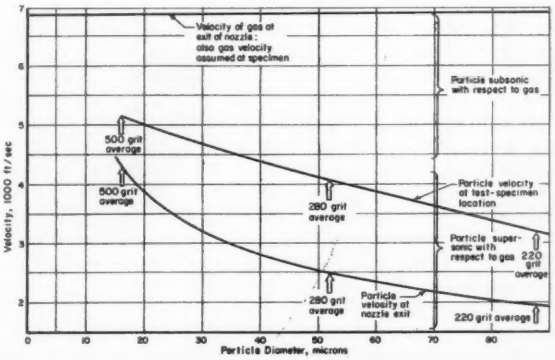
Velocity of gas at exit of nozzle; also gas velocity assumed at specimen
Particle subsonic with respect to gas
500 grit average
500 grit average
280 grit average
Particle velocity at test-specimen location
Particle supersonic with respect to gas
220 grit average
280 grit average
Particle velocity at nozzle exit
220 grit average
Velocity, 1000 ft/sec
Particle Diameter, microns

Fig. 3 Variation of particle velocity with particle diameter in the 3.5 AHT exhaust jet

accounted for if it is assumed that a fraction of this energy is used to decompose the melamine plastic filler in the Micarta. The decomposition of the plastic results in the evolution of a large quantity of gas. This gas has an effect on the thermal flux into the body. The energy required of the particles is only that necessary to start the melamine decomposition, because the decomposition itself is exothermic. The fraction of the impact energy which is transferred to the melamine plastic filler depends on the probability of a particle striking it rather than on the glass reinforcing fibers. This means of accounting for particle energy can be checked because the energy dissipated in the melt layer can be computed independently of any particular failure assumption.

After passing through the melt layer, the energy of the particle is not sufficient to melt all of the glass fiber material eroded from the surface of the specimen. The microscopic observation disclosed the presence of unmelted glass fibers in the melt. The quantity of unmelted glass found in the melt region generally increased as the severity of particle erosion increased. This observation supports the theory that the particles break down or decompose the melamine. Additional support comes from the observation that the layer of charred plastic on fired test specimens was generally thicker when the specimen was hit by particles. The particles might extend the decomposition of melamine to greater depths than would ordinarily be accounted for by heat transfer.

The system to be analyzed is characterized schematically in Fig. 4.

The total ablation rate $\dot{m}$ is given by

$$\dot{m} = \dot{m}_1 - \dot{m}_{\text{stored}} \qquad [1]$$

A quasi-static state is assumed; that is, the melt thickness is assumed not to be a function of time. The origin of the coordinate system is assumed to be on the solid surface and thus recedes with the surface during ablation. For the quasi-static state the simplification

$$\dot{m}_{\text{stored}} = 0$$

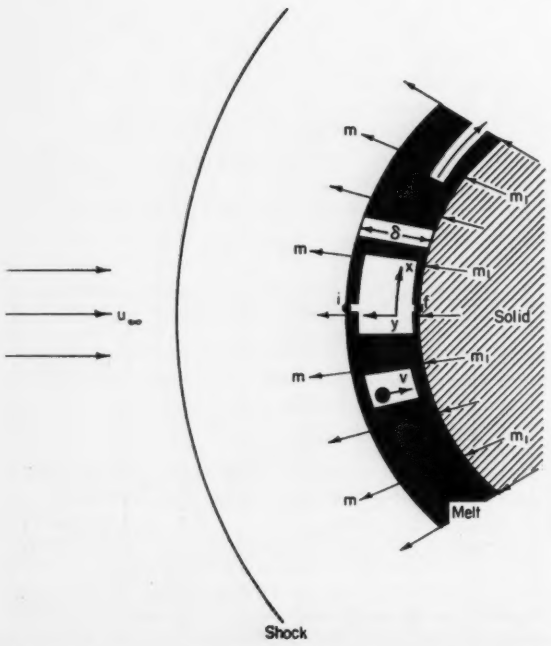

Fig. 4 Schematic model of the ablating system. Dimensions in the y direction are magnified

may be applied to the ablating system. Therefore, for the quasi-static state

$$\dot{m} = \dot{m}_1$$

It is now assumed that $\dot{m}_1$ may be divided into two components, a mass loss due to particle erosion and a mass loss due to thermal failure of material. Therefore

$$\dot{m} = \dot{m}_p + \dot{m}_{th} \qquad [2]$$

On the basis of the assumed failure mechanism for the reinforced plastic the following energy balance may be written

$$Hf\dot{m}_p = F\,(KE)_{\text{impact}}$$

where F, the fraction of the particle impact kinetic energy transmitted to the plastic filler, may be taken as the volume fraction of plastic material in the composite reinforced plastic. Thus, F is essentially the probability of an impacting particle directly impinging on the plastic as opposed to the glass laminates.

The energy balance may be rewritten as

$$Hf\dot{m}_p = \frac{1}{2} F \frac{w_p}{g_c J} \eta V_f^2$$

Rearrangement yields

$$\dot{m}_p = (F/2g_cHf)\eta w_p V_f^2 \qquad [3]$$

The impact velocity at the solid surface must now be found as a function of the melt layer thickness δ and the initial particle velocity V_i. It is assumed that the particle passes through the melt layer before the cavity it forms as a wake has time to close. This last assumption is consistent with the order of magnitude of the melt thickness observed during the microscopic analysis of specimens. The particle velocity V is assumed to be normal to the surface of the body and not to vary with distance from the stagnation point. Newton's law

$$F_p = \frac{d}{dt}(m_p V)$$

becomes for this case of cavity flow

$$\left(\frac{\pi d_p^2}{4}\right)\left(\rho_L \frac{V^2}{2}\right) = \rho_p \frac{\pi d_p^3}{6} \frac{dV}{dt}$$

Algebraic manipulation yields

$$\frac{dV}{dt} = \frac{3}{4} \frac{\rho_L}{\rho_p} \frac{V^2}{d_p} \qquad [4]$$

Equation [4] can now be written as

$$V \frac{dV}{dy} = \frac{3}{4} \frac{\rho_L}{\rho_p} \frac{V^2}{d_p}$$

or as

$$\frac{dV}{V} = \frac{3}{4} \frac{\rho_L}{\rho_p} \frac{dy}{d_p} \qquad [5]$$

Integration of Equation [5] from V_i to V_f and from $y = \delta$ to $y = 0$ yields

$$V_f/V_i = e^{-3\rho_L\delta/4\rho_p d_p} \qquad [6]$$

The value of V_i will, in most cases, be taken as the free stream velocity of the particle relative to the body. The expression for the material loss due to particle impact may now be written as

$$\dot{m}_p = (F/2g_c\,JHf)\eta w_p V_i^2\, e^{-3\rho_L\delta/2\rho_p d_p} \qquad [7]$$

and the total ablation rate is

$$\dot{m} = (F/2g_cJ\ Hf)\eta w_p V_i^2 e^{-3\rho_L\delta/2\rho_p d_p} + \dot{m}_{th} \qquad [8]$$

Expressions relating the melt thickness δ and also $\dot{m}_{th}$ to known parameters are still required. The thermal material loss $\dot{m}_{th}$ will be considered first. Because there is an interaction between the particle impacts and thermal effects, $\dot{m}_{th}$ is not equal to $\dot{m}_0$. It is now assumed that $\dot{m}_{th}$ is equal to the ablation rate $\dot{m}_0$, obtained when no particles are present in the free stream, minus the mass which would have been ablated by the energy used up in heating the gases, resulting from additional decomposition of the plastic, to the mean boundary layer temperature. Thus an interaction between particle and thermal effects is considered. The effect of these additional gases on the boundary layer thickness is not considered. The interaction may be expressed approximately as

$$\dot{m}_{th} = \dot{m}_0 - 0.6\,(T_e - T_f)c_g f\dot{m}_p/H_e \qquad [9]$$

where the 0.6 factor arises from Prandtl number effects in the boundary layer. Substitution of Equation [7] into Equation [9], algebraic manipulation, and finally substitution into Equation [8] yield

$$\dot{m} - \dot{m}_0 = \left[1 - \frac{0.6(T_e - T_f)fc_g}{H_e}\right] \times \frac{F}{2g_c J\ Hf}\,\eta w_p V_i^2 e^{-3\rho_L\delta/2\rho_p d_p} \qquad [10]$$

The only term now remaining to be evaluated in Equation [10] is the average liquid melt thickness δ. It will be assumed that all of the gas generated during the ablation process leaves the melt by flowing in the y direction, and all of the liquid and solid in the melt flows in the x direction. Following the example of Lees (3), the conservation of mass for the melt layer for axially symmetric flow is

$$2\pi r_0(1 - f)\dot{m} = \frac{d}{dx}\left(2\pi r_0 \int_0^\delta \rho_L u_L\, dy\right) \qquad [11]$$

where x is measured along the surface, and y is the coordinate normal to the surface.

For an incompressible liquid melt

$$\int_0^\delta \rho_L u_L\, dy = \Lambda\ \rho_L u_i \delta \qquad [12]$$

where $\Lambda = \frac{1}{2}$ for a linear variation of velocity in the y direction within the melt.

Therefore continuity may be expressed as

$$r_0(1 - f)\dot{m} = (dr_0/dx)\Lambda\rho_L u_i \delta \qquad [13]$$

assuming that for small distances along the melt ρ_L, u_i and δ_0 are not functions of x. This assumption is not considered to be critical because large variations are not expected and because the effect of considering these quantities as variables will tend to cancel when ratios are taken later in this discussion.

For a spherical body

$$r_0 = R \sin\theta \qquad x = R\theta$$

The function dr_0/dx may be expressed as

$$\frac{dr_0}{dx} = \frac{dr_0}{d\theta}\frac{d\theta}{dx}$$

but for a sphere

$$\frac{dr_0}{d\theta} = R\cos\theta \qquad \frac{d\theta}{dx} = \frac{1}{R}$$

which leads to

$$dr_0/dx = \cos\theta$$

The equation of continuity may now be rewritten as

$$R\tan\theta\,(1 - f)\,\dot{m} = \Lambda\rho_L u_i \delta \qquad [14]$$

The common assumption is now adopted that the shear stress is not a function of the melt thickness and would be the same if the melt were not present. This implies a linear velocity gradient in the y direction through the melt. Thus

$$R\tan\theta\,(1 - f)\,\dot{m} = (1/2)\rho_L u_i \delta = \rho_L \bar{u}_L \delta \qquad [15]$$

$$\bar{u}_L = \bar{u}_{L0}\delta/\delta_0 \qquad [16]$$

Substitution of Equation [16] into Equation [15] yields

$$R\tan\theta\dot{m}(1 - f) = \rho_L(\bar{u}_{L0}/\delta_0)\delta^2$$

and solving for δ yields

$$\delta = \sqrt{(1 - f)\,\delta_0\dot{m}R\tan\theta/\rho_L\bar{u}_{L0}} \qquad [17]$$

It may be noted that for the condition of no particles in the free stream

$$R\tan\theta(1 - f)\dot{m}_0 = \rho_L\bar{u}_{L0}\delta_0$$

which may be solved for $\rho_L\bar{u}_{L0}$ to yield

$$\rho_L\bar{u}_{L0} = \dot{m}_0\,(1 - f)\,R\tan\theta/\delta_0 \qquad [18]$$

which may now be substituted in Equation [17] to yield

$$\delta = \delta_0\sqrt{\dot{m}/\dot{m}_0} \qquad [19]$$

An expression has now been obtained for the melt layer thickness which may be substituted into Equation [10] to yield the final result

$$\dot{m} - \dot{m}_0 = \left[1 - \frac{0.6(T_e - T_f)fc_g}{H_e}\right] \times \frac{F}{2g_c J\ Hf}\,\eta w_p V_i^2 e^{\frac{-3\rho_L\delta_0\sqrt{\dot{m}/\dot{m}_0}}{2\rho_p d_p}} \qquad [20]$$

This equation may also be expressed in logarithmic form as

$$\ln\left\{\frac{2g_c J\ Hf(\dot{m} - \dot{m}_0)}{[1 - 0.6(T_e - T_f)fc_g/H_e]\,F\eta w_p V_i^2}\right\} = \frac{-3\rho_L\delta_0\sqrt{\dot{m}/\dot{m}_0}}{2\rho_p d_p} \qquad [21]$$

Equation [21] implies that a semi-log plot of $(\dot{m} - \dot{m}_0)/m_0\eta w_p V_i^2$ as a function of $(\dot{m}/\dot{m}_0)^{1/2}/d_p$ should correlate the data for specimens in the 3.5 AHT exhaust jet for one particle density and for one thermal ablation rate. The negative of the slope of the resulting straight line should be the factor $\rho_p/\rho_L\delta_0$. Knowing this factor for one particle density and thermal ablation rate should allow the determination of the factor for other conditions by adjustment of ρ_p for other particle materials and δ_0 for other thermal ablation rates.

Fig. 5 is the semi-log plot just described. All of the data plotted in Fig. 5 are for specimens which were impacted by alumina particles, $\rho_p = 4$ gm/cc, and the same severity of thermal exposure was used, i.e., the same $\dot{m}_0$. The impaction efficiency η is taken as unity. The correlation of the data shown in Fig. 5 is considered to be good. A slope of -29.1 μ^{-1} is obtained, which yields a value of 77.7 μ-gm/cc for the product $\rho_L\delta_0$. If ρ_L is taken to be of the order of unity, then δ_0 becomes 77.7 μ, which agrees with the order of magnitude of the melt thickness observed on cross sections through specimens. As expected, it is less than the 400 μ mentioned by Sutton (4) for Pyrex glass exposed in a rocket exhaust. The value of δ_0 for Micarta in the 3.5 AHT should be less than that for Pyrex in some other facility because the 3.5 AHT gives relatively low thermal ablation rates and roughly half of the ablated Micarta enters the melt as a gas rather than as a liquid.

The equation used for the correlation of all of the Micarta

data is obtained from rearrangement of Equation [21]. This equation is

$$\frac{\rho_L \delta_0}{\rho_p d_p} = -\ln \left\{ \frac{2 q_c J \; Hf(\dot{m} - \dot{m}_0)}{[1 - 0.6\,(T_s - T_f) f c_0 / H_s]\, F \eta w_p V_i^2} \right\}^{\frac{2}{3}} \left(\frac{\dot{m}}{\dot{m}_0} \right)^{-1/2} = -\ln E_R \quad [22]$$

Equation [22] may be checked for all of the Micarta specimen tests conducted in the 3.5 AHT facility, including the tests wherein glass particles were used. The density of the glass particles is 3 gm/cc instead of the 4 gm/cc for the alumina particles, and the glass particles strike the specimen surface while in the liquid state. The value of $\rho_L \delta_0$ must be adjusted for severity of test utilized.

Fig. 6 shows a plot of the right side of Equation [22] as a function of the inverse of the left side of the equation. The plot is presented on log-log coordinate paper because of the range of $\rho_p d_p / \rho_L \delta_0$ which was tested. Had the left side not been inverted and had the plot been made on semi-log coordinates, a straight line would have been obtained which passes through unity when $\rho_L \delta_0 / \rho_p d_p$ is zero. Instead of this happening, however, the inverse plot of E_R shown in Fig. 6 approaches unity asymptotically as $\rho_p d_p / \rho_L \delta_0$ gets very large. The plot implies that for a fixed impact velocity and flow rate of particles, the ablation rate approaches a constant value as the particle size is increased. This should be expected because it indicates that the effect of the melt layer on the particle energy becomes very small when the particles are larger than some certain size. The variable E_R may be physically interpreted as an energy ratio, being roughly the ratio of particle energy utilized in bringing about failure of material to the particle energy immediately outside the melt layer.

All of the data obtained for specimens in the 3.5 AHT facility were plotted in Fig. 6. The correlation achieved with Equation [22] is considered to be good. The impaction efficiency was taken as 100 per cent, and the value of V_i was taken to be the particle velocity at the specimen location, neglecting deceleration in the shock layer.

The results presented in Fig. 6 show that the effects of the liquid glass and the solid alumina particles on Micarta are of the same type. That is, it does not appear to make any difference whether the particles are liquid or solid when they impact on melting surfaces with high velocities.

Implications of Results

The analysis shows that vehicle velocity, melt thickness, ablation rate and particle size and density are all important factors in the determination of impact damage. Thermal ablation rates less than those encountered during entry into Earth's atmosphere might be encountered during entry into the atmospheres of Venus and Mars. The lower thermal ablation rates, and possibly higher entry velocities, would tend to maximize, relative to an Earth entry, the damage produced by particle impacts.

As a part of the program described in (2), some calculations of impact damage were carried out for ballistic missile trajectories. It is of value to consider the magnitude of the calculated damage, as a frame of reference when considering the damage which might be inflicted on a vehicle entering an atmosphere in which particles are present.

Equation [22] was used to compute the magnitude of the increased erosion due to impacts with cloud elements of a

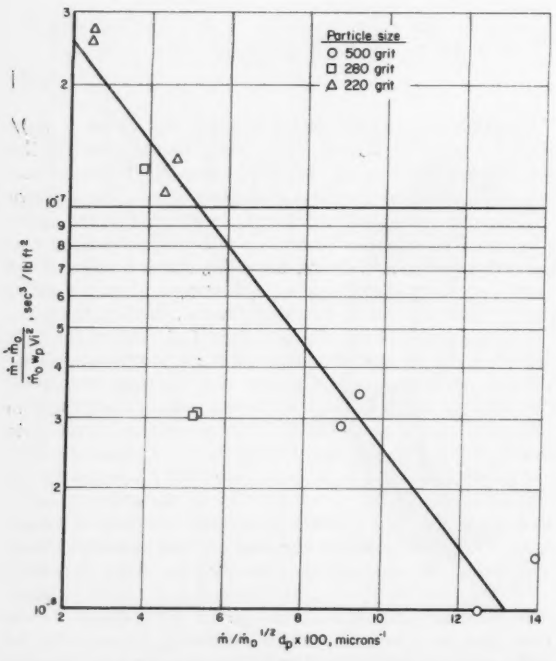

Fig. 5 Correlation of erosion data for specimens impacted by alumina particles at concentrations of 0.625 and 5 per cent and with average sizes of 16, 52 and 88 μ

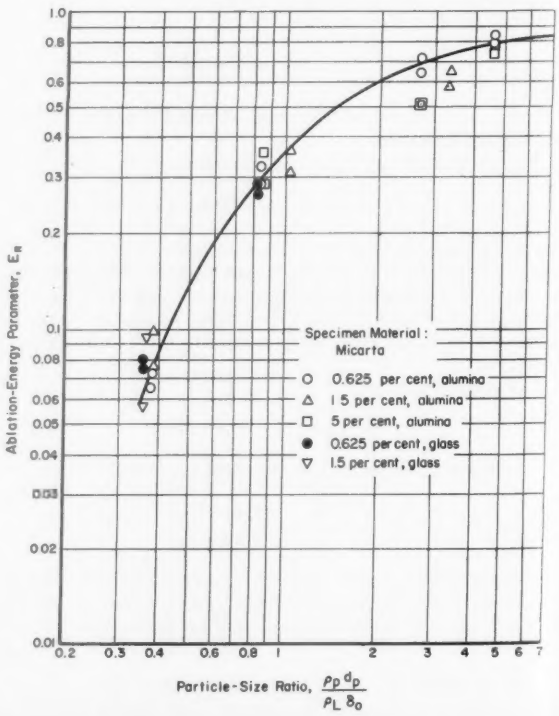
Ablation-Energy Parameter, E_R
Particle-Size Ratio, $\frac{\rho_p d_p}{\rho_L \delta_0}$
Specimen Material : Micarta
○ 0.625 per cent, alumina
△ 1.5 per cent, alumina
□ 5 per cent, alumina
● 0.625 per cent, glass
▽ 1.5 per cent, glass

Fig. 6 Ablation energy parameter as a function of the particle size ratio

body coated with Micarta 259-2 following a ballistic trajectory. The impaction efficiency was taken to be 100 per cent, and particle evaporation and acceleration during passage through the shock layer was neglected. The cooling effect due to the water particles acting as a heat sink was, in most cases, neglected. The calculations indicated an 8 per cent increase in the total mass ablated for the body following a severe re-entry trajectory as a result of flight through a nimbostratus cloud. The cloud altitude was assumed to extend from 2.3 to 10.9 km. The mean particle size was taken to be 13.5 μ and the concentration was taken to be 5×10^2 particles per cc. At one point along a second trajectory which was studied, calculations indicated that the instantaneous ablation rate of the re-entry body may be increased by as much as a factor of 2 during flight through a cloud.

In the case of vehicles entering Earth's atmosphere, the particle impact problem will generally become more severe as the trajectories are changed to include longer periods of time during which hypersonic velocities are maintained at altitudes less than 12 km. This would come about with ballistic missiles having higher weight to drag ratios and with hypersonic low altitude vehicles. Particle impact effects also become more severe as smaller nose radii are utilized for re-entry vehicles. Some of the materials currently being investigated for high heat flux applications do not form a melt layer and therefore might be more vulnerable to particle impact damage than those which do melt during ablation.

In the case of space vehicles entering other planetary atmospheres, the magnitude of the particle damage may be greater than for a ballistic missile entering Earth's atmosphere, in a cloudy location, if the particle concentrations encountered are of the same order of magnitude. A large amount of damage can result from high initial entry velocities and an atmosphere of lower density than Earth's. Because of these two factors, the vehicle entering from space might be traveling at higher velocities at the altitudes where particles might be encountered than velocities realized with ballistic missiles in Earth's atmosphere. The lower atmospheric density would reduce aerodynamic heating, and, as a result, the protective melt layer might not be as deep as during a comparable Earth entry.

Acknowledgments

The test firings conducted during this study were carried out at ABMA under the direction of J. Cain, and the ABMA technical supervisor for the entire program was D. L. Burrows. The author also wishes to acknowledge the assistance of the several people at Battelle Memorial Institute who contributed to various phases of the program.

Nomenclature

c_g	=	specific heat of the gases evolved from decomposition of the plastic
d_p	=	particle diameter
E_R	=	ablation energy parameter defined by Equation [22]
F	=	fraction of particle impact kinetic energy transmitted to the plastic filler
F_p	=	force on particle
f	=	mass fraction of plastic filler in the undamaged material
g_c	=	consistent conversion factor
H	=	energy necessary to start the decomposition of the plastic filler
H_e	=	effective heat of ablation
J	=	conversion factor to energy units
m_p	=	particle mass
$\dot{m}$	=	total ablation rate
$\dot{m}_l$	=	rate at which material crosses the liquid-solid interface
$\dot{m}_p$	=	portion of ablation rate due to particle impact
$\dot{m}_{stored}$	=	rate at which the mass contained in the melt layer changes
$\dot{m}_{th}$	=	portion of ablation rate due to heat transfer
r_0	=	distance measured radially from axis of body
T	=	temperature
t	=	time
U_∞	=	free stream velocity
u	=	velocity in x direction
V	=	particle velocity
w_p	=	mass flow rate of particles
η	=	impaction efficiency
θ	=	angle measured from stagnation point
Λ	=	constant defined by Equation [12]
π	=	3.14 . . .
ρ	=	density

Subscripts

e	=	edge of gas boundary layer
f	=	solid-liquid interface
g	=	gas
i	=	gas-liquid interface
L	=	liquid
0	=	no particle impact condition
p	=	particle

References

1 Arthur, G. F., "Physical and Positional Properties of the Planets," WADC TN 58-347; ASTIA Doc. no. AD 206671, Dec. 1, 1958.

2 Ungar, E. W., "Investigation of High-Speed Particle Erosion of Melting Aerodynamic Surfaces," Battelle Memorial Institute, Columbus, Ohio, report to ABMA, Contract DA-33-019-ORD-2774, Sept. 15, 1959.

3 Lees, L., "Similarity Parameters for Surface Melting of a Blunt-Nosed Body in a High Velocity Gas Stream," ARS JOURNAL, vol. 29, no. 5, May 1959, p. 345.

4 Sutton, G. W., "The Hydrodynamics and Heat Conduction of a Melting Surface," *J. Aeron. Sci.*, vol. 25, no. 1, Jan. 1958, p. 29.

Ablation of Glassy Material Around Blunt Bodies of Revolution[1]

HENRY HIDALGO[2]

Avco-Everett Research Laboratory
Everett, Mass.

The steady-state equations of motion for a thin layer of an incompressible glassy material on the surface of an ablating and radiating blunt body are reduced to a first-order ordinary differential equation which is integrated numerically. This solution is coupled with the solution of the air boundary layer for both laminar and turbulent heat transfer with or without mass vaporization of the ablating material. The distribution of the effective energy of ablation around the body is thus obtained for a cone cylinder with a hemispherical cap that re-enters the atmosphere at hypersonic flight speeds, and has quartz as the ablating material. It is found that the ablation process from turbulent heating is more efficient than from the laminar case because of increased vaporization. This solution of the equations of motion at the stagnation point has been verified by arc wind tunnel experiments. The present state of development of the arc wind tunnel does not permit its use for experimental investigations of ablation around blunt bodies under turbulent heating.

THE KNOWLEDGE of the ablation process around the surface of a blunt body is important for the optimum design of satellites, ICBM's and any other bodies that must re-enter the atmosphere at hypersonic velocities. In this ablation process, the aerodynamic heat energy produced by friction is absorbed by the mechanisms of melting and vaporization of the surface material, mass injection into the air boundary layer from the vaporization of the material, and the radiation from the high temperature of ablation materials that have good emissivities. An additional mechanism of heat absorption is present when the ablating materials react chemically with the air boundary layer.

The aerodynamic heat transfer to the surface of blunt bodies that fly at hypersonic velocities inside the atmosphere has been solved in (2 to 5),[3] which consider the case of laminar and turbulent heating without mass injection into the air boundary layer. The effect of mass injection on the laminar heating rates can be obtained from the solution of the corresponding differential equations (6,7). For the turbulent case, the theory is not so well developed as for the laminar case. However, the available theoretical and experimental results (8,9) indicate that the mass injection effect on turbulent heat transfer is less important than the corresponding laminar case for injection materials that have a molecular weight equal to or heavier than air. For materials that are lighter than air, the mass injection effect seems to be about the same for both laminar and turbulent boundary layers.

The melting of the body surface creates a liquid layer underneath the air boundary layer. The high aerodynamic friction forces on the surface of such bodies—combined with minimum weight and high nose cone performance requirements—call for an ablating material that has a very high viscosity and low thermal conductivity.[4] High viscous forces will prevent the molten layer from leaving the surface before its energy of vaporization has been utilized for the reduction of heat energy into the body. The low conductivity will of course retard the heat flow into the body, and thus yield a more efficient ablation process. The equations of motion for a thin liquid layer on the surface of a body are in general those of the incompressible laminar boundary layer, with the appropriate boundary conditions. The requirement of a high viscosity leads to further important mathematical simplifications of the Navier-Stokes equation for a thin layer (10,11) which then yield approximate solutions that are extremely important for practical applications.

Equations for a Highly Viscous Liquid Layer

The equations of motion for a thin nonradiating liquid layer on the surface of the body are (12):

Continuity

$$\frac{\partial}{\partial x}(ur) + \frac{\partial}{\partial y}(vr) = 0 \qquad [1]$$

Momentum

$$\rho u \frac{\partial u}{\partial x} + \rho v \frac{\partial u}{\partial y} = -\frac{dp}{dx} + \frac{\partial}{\partial y}\left(\mu \frac{\partial u}{\partial y}\right) \qquad [2]$$

Energy

$$\rho c_p \left(u \frac{\partial T}{\partial x} + v \frac{\partial T}{\partial y}\right) = \frac{\partial}{\partial y}\left(k \frac{\partial T}{\partial y}\right) + u \frac{dp}{dx} + \mu \left(\frac{\partial u}{\partial y}\right)^2 \qquad [3]$$

Viscosity law

$$\mu = \mu(T) \qquad [4]$$

In these equations, the coordinate system is the same as in the gas boundary layer. Because $y = 0$ at the wall or gas-liquid interface and is positive in the gas layer, y is negative in the liquid layer. These equations can be solved by the usual numerical procedure of laminar boundary layer theory [as was done by Sutton who considered the liquid layer of Pyrex (13)]. However, this numerical procedure is too cumbersome and time-consuming for practical applications, and any approximate method of integration and appropriate simplification of these equations have great practical im-

Received Oct. 5, 1959.
[1] This work was sponsored by the Ballistic Missile Division, Air Research and Development Command, U. S. Air Force, under Contract AF 04(647)-278.
[2] Senior Engineer.
[3] Numbers in parentheses indicate References at end of paper.
[4] The energy equation (see Eq. [44]) indicates that for a given surface temperature, high values of h_{eff} require high values of the fraction of vaporized material f. This fraction is a strong function of viscosity. A material like Pyrex—which has material properties like quartz except for a lower viscosity—yields negligible values for f as compared with those for quartz even for the case of turbulent flow conditions.

portance. Von Kármán devised such an approximate method of solution by integrating the equations of motion in the y direction (12). Also, for a fluid with a very large viscosity, the inertia forces become considerably smaller as compared with the viscous forces, because the former vary with the velocity squared while the latter are linear with the flow velocity. The magnitude of the Reynolds number becomes of order unity, and the particle inertia forces may be dropped from the momentum equation (12,13). This condition is approximated by liquid glassy materials that do not have a well-defined melting temperature (10). An experimental verification of this approximate method of solution has been obtained at the stagnation point of ablating models in the arc wind tunnel (1), where it was found that the maximum discrepancy between theory and experiment is within 8 per cent.

Thus, the equations of motion for a liquid, highly viscous radiating material that are to be integrated in the y direction are:

Continuity

$$\frac{\partial}{\partial x}(ur) + \frac{\partial}{\partial y}(vr) = 0 \qquad [5]$$

Momentum

$$\frac{\partial}{\partial y}\left(\mu \frac{\partial u}{\partial y}\right) = \frac{dp}{dx} + \rho G \sin\theta \equiv P_x \qquad [6]$$

Energy

$$\rho c_p \left(u \frac{\partial T}{\partial x} + v \frac{\partial T}{\partial y}\right) = \frac{\partial}{\partial y}\left(k \frac{\partial T}{\partial y} - I\right) + u \frac{dp}{dx} + \mu \left(\frac{\partial u}{\partial y}\right)^2 \qquad [7]$$

Viscosity Law

$$\mu \propto \exp\left(AT^{-1}\right) \qquad [8]$$

The term $\rho G \sin\theta$ in Equation [6] represents the component of the missile inertia force on the liquid particle, and G is the number of g's acting along the missile longitudinal axis. It should be noted also that the energy Equation [7] includes the radiation heat flux I. The viscosity for a glassy material (Eq. [8]) can be expressed as an exponential in AT^{-1} (A = constant), which indicates that $\mu \to \infty$ as the temperature drops in a direction from the gas-liquid interface toward the interior of the body.

The integration of the continuity equation [5] yields

$$v = v_{-\infty} - \frac{1}{r}\frac{\partial}{\partial x}\left(r \int_{-\infty}^{y} u\, dy\right) \qquad [9]$$

or, using the conditions at the interface where $v = v_w$ and $y = 0$

$$\frac{v_w}{v_{-\infty}} = 1 - \frac{1}{r v_{-\infty}} \frac{d}{dx}\left(r \int_{-\infty}^{0} u\, dy\right) \qquad [10]$$

Equation [10] is the expression for the fraction of ablated material $v_w/v_{-\infty}$ that is vaporized into the gas boundary layer. It will be seen that this parameter together with the vaporization velocity v_w and the wall temperature T_w fix the effective enthalpy of ablation, which is defined as the energy that the ablated mass rate must absorb in order to balance the aerodynamic heat rate without mass injection effect $\dot{q}_0$, i.e., $\rho v_{-\infty} h_{eff} = \dot{q}_0$. The lower limit of integration is taken as $-\infty$ in the foregoing equations because the velocity u approaches 0 at the solid surface of the ablating body. This velocity u is obtained from the momentum equation [6], which yields

$$u(y) = \tau_{w_{gas}}(x) \int_{-\infty}^{y} \frac{dy}{\mu} + P_x(x) \int_{-\infty}^{y} \frac{y\, dy}{\mu} \qquad [11]$$

where $\tau_{w_{gas}}(x)$ is the gas shear at the gas-liquid interface, and can be evaluated approximately from the corresponding heat rate through the Reynolds analogy. The lower limit of integration is taken as $-\infty$ because the viscosity μ approaches ∞ in the interior of the body. In a limited temperature range, the exponential form of the viscosity law can also be represented empirically as $\mu \propto T^{-n}$, where n is a constant that depends on the temperature range, i.e., $n \propto T_w^{-1}$ (10,14). Therefore, the following expression may be obtained

$$\mu = \mu_w (T/T_w)^{-n} \qquad [12]$$

where n is large compared with unity. For example, for Pyrex, n is approximately 6 at $T = 4000$ F, and for quartz n is approximately 20. Since in the energy equation [7] the predominant terms involve the temperature gradient in the y direction, it is reasonable to assume that at any point around the surface of the ablating body the viscosity variation through the liquid layer will be as at the stagnation point, where $\mu \propto e^{-y/\delta}$ (10). However, the full energy equation [7] is now used to relate the ablation velocity $v_{-\infty}$ to the liquid layer thickness δ. Thus

$$\mu = \mu_w e^{-y/\delta} \qquad [13]$$

where $\delta = \delta(x)$. This expression indicates also an increase in viscosity in the liquid layer as $y \to -\infty$. Combining Equations [12 and 13]

$$T = T_w e^{y/n\delta} \qquad [14]$$

From which

$$\delta = \frac{1}{n}\frac{T}{\partial T/\partial y} = \frac{1}{n}\frac{T_w}{(\partial T/\partial y)_w} = \frac{1}{n}\frac{kT_w}{q_w} \qquad [15]$$

Thus, the liquid layer thickness δ becomes a boundary condition. It is important to note that the heat rate q_w is evaluated in the liquid side of the gas-liquid interface. From Equations [11 and 13]

$$u(y) = \frac{\tau_w \delta}{\mu_w} e^{y/\delta} + \frac{P_x \delta^2}{\mu_w} e^{y/\delta}\left(\frac{y}{\delta} - 1\right) \qquad [16]$$

which when introduced in Equation [10] yields

$$\frac{v_w}{v_{-\infty}} = 1 - \frac{1}{r v_{-\infty}} \frac{d}{dx}\left[r\left(\frac{\tau_w \delta^2}{\mu_w} - 2\frac{P_x \delta^3}{\mu_w}\right)\right] \qquad [17]$$

The wall temperature is related to the ablation velocity $v_{-\infty}$ through the energy equation [7]

$$\int_{-\infty}^{0} u \frac{\partial T}{\partial x} dy + \int_{-\infty}^{0} v \frac{\partial T}{\partial y} dy = \frac{1}{\rho c_p}(q_i - \epsilon\sigma T_w^4) + \frac{1}{\rho c_p}\int_{-\infty}^{0} (up_x + \mu u_y^2)\, dy \qquad [7a]$$

or

$$q_i - \epsilon\sigma T_w^4 = (1 + \xi)\rho c_p v_{-\infty} T_w \qquad [18]$$

where

$$q_i = \psi q_0 - \rho_L v_w h_v \qquad [19]$$

$$\xi = \xi_1 - \xi_2 \qquad [20]$$

$$\xi_1 = \frac{1}{v_{-\infty} T_w} \times \left[\int_{-\infty}^{0} u \frac{\partial T}{\partial x} dy - \frac{1}{r}\int_{-\infty}^{0} \frac{\partial T}{\partial y}\left(\frac{\partial}{\partial x} r \int_{-\infty}^{y} u\, dy\right) dy\right] \qquad [21]$$

$$\xi_2 = \frac{1}{\rho c_p v_{-\infty} T_w}\int_{-\infty}^{0} (up_x + \mu u_y^2)\, dy \qquad [22]$$

The integration of Equation [7a] includes the heat conduction process in the interior of the body because there u approaches 0, $v = v_{-\infty}$ and all the terms except the second term in the left-

hand side and the first term in the right-hand side of the equation become, then, negligibly small. The conditions of negligible temperature and thermal heat flux have been used as boundary conditions at the interior of the body. The heat rate q_i as defined by Equation [19] is the aerodynamic heat rate with mass injection effect (ψq_0) reduced by the energy required to vaporize the ablating material that is injected into the gas boundary layer ($\rho_L v_w h_v$). The function ψ is unity for zero mass injection effect; otherwise it is reduced from unity by a term that depends on the nature of the heating rates (laminar or turbulent). Equation [18] is the steady-state heat balance equation. Since the vaporization velocity v_w in Equation [17] is determined from the diffusion process in the gas boundary layer (Eqs. [31,32]), Equations [17 and 18] are the solution to the steady-state ablation problem, for they yield the ablation velocity $v_{-\infty}$ and wall temperature T_w. Thus from Equation [18]

$$v_{-\infty} = [q_i - \epsilon\sigma T_w{}^4 - \rho c_p T_w(\xi v_{-\infty})]/\rho c_p T_w \qquad [18a]$$

where $\xi v_{-\infty}$ is obtained from Equations [14, 16 and 20]

$$\xi_1 = \frac{u_{wL}\delta v_{-\infty}^{-1}}{1 - P_x\delta/\tau_w}\left[\frac{T_{wx}}{T_w}\left(1 - \frac{2P_x\delta}{\tau_w}\right) + \frac{2\delta_x}{n\delta}\left(\frac{9}{2}\frac{P_x\delta}{\tau_w} - 1\right) - \frac{1}{n}\left(\frac{\tau_{wx}}{\tau_w} + \frac{r_x}{r}\right) + \frac{3\delta}{n\tau_c}\left(P_{xx} + P_x\frac{r_x}{r}\right) + \frac{\mu_{wx}}{n\mu_w}\left(1 - \frac{3P_x\delta}{\tau_w}\right)\right] \qquad [21a]$$

where conditions $n^{-1} \ll 1$ have been used. The expression for ξ_2 is

$$\xi_2 = \frac{u_{wL}v_{-\infty}^{-1}}{1 - P_x\delta/\tau_w}\frac{\tau_w}{\rho c_p T_w}\left[\left(1 + \frac{p_x\delta}{\tau_w}\right)\left(1 - \frac{2P_x\delta}{\tau_w}\right) + 2\left(\frac{P_x\delta}{\tau_w}\right)^2\right] \qquad [22a]$$

which, with the aid of Reynolds analogy

$$\tau_w = \psi q_0 u_e \sigma_{Pas}{}^{2/3}/(H_e - H_w) \qquad [23]$$

and Equation [18] becomes

$$\xi_2 = \frac{1 + \xi}{1 - P_x\delta/\tau_w}\frac{u_e{}^2/H_e}{1 - H_w/H_e}\frac{\sigma_{Pas}{}^{2/3}}{1 - [(\rho_L v_w h_v - \epsilon\sigma T_w{}^4)/\psi q_0]}\frac{u_{wL}}{u_e}\left[\left(1 + \frac{p_x\delta}{\tau_w}\right)\left(1 - \frac{2P_x\delta}{\tau_w}\right) + 2\left(\frac{P_x\delta}{\tau_w}\right)^2\right] \qquad [22b]$$

The condition of a positive tangential velocity at the gas liquid interface requires $P_x\delta/\tau_w < 1$. It is thus seen that ξ_2 has the order of magnitude of u_{WL}/u_e which is negligible compared with unity and may be neglected in Equation [18]. Except at sharp corners in the body contour where there are large Prandtl-Meyer expansions, ξ_1 is much less than 1. This term is usually small because it is produced mainly by the energy transfer in the liquid layer in a direction parallel to the surface of the body, and this is small compared with the energy transfer normal to the surface of the body.

Equation [17] is a first-order differential equation that requires one set of boundary conditions, and can be solved more conveniently by using a stepwise numerical procedure that starts at the stagnation point of the body, where by symmetry $\delta_x = T_{wx} = 0$. This general equation [17] can be specialized to the stagnation point of a blunt body and to a semi-infinite cylinder as follows.

Stagnation Point

At the stagnation point region the conditions $r = x$, $\tau_w = \tau_{wx}x$, $p_x = p_{xx}x$, $\delta_x = T_{wx} = \mu_{wx} = 0$ can be used in Equations [17 and 21]. The result is

$$\left(\frac{v_w}{v_{-\infty}}\right)_s = 1 - \frac{2\delta^2}{\mu_w v_{-\infty}}(\tau_{wx} - 2\delta P_{xx}) \qquad [24]$$

$$\xi_s = \frac{2\tau_{wx}\delta^2}{\mu_w v_{-\infty} n}\left(\frac{3P_{xx}\delta}{\tau_{wx}} - 1\right) \qquad [25]$$

Cylindrical Body

At the cylindrical section of an ablating body that is long enough to be unaffected by the ablation history ahead of it, Equation [17] yields

$$\left(\frac{v_w}{v_{-\infty}}\right)_{CYL} = 1 - \frac{1}{v_{-\infty}}\frac{d}{dx}\left(\frac{\tau_w\delta^2}{\mu_w} - 2\frac{P_x\delta^3}{\mu_w}\right) \qquad [26]$$

$$\xi_{CYL} = \frac{\tau_w\delta\delta_x}{n\mu_w v_{-\infty}}\left(9\frac{P_x\delta}{\tau_w} - \frac{\tau_{wx}\delta}{\tau_w\delta_x} - 2\right) \qquad [27]$$

Effect of Radiation Mean Free Path on Ablation

The general treatment of radiation effects on ablation is given in (15 and 16). It is shown there that the radiation mean free path has a strong effect on ablation, as can be seen from Equations [15 and 18], which yield

$$\delta = \frac{k}{\rho c_p v_{-\infty} n(1 + \xi)}\frac{q_i - \epsilon\sigma T_w{}^4}{q_w} \qquad [28]$$

When the radiation mean free path λ is small compared with the liquid layer thickness δ, i.e., $\lambda/\delta \ll 1$, the liquid layer absorbs the radiation flux. In this case, a heat balance across a liquid sublayer having a thickness λ at the gas-liquid interface yields $q_w - 0 = q_i - \epsilon\sigma T_w{}^4$. This is so because in the liquid side of this sublayer there are two equal radiation heat fluxes but in opposite directions. In the gas side of the sublayer, because the gas is transparent to radiation, there is only one radiation flux towards the gas boundary layer. Thus, Equation [28] becomes

$$\delta_{\lambda/\delta<<1} = k/\rho c_p n v_{-\infty}(1 + \xi) \qquad [29]$$

It must be pointed out that in this case Equation [14] does not hold in this sublayer at the gas-liquid interface, and must be modified as indicated in (16). This is a local effect, however, for Equation [14] is a good approximation for the temperature distribution in the liquid layer and interior of the body even for this case. On the other hand, when $\lambda/\delta \gg 1$, the liquid layer is transparent to radiation. The conditions at the gas and liquid side of this sublayer are the same. Hence, the heat balance yields $q_w - \epsilon\sigma T_w{}^4 = q_i - \epsilon\sigma T_w{}^4$ or $q_w = q_i$. The liquid layer thickness becomes then from Equation [28]

$$\delta_{\lambda/\delta>>1} = \frac{k}{\rho c_p n v_{-\infty}(1 + \xi)}\left(1 - \frac{\epsilon\sigma T_w{}^4}{q_i}\right) \qquad [30]$$

Thus, the radiation mean free path affects the liquid layer thickness, and therefore, the fraction of vaporized material.

Diffusion Equation and Vapor Pressure Law

From the diffusion equation in the gas boundary layer in the absence of chemical reactions and neglecting pressure

gradient effects, is obtained (7)

$$v_w = \frac{C_{2w}}{1 - C_{2w}} \frac{\psi q_0}{H_e - H_w} \left(\frac{D\mathcal{L}_p}{k}\right) \quad [31]$$

$$C_{2w} = \left[1 + \frac{M_{air}}{M_v}\left(\frac{p}{p_v} - 1\right)\right]^{-1} \quad [32]$$

where the vapor pressure p_v of the vaporized material must, of course, be known as a function of the wall temperature and the aerodynamic pressure. (For glassy materials where silica sand SiO_2 is the principal ingredient, see Appendix.) The parameter, $D\mathcal{L}_p/k$ in Equation [31] is obtained from the Lewis number, which for glassy materials can be assumed to be unity.

Mass Injection Effect on Heat Transfer

The injection of the vaporized ablated material into the air boundary layer reduces the heat transfer rate and the gas shear at the gas-liquid interface. These two parameters can be related approximately by using the Reynolds analogy. For a given injection material and injection rate, the reduction in the heat transfer rate depends in general on the type of flow in the boundary layer.

Laminar Flow

An investigation was made of the effect of air mass injection on the heat transfer from a partially dissociated air laminar boundary layer in thermodynamic equilibrium. As discussed in (3), the respective momentum and energy equations are

$$(lf_{\eta\eta})_\eta + ff_{\eta\eta} + \beta(\rho_e/\rho - f_\eta^2) = 0 \quad [33]$$

$$(lg_\eta\sigma^{-1})_\eta + fg_\eta + (u_e^2/H_e)[(1 - \sigma^{-1})lf_\eta f_{\eta\eta}]_\eta = 0 \quad [34]$$

The local pressure gradient and Mach number effects on heat transfer are given by β and u_e^2/H_e, respectively.

The mass injection effect is introduced as a boundary condition at the wall to the foregoing system of differential equations. From the results of (3)

$$-f_w = \xi_x^{-1}\sqrt{2\xi}\, r(\rho v)_w \quad [35]$$

where the conditions of local similarity $f_\xi = 0$ and negligible slip ($f_{\eta w} \approx 0$) have been used. This latter condition is possible because the velocity u at the gas-liquid interface is very small compared with the velocity at the edge of the boundary layer. Introducing the blowing parameter B which is defined as

$$B = \frac{\rho_w v_w}{\rho_e u_e St_0} = \frac{2F}{C_{f_0}\,\sigma^{-2/3}} = \frac{\rho_w v_w}{q_0}(H_e - H_w) \quad [36]$$

where (3)

$$\frac{q_0}{q_{0_r}} = \frac{r\rho_w\mu_w u_e}{\sqrt{2\xi}}\left[2\rho_{ws}\,\mu_{ws}\left(\frac{du_e}{dx}\right)_e\right]^{-1/2}\frac{g_{\eta w}}{g_{\eta w\,s}} \quad [37]$$

$$q_{0_r} = 0.76\,\sigma^{-0.6}\,(\rho_w\mu_w)_e^{0.1}\,(\rho_e\mu_e)_e^{0.4}\,H_e\,(1 - g_{ws})\times \left(\frac{d\mu_e}{dx}\right)_e^{1/2}\left[1 + (L^\alpha - 1)\frac{h_{DS}}{H_e}\right] \quad [38]$$

The combination of Equations [35 to 38] for a Lewis number of unity yield

$$B = 1.865\sigma^{0.6}l_{es}^{-0.4}(-f_w)[1.068/(1 + 0.096)\sqrt{\beta})] \quad [39]$$

where

$$l_{es} = (\rho_e\mu_e/\rho_w\mu_w)_s$$

The ratio of heat transfer rate with mass injection to the heat transfer rate without injection ψ as obtained from these numerical solutions can be correlated by the parameter shown in Fig. 1. It is seen that

$$\psi = 1 - 0.58l^{0.04}\,\sigma^{-0.18}B[(1 + 0.096\sqrt{\beta})/1.068] \quad [40]$$

This correlation holds for the injection of air into the dissociated air boundary layer. It shows a very weak dependence on l. The power of the Prandtl number is the result of two effects:

1 The quantity $1 - \psi$ varies as $\sigma^{0.42}$.

2 The heat rate q_0 varies as $\sigma^{-0.6}$.

The effect of pressure gradient and dissipation terms on this correlation was found to be small. There is also a somewhat weak effect of the molecular weight as is shown by the results of (7). A correlation of the results of (7) indicates that the blowing parameter B should be multiplied by $M_{Ai}^{1/4}$, where M_{Ai} is the ratio of the molecular weight of air to that of the injected material. Thus for laminar flow the mass injection correlation becomes

$$\psi = 1 - 0.58l^{0.04}\,\sigma^{-0.18}M_{Ai}^{1/4}B(1 + 0.096\sqrt{\beta})/1.068 \quad [40a]$$

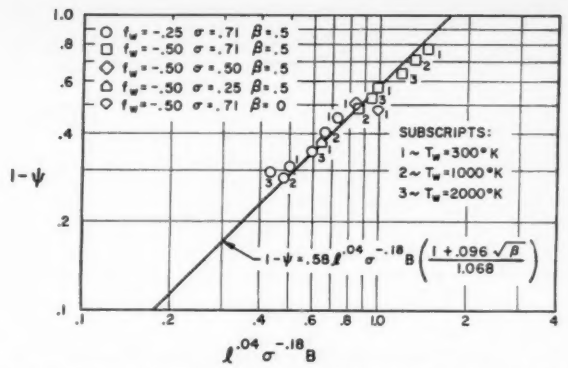

Fig. 1 Effect of air injection on heating rates from a partially dissociated laminar boundary layer

Turbulent Flow

The effect of mass injection on the turbulent heat transfer rates can be obtained from the experimental results of (8 and 9). Reference (8) shows data for local heat transfer rates for the case of air injection into a turbulent boundary layer on a flat plate with an external Mach number of 2.7. Reference (9) presents data for the total skin friction coefficient for the case of injection of helium, air and freon-12 (CCl_2F_2) into a turbulent boundary layer on a cone with subsonic and supersonic flow at the edge of the boundary layer. This data indicates a weak Mach number effect on skin friction for small injection rates. As the mass injection rates increase, the reduction in skin friction is larger at subsonic speeds. Using this latter data for the case of supersonic flow, the following approximate correlation is obtained for the total skin friction coefficient C_F

$$\frac{C_F}{C_{F_0}} = 1 - \frac{1}{5}M_{Ai}^{\alpha}\left(\frac{2F}{C_{F_0}}\right) \quad [41]$$

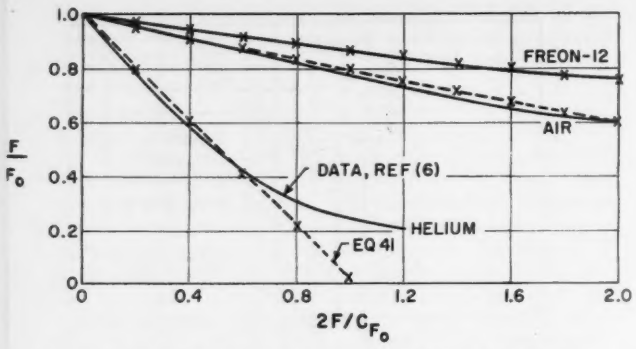

Fig. 2 Effect of mass injection on the turbulent skin friction coefficient for a cone, $M_e = 3.21$

where

$\alpha = \frac{1}{3}$ when $M_{Ai} \leq 1$

$\alpha = \frac{4}{5}$ when $M_{Ai} \geq 1$

This correlation is shown in Fig. 2. The relation between the local (C_f) and total (C_F) skin friction coefficients is given by

$$C_F = \left(\frac{1}{A}\right) \int \left(\frac{C_f}{C_{f_0}}\right) C_{f_0} dA$$

where A is the wetted area of the body. Since at a given body location, the ratio C_f/C_{f0} is independent of body position, C_F/C_{F_0} is equal to C_f/C_{f_0}. From the results of (5), $C_{f_0} \propto x^{-1/5}$. Hence, $C_{F_0} = C_{f_0}\bar{A}$, where

$$\bar{A} = A^{-1} x^{1/5} \int x^{1/5} dA$$

Theoretical and experimental data indicate that both the skin friction and heating rates for turbulent boundary layers decrease with mass injection. These two parameters can be related approximately by extending the Reynolds analogy to the case of mass injection, in particular for the case $M_{Ai} \leq 1$ where the magnitude of this effect is smaller (9). Hence, Equation [41] can be written as

$$\psi = \frac{(\partial T/\partial y)_w}{(\partial T/\partial y)_{w,0}} \approx \frac{C_f}{C_{f_0}} = 1 - \frac{1}{5} M_{Ai}^{\alpha} \frac{2F}{C_{f_0}\bar{A}} \qquad [41a]$$

or with Equation [36]

$$\psi = 1 - \frac{1}{5} M_{Ai}^{\alpha} \frac{B}{\bar{A}\sigma^{2/3}} \qquad [41b]$$

For $\sigma = 0.72$, the parameter $\bar{A}\sigma^{2/3}$ equals $\frac{8}{9}$ for a cone and unity for a cylinder. The turbulent data of (9) show a large reduction in heat transfer rates for light injection materials, i.e., materials that have a molecular weight lower than that of air. Equation [41] indicates this fact through the value of $\alpha = \frac{4}{5}$. For materials that are heavier than air, the reduction in heating rates is less important, as is indicated by a value of $\alpha = \frac{1}{3}$.

It is also noted that for air injection ($\sigma = 0.72$), the numerical coefficient in the laminar equation [40] becomes three times larger than the corresponding numerical coefficient in the turbulent equation [41b]. This indicates that for injection materials like air, the effect of mass injection on heat rates is less significant for turbulent than for laminar flow. Equations [40a and 41b] indicate, respectively, the effect of mass injection on the gas shear and heat rates for the conditions of laminar and turbulent boundary layers.

Determination of Ablation Parameters

For a given blunt body geometry and flight conditions, the pressure distribution around the body can be determined independently of the ablation equations. The aerodynamic heating rates and local shear forces without mass injection effects for both laminar and turbulent boundary layers then become proportional only to the wall temperature of the ablating body. The ablation calculation is started at the stagnation point where Equations [24 and 25] are used instead of Equations [17 and 20]. The use of Equation [17] around the surface of the ablating body requires a stepwise numerical procedure. By assuming a wall temperature, it is possible to calculate all the terms in Equation [24] at the stagnation point, and in Equation [17] around the body through the successive use of Equation [31] for v_w, Equation [18] for $v_{-\infty}$ and [29] or [30] for δ. The viscosity is obtained from the corresponding equation [8], and the gas shear at the interface from [23]. Note that at the stagnation point where the shear and velocity u_e are proportional to x, τ_{wx} is then proportional to the velocity gradient u_{ex}. For a Newtonian pressure distribution

$$u_{ex} = \sqrt{2}\, R^{-1}[(p_e - p_\infty)\rho_e^{-1}]^{1/2}$$

An iteration procedure on wall temperature is then utilized until either Equation [24] or [17] is satisfied.

Effective Energy of Ablation

The parameter that indicates the aerodynamic heat energy that is absorbed per unit mass of ablating material is defined by

$$h_{eff} = q_0/\rho v_{-\infty} \qquad [42]$$

where q_0 is the aerodynamic heat rate per unit area without mass injection effect to the ablating body. This parameter h_{eff} is a function of both location on the body contour and time along a flight trajectory. An integrated energy of ablation for the ablation process during re-entry can be defined as

$$\bar{h}_{eff} = \int_{t_i}^{t_f} q_0\, dt \Big/ \int_{t_i}^{t_f} \rho v_{-\infty} dt \qquad [43]$$

The numerator is the total local heat input during the time of ablation, and the denominator is the total local ablated mass. This parameter $\bar{h}_{eff}$ is only a function of position on the surface of the body. From the energy equation [18], h_{eff} can be written as

$$h_{eff} = \{(1 + \xi)c_p T_w + f[h_v + K(H_e - H_w)]\} \times (1 - q_r/q_0)^{-1} \qquad [44]$$

where K is the coefficient of the blowing parameter in [40a] or [41b]. Equation [44] can also be expressed as

$$h_{eff} = (1 + \xi)c_p T_w + \frac{v_w}{v_{-\infty}} h_v + (1 - \psi)h_{eff} + \frac{q_r}{q_0} h_{eff} \qquad [45]$$

Equation [44] shows the rather powerful effect of radiation on h_{eff} as $q_r/q_0 \to 1$, which is the limiting condition when all the aerodynamic heat is radiated away from the body. It should be pointed out, however, that this condition also gives a somewhat higher surface temperature, which yields higher q_r and lower q_0 rates. A higher surface temperature means a thicker insulating material for a given value of the temperature behind the heat shield material (17). Thus the effective energy of ablation as well as the surface temperature are the important parameters for the determination of the heat shield material along a given flight trajectory.

Equation [45] indicates the breakdown or contributions to the effective energy of ablation by the mechanisms of heat conduction, vaporization, mass injection and radiation, respectively. From this equation (or Eq. [18]) it is also seen that for steady-state ablation h_{eff} is always positive.

Applications

The foregoing analysis is now illustrated by using a body shape of the Thor-Able type and typical trajectories for hypersonic flight (18). The ablating material is chosen to be quartz. The properties of this material are as given in the Appendix. A Newtonian pressure distribution is assumed for the hemispherical cap and cone, and a Prandtl-Meyer expansion is assumed to take place at the junction between the cone and cylindrical section of the body. For the sake of simplicity, the pressure on the cylinder is assumed to be constant. The heat rates are calculated by assuming that the air is in thermodynamic equilibrium. It is, of course, necessary to know the conditions for transition from laminar to turbulent boundary layers. Based on the shock tube data of (19), transition is assumed to take place at $Re = 250$.

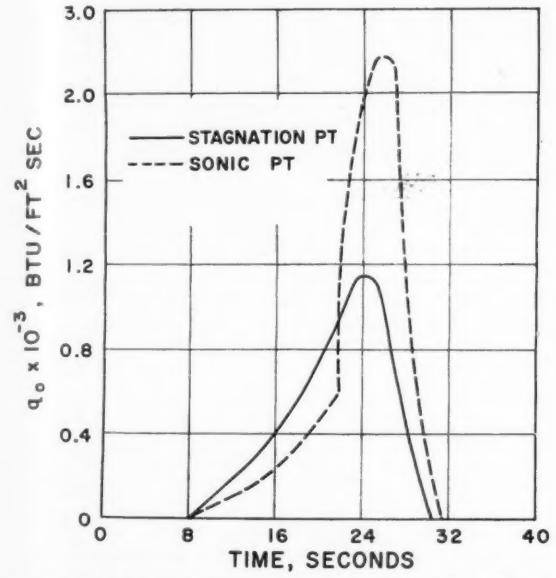

Fig. 3a Heating rates at stagnation and sonic points for typical 5000-nautical mile trajectory. $R_N = \frac{1}{2}$ ft, $R_{CYL}/R_N = 1.5$, $\alpha_c = 30$ deg

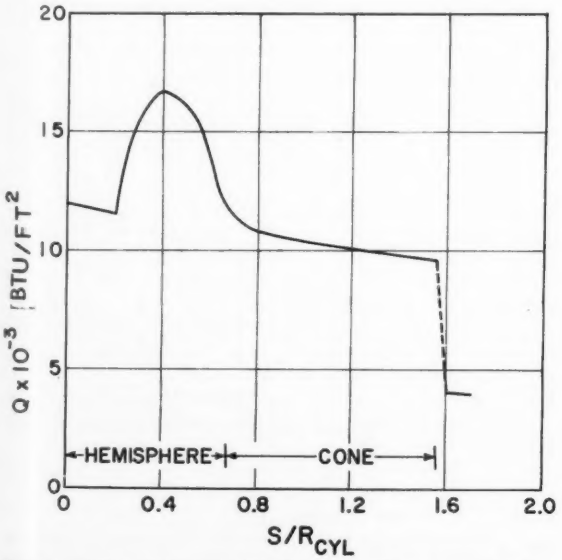

Fig. 3b Total aerodynamic heat input per unit area around body. Typical 5000-nautical mile trajectory. $R_N = \frac{1}{2}$ ft, $R_{CYL} = 1.5$, $\alpha_c = 30$ deg

Fig. 3a indicates the aerodynamic heating to the ablating surface, without mass injection effect, during re-entry at the stagnation point and sonic point on the spherical cap of a typical nose cone that has a range of 5000 nautical miles. The sonic point shows the effect of transition from laminar to turbulent flow after about 14 sec of flight time in the atmosphere. It is also seen that the peak turbulent heating rate at the sonic point is about two times larger than the corresponding laminar rate at the stagnation point. The total heat input per unit area $\int q_0 dt$ distribution around the body during the ablation process is as shown in Fig. 3b.

The ablation velocity time history at the stagnation and sonic points of the above nose cone is indicated in Fig. 4a. This is the velocity with which the surface of the body moves toward the interior of the body. It is noted that the peak values of the ablation velocity at these two points differ by about only 15 per cent, even though the corresponding laminar and turbulent heating rates differ by a factor of 2.0. The reason for this is that there is more vaporization in the ablation process with turbulent heating than in the laminar case. The ablated thickness $\int v_{-\infty} dt$ along the body contour for the typical 5000-nautical miles nose cone is shown in Fig. 4b. The effect of emissivity on ablated thickness is also illustrated for the transparent case, i.e., $\lambda/\delta \gg 1$. It is seen that the maximum ablated thickness takes place near the sonic point on the spherical nose, where the turbulent heating rates reach a maximum along the body contour. The maximum change in body radius takes place when there is no radiation, and is about 7 per cent of the original radius. The loss of ablated material from the surface of the cone is less than at the stagnation point because of the increased vaporization, since heating rates are comparable (Fig. 3b). The ablation thickness on the cylinder is much smaller than at the cone, and is caused by the sharp drop in the heating rates at the cone-cylinder junction which is produced by the Prandtl-Meyer expansion in that region. In actual flight, as the pressure and, consequently, the heating rates, decay along the surface of the cylinder, the ablation process will eventually stop. Under these conditions, the assumption of steady-state ablation breaks down. The unsteady effects in the continuity and momentum equations for the liquid layer are negligible because the density is constant and the inertia forces remain small compared with the viscous forces. However, the energy equation must be modified by retaining the term $\partial T/\partial t$ in the left-hand side of Equation [7]. Also, these equations of motion will not yield solutions for the combination of large inertia (G's) and low aerodynamic shear forces.

The integrated effective energy of ablation ($\bar{h}_{eff}$) distribution around the body is as shown in Fig. 5. It indicates that for a given emissivity, the value of $\bar{h}_{eff}$ is considerably higher for turbulent flow conditions on the cone than for the laminar values at and near the stagnation point. As the emissivity increases, $\bar{h}_{eff}$ also increases because of the increase of energy that is radiated away from the surface, which produces mainly a decrease in the ablation velocity. The effect of both emissivity and radiation mean free path on the energy of ablation is as illustrated in Fig. 6. It shows that for a given emissivity, h_{eff} is higher for the case when the liquid layer is transparent to radiation. Fig. 7 shows that increased radiation tends to cool the ablating surface and that the radiation mean free path has a negligible effect on surface temperature. It should be mentioned that the viscosity data for quartz at high temperatures are not well known. However, since the viscosity is an exponential function in the inverse value of the temperature, a plot of ln μ vs. T^{-1} is a straight line. This facilitates the extrapolation of viscosity data to higher temperatures. It was also found that if the viscosity at the highest temperature of interest (i.e., 6500 R) is varied arbitrarily by a factor of ± 3.0 from the extrapo-

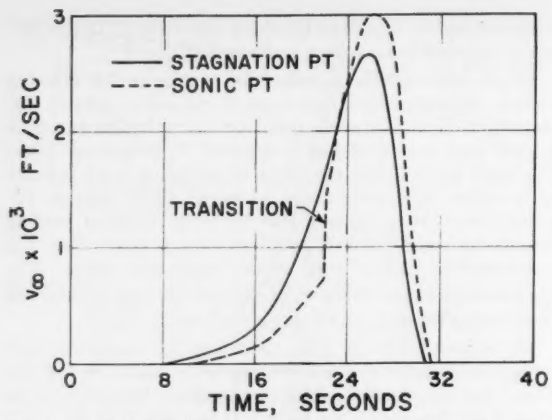

Fig. 4a Ablation velocities for quartz at stagnation and sonic points for typical 5000-nautical mile trajectory. $R_N = \frac{1}{2}$ ft, $R_{CYL}/R_N = 1.5$, $\alpha_c = 30$ deg, $\epsilon = \frac{1}{4}$

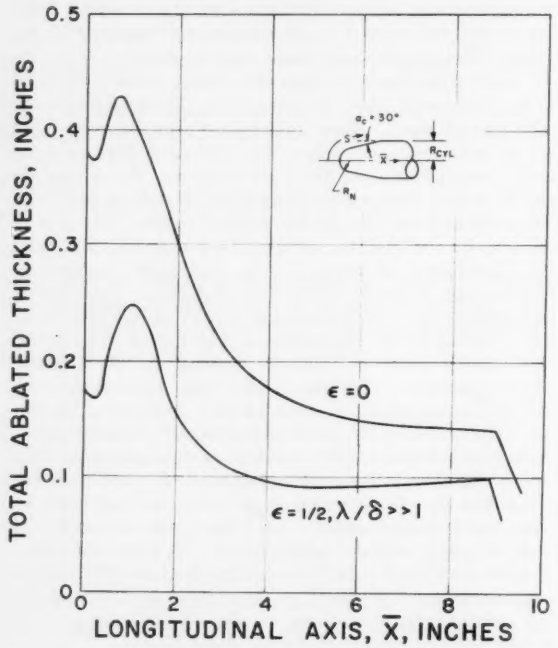

Fig. 4b Ablated thickness around body for quartz. Typical 5000-nautical mile trajectory. $R_N = \frac{1}{2}$ ft, $R_{CYL}/R_N = 1.5$, $\alpha_c = 30$ deg

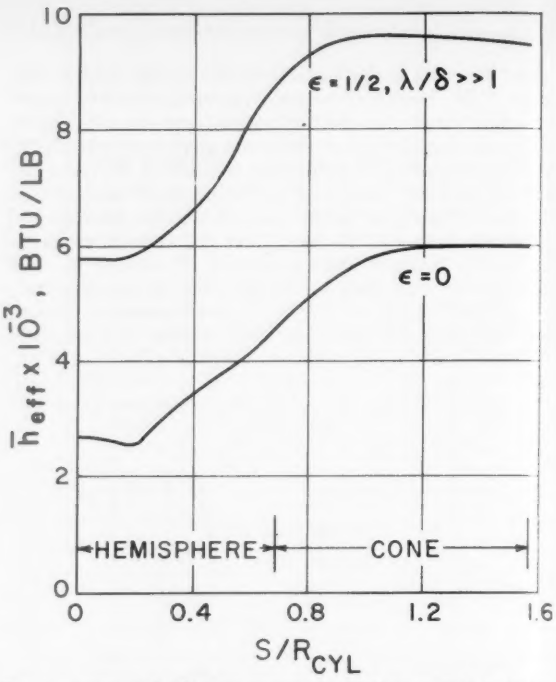

Fig. 5 Integrated effective energy of ablation around body for quartz. Typical 5000-nautical mile trajectory. $R_N = \frac{1}{2}$ ft, $R_{CYL}/R_N = 1.5$, $\alpha_c = 30$ deg

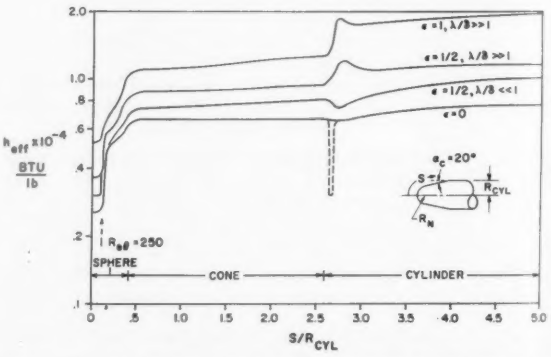

Fig. 6 Effect of radiation on the effective energy of ablation for quartz. $V_F = 20{,}000$ fps, 60,000-ft altitude. $R_N = \frac{1}{2}$ ft, $R_{CYL}/R_N = 3.0$, $\alpha_c = 20$ deg

lated value (see Appendix), the total ablated thickness varies then by a corresponding ±20 per cent. Fig. 8 indicates the contribution of the several mechanisms of heat absorption to the effective energy of ablation for the case where the emissivity is 0.5. It is noted that as the gas boundary layer becomes turbulent near the stagnation point, the fraction of vaporized material increases appreciably from the laminar value. This fraction of vaporized material is a function of both viscosity and type of heating (i.e., laminar or turbulent). For a material such as Pyrex, which has ablation properties similar to those of quartz except for an appreciably lower viscosity, the fraction of vaporized material is very small even for the case of turbulent heating. For a material of high viscosity, e.g., quartz, the fraction of vaporized material depends on whether the boundary layer is laminar or turbulent. This is illustrated in Figs. 9, which compare the effective energy of ablation distribution for both laminar and turbulent flow for the case of zero radiation.

Figs. 9a and 9b show that the vaporization for turbulent flow is 50 per cent higher than for laminar flow. Fig. 9c compares the effective energy of ablation. Figs. 8 and 9 indicate that the effect of mass injection on h_{eff} is small for the ablation of quartz, and that it is about the same for both laminar and turbulent flow. In this latter case, the increased vaporization compensates for the weaker effect of mass injection on turbulent heating rates, when they are compared with the laminar case at the same value of the blowing parameter.

For the flight conditions indicated in Fig. 6, the tangential velocity at the gas liquid interface reaches a maximum value of about 10 fps near the sonic point. The Reynolds number $u_w\delta/\nu_w$ also reaches a maximum value of 3.0 at this station (for gases, $u\delta/\nu$ is of the order of 10^3), and the liquid layer thickness δ reaches a maximum value of 5×10^{-4} ft on the cylindrical section of the body.

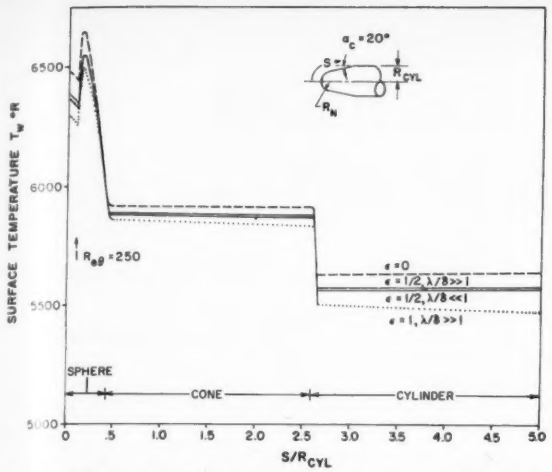

Fig. 7 **Effects of radiation on surface temperature for quartz. V_F = 20,000 fps, 60,000-ft altitude. R_N = ½ ft, R_{CYL}/R_N = 3.0, α_c = 20 deg**

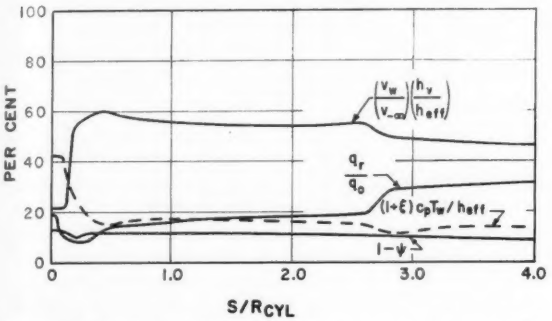

Fig. 8 **Mechanisms of heat absorption. ϵ = ½, V_F = 20,000 fps, 60,000-ft altitude. R_N = ½ ft, R_{CYL}/R_N = 3.0, α_c = 20 deg**

Conclusions

The Bethe-Adams theory of ablation (10) at the stagnation point of a blunt body of revolution has been extended to include the effect of turbulent heat transfer and radiation effects. The results for an ICBM nose cone indicate the important result that the fraction of vaporized material for a highly viscous liquid layer increases appreciably for turbulent boundary layers—a very fortunate result for practical applications. Also, the turbulent mass injection effect on the magnitude of the energy of ablation is at most of the order of 20 per cent, which is again a fortunate result because of the lack of complete theoretical understanding and limited amount of experimental data available on this mass injection process.

Appendix

Physical Properties of Quartz (1)

Specific heat c_p, Btu/lb R	0.25
Thermal conductivity k, (Btu/ft sec R)	3.2×10^{-4}, $T > 1800$ R
Density, lb/ft³	140
Viscosity μ, lb/ft sec	$0.0672 \exp[124{,}000/T\,(\text{deg R}) - 20]$
Heat of vaporization h_v, Btu/lb	5500

Vapor pressure law

$$\left(\frac{p_v}{p_v^*}\right)\left[0.4 + 0.6\left(\frac{p}{p_v}\right)\right]^{1/3} = 1$$

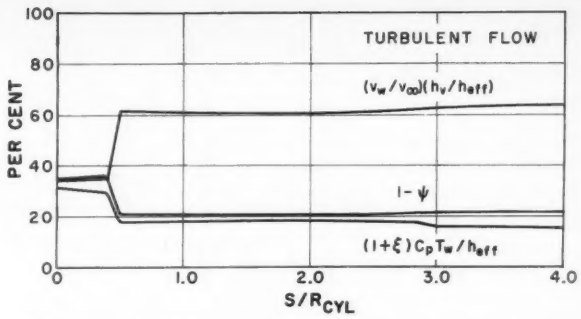

Fig. 9a **Mechanisms of heat absorption for laminar flow. ϵ = 0, V_F = 23,000 fps, 100,000-ft altitude. R_N = ½ ft, R_{CYL}/R_N = 3.0, α_c = 20 deg**

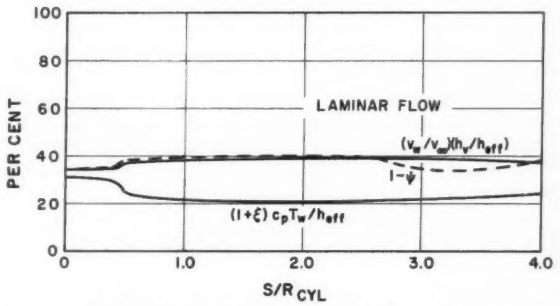

Fig. 9b **Mechanisms of heat absorption for turbulent flow. ϵ = 0, V_F = 23,000 fps, 100,000-ft altitude. R_N = ½ ft, R_{CYL}/R_N = 3.0, α_c = 20 deg**

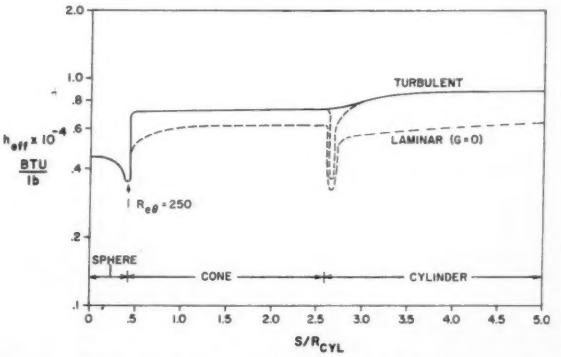

Fig. 9c **Effect of laminar and turbulent heating rates on the effective energy of ablation. ϵ = 0, V_F = 23,000 fps, 100,000-ft altitude. R_N = ½ ft, R_{CYL}/R_N = 3.0, α_c = 20 deg**

where

$$p_v^* = \exp[-104{,}000/T(\text{deg R}) + 18.48]$$

The effect of aerodynamic pressure on the vapor pressure law, as given by this equation is obtained as described in the following.

Vapor Pressure Reactions for Silica

$$S_iO_{2\text{condensed}} \rightleftarrows S_iO_{2\text{gas}} \qquad [A\text{-}1]$$

$$S_iO_{2\text{gas}} \rightleftarrows S_iO + \tfrac{1}{2}O_2 \qquad [A\text{-}2]$$

The pressure through the gas boundary layer is

$$p_{air} + p_v = p \qquad [A\text{-}3]$$

where

$$p_v = p_{Si_2O} + p_{O_2}' \quad [A\text{-}4]$$

$$P_{O_2} = 0.2\, p_{air} + p_{O_2}' \quad [A\text{-}5]$$

where p_{O_2}' represents O_2 particles created by reaction [A-2]. The conservation of species yields—

$$\frac{p_{Si_2O_2} + p_{Si_2O}}{p_{Si_2O} + 2p_{O_2}'} = \frac{1}{2} \quad [A\text{-}6]$$

or, since $p_{Si_2O}/p_{Si_2O_2} \ll 1$

$$2p_{O_2}' = p_{Si_2O} \quad [A\text{-}7]$$

which with Equation [A-4] yields

$$p_v = 3p_{O_2}' = \tfrac{3}{2}\, p_{Si_2O} \quad [A\text{-}8]$$

From the reactions [A-1 and A-2]

$$p_{Si_2O_2} = K_1\, e^{-L/kT} \quad [A\text{-}9]$$

$$p_{Si_2O}\, p_{O_2}{}^{1/2}/p_{Si_2O_2} = K_2\, e^{[1/2DE(O_2) - DE(Si_2O_2)]/kT} \quad [A\text{-}10]$$

Note that p_{O_2} and not p_{O_2}' is used in [A-10]. This means that the presence of O_2 from air affects the equilibrium concentration of O_2 and hence production of Si_2O (Eq. [A-6]).

Introducing Equations [A-8, A-3, A-4 and A-5] into [A-9 and A-10]

$$\tfrac{3}{2}\, p_v[0.2p + 0.133p_v]^{1/2} = \alpha \quad [A\text{-}11]$$

where

$$\alpha = K_1K_2 \exp \frac{(1/2)DE(O_2) - L - DE(Si_2O_2)}{kT}$$

For the case when there is no air, $p_v = p_v{}^*$ and $p_{O_2} = p_{O_2}'$. Hence [A-11] yields

$$\alpha = (2/3\sqrt{3})(p_v{}^*)^{3/2}$$

which when combined with [A-11] yields

$$\left(\frac{p_v}{p_v{}^*}\right)\left[0.4 + 0.6\left(\frac{p}{p_v}\right)\right]^{1/3} = 1 \quad [A\text{-}12]$$

Acknowledgments

The author would like to thank Dr. Mac C. Adams, Deputy Director of the Avco-Everett Research Laboratory for many valuable discussions, and Leo P. Kadanoff for discussions of the effect of radiation mean free path on ablation.

Nomenclature

c_p = heat capacity per unit mass
C_{2w} = concentration of ablated material in boundary layer
f_η = u/u_e
g = H/H_e
h = enthalpy (energy per unit mass)
h_{eff} = effective energy absorbed per unit mass of ablated material
H = stagnation enthalpy
k = thermal conductivity
l = $\rho\mu/\rho_w\mu_w$
M = molecular weight ratio (air to vapor)
n = viscosity parameter
p = pressure
q = heat transfer rate per unit area
q_r = $\epsilon\sigma T_w{}^4$
q_0 = heat transfer rate to hot nonablating surface
r = body dimension measured normal to axis
R = body nose radius
t = time, sec
T = temperature
U = stream velocity
u = velocity tangent to body surface
v = velocity normal to body surface
v_w = vaporization velocity
v_{-w} = ablation velocity
x = coordinate tangent to body surface
y = coordinate normal to body surface
δ = thickness of liquid layer
μ = viscosity
ρ = density
σ = Prandtl number ($c_p\mu/k$), Stefan-Boltzmann constant
τ = shear stress
τ_0 = shear stress on nonablating surface
ψ = ratio of heat transfer with and without mass injection
λ = radiation mean free path
ϵ = emissivity
θ = angle generated by rotation of nose radius away from stagnation point

Subscripts

i, w = gas-liquid interface
L = liquid property
s = gas property at stagnation point
v = property of glass vapor
e = external edge of boundary layer
x = differentiation with respect to x
y = differentiation with respect to y
CYL = cylinder

References

1 Adams, M. C., Powers, W. E. and Georgiev, S., "An Experimental and Theoretical Study of Quartz Ablation at the Stagnation Point," Avco-Everett Research Laboratory, Research Rep. 57, June 1959.

2 Fay, J. A. and Riddell, F. R., "Theory of Stagnation Point Heat Transfer in Dissociated Air," *J. Aeron. Sci.*, vol. 25, no. 2, Feb. 1958, pp. 73–85.

3 Kemp, N. H., Rose, P. H. and Detra, R. W., "Laminar Heat Transfer Around Blunt Bodies in Dissociated Air," *J. Aero/Space Sci.*, vol. 26, no. 7, July 1959, pp. 421–430.

4 Lees, L., "Laminar Heat Transfer Over Blunt Nosed Bodies at Hypersonic Flight Speeds," JET PROPULSION, vol. 26, no. 4, April 1956, pp. 259–269.

5 Rose, P. H., Probstein, R. F. and Adams, M. C., "Turbulent Heat Transfer Through a Highly Cooled Partially Dissociated Boundary Layer," *J. Aero/Space Sci.*, vol. 25, no. 12, Dec. 1958, pp. 751–760.

6 Reshotko, E. and Cohen, C. B., "Heat Transfer at the Forward Stagnation Point on Blunt Bodies," NACA TN 3513, July 1955.

7 Baron, Judson R., "The Binary Mixture Boundary Layer Associated with Mass Transfer Cooling at High Speeds," MIT Naval Supersonic Laboratory, Technical Rep. 160.

8 Rubesin, M. W., Pappas, C. C. and Okuno, A. F., "The Effect of Fluid Injection on the Compressible Turbulent Boundary Layer—Preliminary Tests on Transpiration Cooling of a Flat Plate at M = 2.7 With Air as the Injected Gas," NACA TN A55119, Dec. 21, 1955.

9 Pappas, C. C., "Effect on Injection of Foreign Gases on the Skin Friction and Heat Transfer of the Turbulent Boundary Layer," IAS Rep. no. 59-78.

10 Bethe, H. A. and Adams, M. C., "A Theory for the Ablation of Glassy Materials," *J. Aero/Space Sci.*, vol. 26, no. 6, June 1959, pp. 321–328.

11 Lees, L., "Similarity Parameters for Surface Melting of a Blunt Nosed Body in a High Velocity Gas Stream," ARS JOURNAL, vol. 29, no. 5, May 1959, pp. 345–354.

12 Schlichting, H., "Boundary Layer Theory," McGraw-Hill Book Co., N. Y., 1955, chaps. IV and XII.

13 Sutton, G. W., "The Hydrodynamics and Heat Conduction of a Melting Surface," *J. Aeron. Sci.*, vol. 25, no. 1, Jan. 1958.

14 Corning Glass Works, "Properties of Selected Commercial Glasses," Corning Glass Works, 1957, Bulletin B-83, Corning, N. Y.

15 Kadanoff, Leo P., "Radiative Transport Within an Ablating Body," Avco Research Laboratory, Research Rep. 37, Oct. 1958.

16 Kadanoff, Leo P., "Radiative Transport Within an Ablating Body," Avco-Everett Research Laboratory, Research Rep. 61, July 1959; ASME Paper no. 60-HT-2 (to be published in *J. Heat Transfer*).

17 Georgiev, S., Hidalgo, H. and Adams, M. C., "On Ablation for the Recovery of Satellites," Avco Research Laboratory, Research Rep. 47, March 1959.

18 Detra, R. W. and Hidalgo, H., "Generalized Heat Transfer Formulae and Graphs," Avco Research Laboratory, Research Rep. 72, May 1958.

19 Stetson, K. F., "Boundary Layer Transition with Highly Cooled Boundary Layers," Avco Research Laboratory, Research Rep. 41, Jan. 1959; IAS Rep. no. 59-36.

Materials for Re-Entry Heat Protection of Satellites

LEO STEG[1]

General Electric Co.
Philadelphia, Pa.

It has now been demonstrated that ablation techniques are capable of providing heat protection for ICBM vehicles during hypersonic re-entry into Earth's atmosphere. In this paper, the application of ablation to satellite re-entry is considered. The four types of materials suitable for ablation are discussed: A material which gasifies but does not liquefy; a material which reacts at its surface with the constituents of dissociated air; a material which melts and vaporizes; a material which partially gasifies, the remaining material being removed by surface combustion. The result of a theoretical analysis of ablation for a typical satellite re-entry trajectory is presented together with some experimental data for materials of the four types, namely Teflon, graphite, quartz and phenolic-nylon. The satellite re-entry environment was simulated in an electric arc driven tunnel. Comparison is also made between results in low heat transfer and high heat transfer test environments to illustrate differences in behavior between steady-state and nonsteady-state ablation. On the basis of the analysis and experiments presented, it appears that little ablation of the materials considered will occur during the ballistic re-entry of a blunt nonlifting vehicle from a satellite orbit. The selection of materials for heat protection can, therefore, be strongly influenced by other criteria.

SEVERAL techniques for heat protection of high speed re-entry ballistic vehicles have been successfully demonstrated. Some questions remain as to the suitability of these techniques and associated materials to the less severe but longer re-entry phase associated with nonlifting satellites (Fig. 1).

A typical re-entry satellite trajectory utilized herein is shown in Fig. 2. With this trajectory and a blunt configuration (R_B = 3.33 ft), the boundary layer will be laminar over a large portion of the nose. A number of correlation formulas for the prediction of heat transfer exist (1–4).[2] The typical heating cycle used is shown in Fig. 3 and is based on an exact solution of the boundary layer equations by Scala (4). Three basic types of heat alleviation schemes are the heat sink (5,6), forced mass transfer systems (4) (e.g., transpiration cooling devices) and self-regulating mass transfer systems (e.g., ablation).

Ablation (7–13) has proven to be an attractive method for the thermal protection of high speed re-entry vehicles with their associated sharp and short heat pulse. The application of this technique to the longer heat pulses and less severe heating rates associated with satellites is considered herein.

Ablation Materials

Some generally desirable characteristics of ablation materials are as follows:

1 In general, gasification during ablation is desirable. The large amount of gas generated thickens the boundary layer and reduces the rate of heat transfer. Gasification products of low molecular weight enhance this effect because of their larger heat capacity and larger diffusion coefficients (14).

2 Ablation materials should have good thermal insulation characteristics so that the ablation process, the loss of structural strength resulting from heating beyond the ablation zone, and the effect of local irregularities during ablation, are confined to the surface.

3 Ablation materials should have a high resistance to thermal and mechanical shock and be easy to fabricate in large sizes.

Materials of interest may be grouped as follows:

1 Plastics which depolymerize to a gas but do not liquefy (e.g., Teflon).

2 Materials which sublime and react with the constituents of dissociated air (e.g., graphite).

3 Materials which first melt and then vaporize (e.g., glass).

4 Composite materials, such as reinforced plastics which pyrolyze and char (e.g., phenolic-nylon).

The stagnation point ablation characteristics of these materials are analyzed in the following sections.

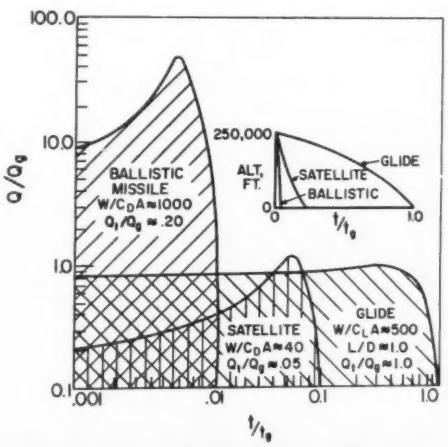

Fig. 1 Typical re-entry heating cycles

Presented at the ARS Semi-Annual Meeting, June 8–11, 1959, San Diego, Calif.

[1] Manager, Space Sciences Laboratory, Missile and Space Vehicle Dept. Member ARS.

[2] Numbers in parentheses indicate References at end of paper.

Pure Gasification—Teflon

The ablation of Teflon appears to occur by a first-order reaction in which the polymer depolymerizes into a monomer (15). The monomer has a very high vapor pressure, so that under most conditions it will flash directly to the vapor. During this process, about 750 Btu/lb are absorbed. In the presence of high temperature air, the monomer may burn to form COF_2 or $CO + F_2$.

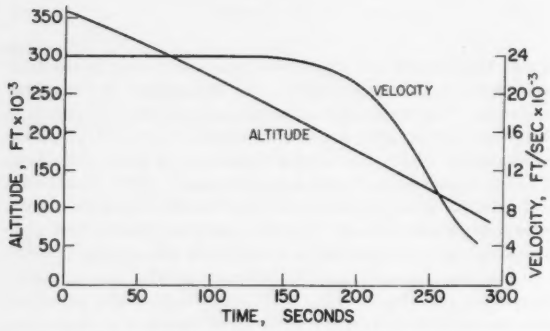

Fig. 2 Typical re-entry satellite trajectory

Fig. 3 Aerodynamic heating of a typical re-entry satellite

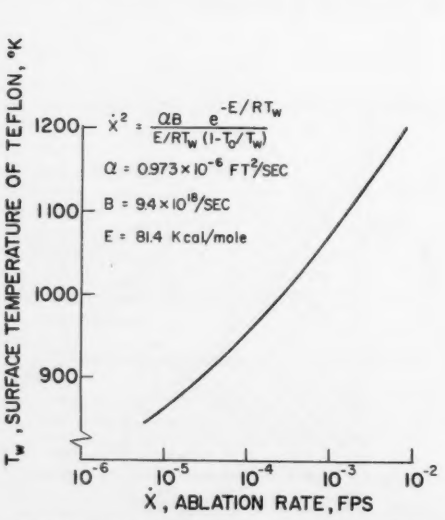

Fig. 4 Variation of surface temperature with ablation rate for steady-state ablation of Teflon

The first published theoretical analysis (16) considered hypersonic Couette flow over a Teflon wall assumed to be at uniform temperature. It has been found experimentally, however, that during the ablation process the material is still at the initial temperature a few millimeters below the surface and that a steep temperature gradient exists near the surface. The process is quite complex, and is described by the generalized heat conduction equation

$$\rho_p C_{p_p}(\vec{v}\cdot\nabla T + \partial T/\partial t) = Q_p + \nabla\cdot K\nabla T \qquad [1]$$

where

Q_p = heat absorbed per unit volume by the action of depolymerization

$\vec{v}$ = the apparent motion of the Teflon with respect to a coordinate system which is at rest with respect to the ablating surface at the stagnation point

Equation [1] can be simplified to obtain an approximate qualitative relationship between the ablation rate $\dot{x}$ and the surface temperature of the Teflon T_w. Over a large portion of any re-entry trajectory, the Teflon appears to be ablating in quasi-steady state, so that $\partial T/\partial t = 0$. In addition, temperature gradients parallel to the surface are small in comparison to those normal to the surface. Since the temperature gradients are largest at the surface and Q_p is an Arrhenius function of temperature, most of the heat absorption by depolymerization occurs near the surface; hence, Q_p can be assigned to the surface itself. The first-order reaction rate then yields

$$\dot{x} = \int_0^\infty Be^{-E/RT}\,dx \qquad [2]$$

where

$E = 81{,}400 \pm 900$ cal/mole

$B = (9.4\ ^{+7.4}_{-4.2}) \times 10^{18}\ \text{sec}^{-1}$

Combination of Equations [1 and 2] and integration using constant thermal properties yield the following relation between $\dot{x}$ and T_w

$$\dot{x}^2 = \alpha_p Be^{-E/RT_w}/(E/RT_w)(1 - T_0/T_w) \qquad [3]$$

The plot in Fig. 4 indicates that the surface temperature is relatively insensitive to the ablation rate $\dot{x}$.

This insensitivity makes the Teflon ablation problem simple to evaluate. A laminar boundary layer analysis (17,18), in which all species are assumed to have the same physical properties and the pressure gradient is neglected, yields the following expression for the energy transfer in the presence of mass transfer of a combustible gas

$$-(K\,\partial T/\partial x)_{pw} = C_H(\dot{m})\rho_e u_e(H_{e_{air}} - H_{w_{air}} + \Delta H_0 C_{0e}) \qquad [4]$$

For steady-state ablation

$$-(K\,\partial T/\partial x)_{pw} = \dot{m}\Delta H_p \qquad [5]$$

Hence

$$\dot{m}/[C_H(\dot{m})\rho_e u_e] = [H_{e_{air}} - H_{w_{air}} + \Delta H_0 C_{0e}]\,\Delta H_p^{-1} \qquad [6]$$

Since the wall temperature is insensitive to the ablation rate, H_w and ΔH_p may be taken at some average value, and Equation [6] yields the ablation rate directly.

For mass transfer into a laminar boundary layer, Stewart (14) has correlated the results of theoretical analyses to obtain the following expression for the Stanton number

$$C_H(\dot{m}) = C_H(0) - 0.72\left(\frac{\dot{m}}{\rho_e u_e}\right)\left(\frac{C_{p_{inj}}}{C_{p_{air}}}\right)^{0.4} \qquad [7]$$

where $(C_{p_{inj}}/C_{p_{air}})$ is effectively $29/M_{C_2F_4}$. If the heat transfer

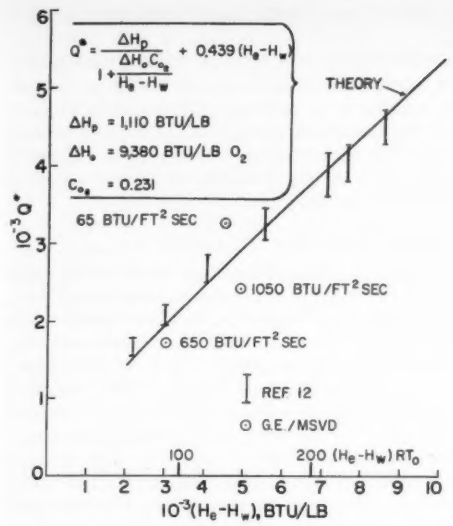

Fig. 5 Heat of ablation of Teflon

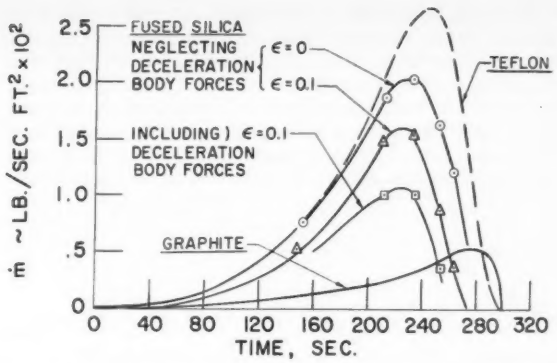

Fig. 6 Material ablation rates for re-entry satellite trajectory

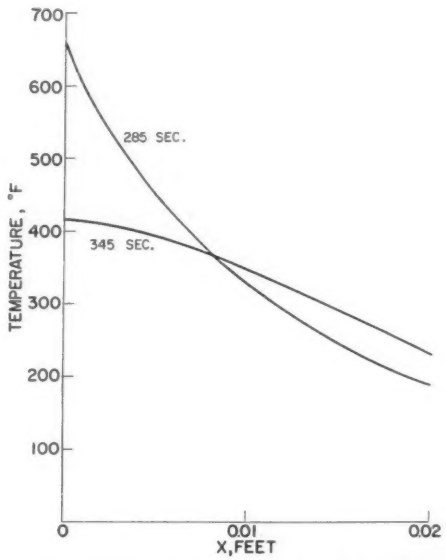

Fig. 7 Temperature profiles in Teflon after ablation ends

given by Equations [6 and 7], is equated to the product of the enthalpy increase of the plastic and the steady-state mass transfer rate, the following expression for steady-state value of the heat of ablation is obtained

$$Q^* = \frac{\Delta H_p}{1 + \Delta H_0 C_{0_e}/(H_e - H_w)_{\text{air}}} + 0.439(H_e - H_w)_{\text{air}} \qquad [8]$$

With T_w taken at an average of 1340 F, T_0 = 100 F, C_{p_p} = 0.30, ΔH_v = 738 Btu/lb, ΔH_p is equal to 1110 Btu/lb. The heat of ablation of Teflon is shown in Fig. 5 for which a value of ΔH_0 = 9380 Btu/lb was used. If combustion is ignored, the theoretical prediction is too large by 20 per cent at the lower enthalpies. At high enthalpy levels (i.e., significant portion of trajectory), the theory of (4) may be used for the energy transfer to the surface

$$Q = Q_{\dot{m}=0} - 0.48\,(H_e - H_w)_{\text{air}}\,\dot{m} \qquad [9]$$

The transient heat conduction equation has been solved using Equation [9] and the method of (19) for the re-entry trajectory heating rate shown in Fig. 3. The resulting ablation rate is shown in Fig. 6. Some temperature profiles are shown in Fig. 7. Total ablation is 0.2 in.

Surface Combustion—Graphite

Graphite is typical of the class of materials which undergo surface combustion (20).

In the absence of detailed reaction rate data, a simple model for the complex C—O—N system is employed, and certain simplifying mathematical assumptions are generally made.

The following assumptions were made in the analysis performed by Scala (21):

1 The gas phase can be approximated by a three-component mixture, consisting of nitrogen, atomic oxygen and carbon monoxide.

2 Gas phase reactions are assumed frozen.

3 Nitrogen reactions do not occur at the surface.

4 The surface combustion product is carbon monoxide.

5 The Lewis and Prandtl numbers are constant and equal to 1.2 and 0.75 respectively.

It can then be shown that the ablation rate of graphite at the stagnation point of an axially symmetric body is given by

$$\dot{m}_w \cong 0.1\sqrt{2\rho_{gw}\mu_{gw}\beta} \qquad [10]$$

This solution applies when the slowest, and hence rate-determining, step is the process of diffusion and counter-diffusion, where the ablation rate depends very little on the surface temperature.

Assuming a Newtonian pressure distribution over the body, Equation [10] may be further simplified to the form

$$\dot{m}_w\sqrt{R_B} = 5 \times 10^{-6}\sqrt[4]{P_e^3/\rho_e} \qquad [11]$$

Substitution of typical satellite re-entry pressures and densities into Equation [11] yields the values of $\dot{m}_w$ shown in Fig. 6. Thus, in the case of satellite re-entry, graphite has such low thermal erosion characteristics that it may be considered primarily as a heat sink material which undergoes oxidation reactions with the environment.

Considering heat transfer into the interior of the graphite, an energy balance reveals that

$$-\left(K\frac{\partial T}{\partial x}\right)_{sw} = Q_{\text{aero}} - \left[\left(\frac{\Delta Q}{\Delta \dot{m}}\right)_w + H_{gw} - H_w(s)\right] \qquad [12]$$

Since the instantaneous combustion rate $\dot{m}_w$ is very small during satellite re-entry, the ablation process should not alter the heat transfer to the surface appreciably. Further, since H_{gw} actually can be a negative quantity (it contains a rather large negative heat of formation of the combustion products), it has been found that for the most severe flight conditions, the chemical heat release actually exceeds the heat blocking term owing to boundary layer thickening, so that $-(K \times \partial T/\partial x)_w$ is approximately 20 per cent larger than Q_{aero} at worst.

Thus, the design of a thermal shield utilizing graphite is limited not by its ablation rate, but rather by the heat penetration aspects and, consequently, mechanical limitations, such as thermal shock and shield fastening problems. The front and back wall temperatures of a layer of graphite 0.10 in. thick, with a surface emissivity of 0.8, are shown in Fig. 8, for the case of variable thermal conductivity.

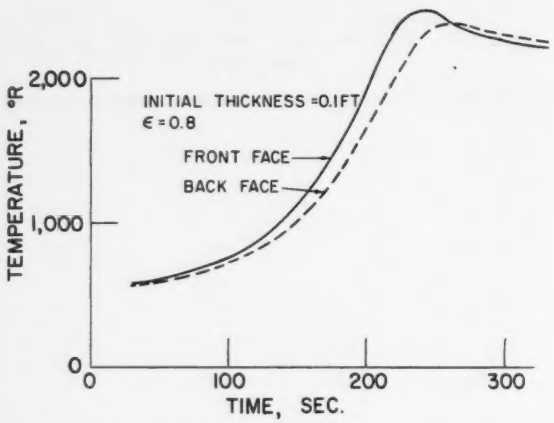

Fig. 8 Front and back wall temperatures of graphite for re-entry satellite

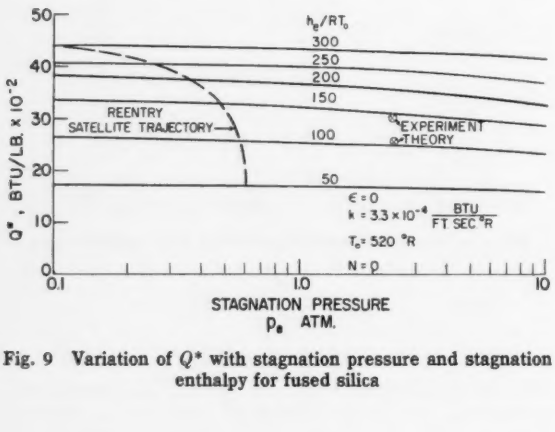

Fig. 9 Variation of Q^* with stagnation pressure and stagnation enthalpy for fused silica

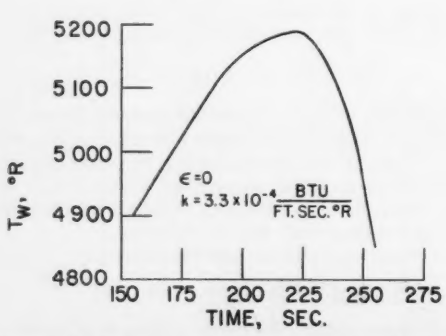

Fig. 10 Surface temperature history for fused silica

Melting and Vaporization—Glasses

There are few practical materials which sublime directly or which have sufficiently high vapor pressures at their melting point to give flash vaporization. To obtain appreciable vaporization, with its associated heat absorption and boundary layer thickening, materials are required whose melt is highly viscous, so that the liquid can be heated to near-boiling temperatures before aerodynamic forces remove it. Such materials are by their very nature glasses, e.g., liquids which are viscous enough so that they may be supercooled without having their molecules falling into the ordered array of a crystal. Data on glasses indicate that fused silica has the highest viscosity, and under certain conditions this material has given evidence of superior ablation characteristics (7,11).

In addition, high silica content glasses are quite resistant to thermal shock. They are, however, transparent to infrared radiation, and consequently often have additives dispersed throughout to absorb or scatter both incoming radiation and self-radiation from the heated surface.

When vaporized, silica forms both the gaseous dioxide and monoxide, in the following highly endothermic reactions

$$SiO_2(s) \rightleftharpoons SiO_2(l) \rightleftharpoons SiO(g) + \tfrac{1}{2}\, O_2(g)$$
$$SiO_2\,(s) \rightleftharpoons SiO_2(l) \rightleftharpoons SiO_2(g) \qquad \ldots\ldots [13]$$

With the formation of a liquid phase, the effect of body forces owing to deceleration of the vehicle during re-entry must be considered. The body forces can slow the liquid sufficiently so that it detaches from the surface somewhere downstream, leading to a decrease in Q^*.

Fanucci and Lew (22) analyzed the flow of a liquid layer with vaporization under the influence of a gaseous hypersonic boundary layer (laminar or turbulent, depending on the region of the body concerned), taking proper account of the history of the flow from the stagnation point. Some results of the characteristics of the liquid phase at the stagnation point of the satellite vehicle have been matched with an analysis by Scala (23) for the dissociated hypersonic boundary layer with mass addition to obtain the rate of ablation of the surface, the fraction vaporized Γ and the effective heat of ablation Q^*.

The heats of ablation for steady-state conditions are shown in Fig. 9. An increase in stagnation pressure causes the surface temperature to rise, resulting in a decrease of the viscosity of the liquid layer and a decrease in Q^*. The lessened viscosity causes more material to flow downstream under the influence of aerodynamic forces, resulting in a smaller gasification ratio. On the other hand, Q^* increases in a nearly linear fashion with increasing stagnation enthalpy because the higher heat transfer rates at high stagnation enthalpies force more of the liquid to vaporize.

The variation of Q^* along the trajectory of the re-entry satellite is indicated in Fig. 9. The associated surface temperatures are shown in Fig. 10. There is little surface temperature variation for steady flight at each altitude and velocity of the re-entry satellite trajectory. It is clear that during the actual trajectory the initial temperature of the silica is low, and no ablation will occur until the silica is heated above its softening point. This occurs at about 160 sec (see Fig. 3) when the ablation process begins.

A study of the effects of deceleration, and hence of body forces, indicates that Q^* is increased and the net mass loss over a trajectory is decreased. This effect is shown in Fig. 6 and is not negligible even though the rate of deceleration is low. Surface reradiation will decrease the net heat transfer to the surface. In Fig. 6 it also may be seen that a very modest emissivity of 0.1 decreases the ablation rate by about 20 per cent. If the surface emissivity is unity, then the equilibrium temperatures will be 3470 R for the case of no heat conduction into the interior. Under these conditions, the silica probably will not ablate but will act merely as a reradiating surface. If the thickness is sufficiently large, then the silica will act as a heat sink, with a maximum surface temperature of 2800 F. A heat sink calculation yields a maximum value of the net heat transfer of 28 Btu/ft²-sec and a heat pulse of about 5000 Btu/ft². The thickness of silica required to yield a final back face temperature rise of 200 F is about 7 in., and is inversely proportional to the final back face temperature rise; a thickness of 1 in. will yield a back face temperature rise of 1400 F. On this basis, it appears more desirable to have the emissivity of the silica less than unity so that a surface temperature sufficiently high to cause ablation is reached, resulting in a decrease of the net heat content of the remaining silica. Thus quartz, when utilized as a heat sink, is relatively inefficient.

Nonequilibrium effects have been considered by Scala and Vidale (24,25). It was found that rate controlled vaporization tends to increase the surface temperature resulting in a decrease of Γ and Q^* above 200,000 ft. For the vehicle and the trajectory shown in Fig. 2 the effect is not significant, since ablation probably will not begin at altitudes above 200,000 ft.

Reinforced Plastics

Reinforced plastics include some of the most attractive materials for use in satellite re-entry. Certain of the phenolic, silicone and melamine resins are suitable plastics (7); 91LD resin (Cincinnati Testing Laboratories), for example, has shown good characteristics experimentally. When heated, this resin pyrolyzes into a gas and a carbonaceous structure which shrinks in dimension. Preliminary experiments indicate that the gas is composed of hydrogen, methane and carbon dioxide. Combustion may occur between methane and oxygen to form CO_2, H_2O, OH and CO. The latter three then may react with and chemically erode the carbonaceous structure to form CO and CO_2. Suitable reinforcements include "E" glass, Refrasil (a form of silica: H. T. Thompson Co.) and nylon (7,11).

Phenomenological behavior in this class varies significantly with time and magnitude of heating. For the application under consideration, the nylon reinforced plastic pyrolyzes to form a moderately thick, low density, charred layer which, in general, has shrunk dimensionally and which may have been chemically eroded at the surface. The surface temperature of the char layer may become sufficiently hot to reradiate most of the aerodynamic heat. The heat damage thus propagated into the material is caused by the aerodynamic heat transfer and by the heat released during combustion or chemical reaction within the char and adjacent layer.

For glass and Refrasil reinforcement, char depth was found experimentally to be about twice that of the nylon reinforcement. When inorganic fibers are used as reinforcement, the plastic tends to delaminate and grow in dimension (13). The local rate at which unpyrolyzed plastic is pyrolyzed is given by

$$\frac{\partial \rho_{vp}}{\partial t} + \bar{v} \cdot \nabla \rho_{vp} = -B \rho_{vp} e^{-E'/RT} \qquad [14]$$

The total rate of pyrolysis is given by

$$\int_0^\infty \rho_{vp} B e^{-E'/RT} dx \qquad [15]$$

The local rate of heat absorption is given by

$$Q_p = \rho_{vp}\, \Delta H_v e^{-E/RT} \qquad [16]$$

Thus the problem of predicting the rate of pyrolysis of the plastic is quite complex. Steady-state ablation does not appear probable for re-entry satellites protected by reinforced plastics. Therefore, redefining Q^* by $Q^* = Q_{(\dot{m}=0)}/\dot{m}_p$, where $\dot{m}_p$ is the rate at which mass is pyrolyzed but not necessarily removed, Scala has obtained the expression

$$Q^* = (\Gamma + \Xi)\left[\left(\frac{\Delta Q}{\Delta m}\right)_w + H_{vw}\right] - H_{vp} \qquad [17]$$

To evaluate Q^*, the chemistry of the interaction between the material and dissociated air must be considered.

If pyrolysis occurs in a vacuum, then $\Gamma \dot{m}_p$ represents the rate of gasification, and $1 + (1 - \Gamma)\dot{m}_p$ represents the rate of formation of char, where $\dot{m}_p$ is the rate of pyrolysis. During hypersonic re-entry, however, oxygen diffuses toward the surface and oxidation reactions occur. The rate of gasification is then given by $(\Gamma + \Xi)\dot{m}_p$, and the instantaneous rate of char formation is $(1 - \Gamma - \Xi)\dot{m}_p$. Char is continuously formed at an interface between the virgin plastic and the pyrolyzed layer, and, if sufficient oxygen diffuses to the surface, is consumed at the outer surface. Thus the rate of growth of the char layer depends on:

1 The mass diffusion flux of oxygen from the main stream toward the surface.

2 The quantity and reactivity of the combustible gases produced during pyrolysis which flow into the boundary layer; this, in turn, is controlled by the rate at which heat can be conducted to the virgin plastic.

For the case of ablation of phenolic nylon, an exact solution for air injection into the hypersonic dissociated stagnation point laminar boundary layer yields the following expression for the heat blocked due to mass transfer (23)

$$\left(\frac{\Delta Q}{\Delta \dot{m}}\right)_w = \frac{30}{M_w}\,[240 + 0.48(H_s - H_w)] \qquad [18]$$

This is assumed to be valid for predicting the effects of gas injection containing species other than oxygen and nitrogen. Since the mean molecular weight of the gas at the surface appears in the denominator, the injection of lightweight gases, such as hydrogen, enhances the blocking term.

If nylon is utilized as a resin, it melts, vaporizes and reacts without leaving a char residue (11), whereas phenolic-resin decomposes to form a char residue. Nylon and phenolic-resin combined in equal amounts by weight may be represented by the empirical formula $C_{13}H_{18}O_2N$. The behavior of the composite material is such that lightweight gases are released during pyrolysis and a char layer is formed which enhances reradiation from the surface.

A theoretical analysis of the ablation of phenolic-nylon, utilizing the boundary layer equations, is complicated by the large number of different chemical species which are the original products of pyrolysis and by the subsequent combustion reactions between these species and the components of dissociated air. Experimental data (11) indicate that under vacuum conditions $\Gamma \backsimeq 0.7$. Hence, $0.7 < (\Gamma + \Xi) \leq 1$.

The dependence of $(\Delta Q/\Delta \dot{m})_w$, the heat blocking action term, on the mean molecular weight M_w has been noted in the foregoing. If, for example, the final products of gaseous dissociation and combustion are primarily hydrogen, with small amounts of water and carbon monoxide, the heat blocking term can easily be a factor of 2 or 3 larger than the corresponding term for transpiration cooling by air injection. Another effect contributing to Q^* is the magnitude of the gaseous enthalpy at the surface H_w. Combining Equations [17 and 18] indicates that Q^* tends to increase approximately as the additive term $(\frac{1}{2})H_w$. The more hydrogen at the surface, the larger the term H_w will be.

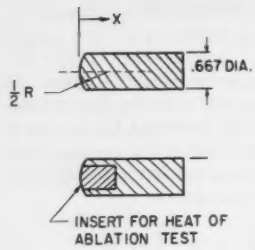

MATERIALS	THERMOCOUPLE LOCATIONS	
	STA. A	STA. B
TEFLON	X=.100	X=.200
PHENOLIC NYLON	.188"	.376"
PHENOLIC REFRASIL	.136"	.272"
PHENOLIC GLASS	.130"	.260"
GRAPHITE	.121"	.242"
WEIGHT OF MATERIAL AHEAD OF EACH T.C.	1.15 #/FT²	2.30 #/FT²

Fig. 11 Schematic of cylindrical models

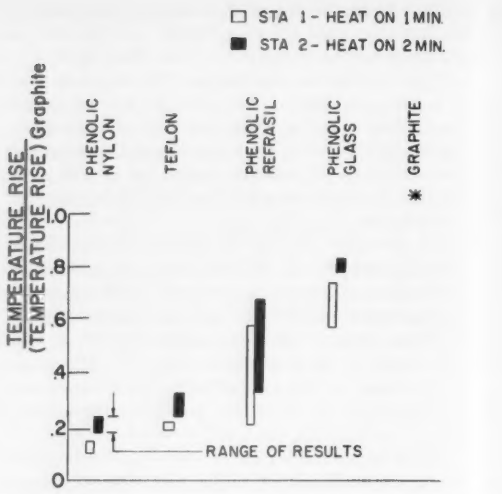

Fig. 12 Relative temperature rise in materials at end of heating cycle

Finally, it is observed that complex hydrocarbons, such as phenolic-nylon, have a negligible heat of formation per unit mass ($H_{vp} \sim 0$).

Evaluating Equation [17] in the light of the foregoing discussion, Q^* may be approximated by (26)

$$Q^* = 1500 + (1/2)H_s \qquad [19]$$

Experimental Results

In high speed re-entry mass loss due to ablation (related to Q^*) is generally the primary consideration; in satellite re-entry the temperature reached at the inner wall surface is perhaps of equal interest. Since conductivities for all of the materials considered here[3] (except graphite) are of the same order of magnitude as the conductivities of the best practical insulators, the self-insulation thickness is a good figure of merit.

In view of theoretical complications introduced by long-time heating (e.g., charring and the prevalence of non-equilibrium phenomena), experimental data are of particular interest.

Experiments were performed in a Mach 4.8 arc heated supersonic wind tunnel at a stagnation enthalpy of 150 RT_0, calorimeter heat transfer rate of 65 Btu/ft² sec and a stagnation pressure of $p_s = 0.026$ atm.[4] Tests were run for 1 and 2 min; the total heat pulse for a 2-min run is comparable to that shown in Fig. 3.

Thermocouples were placed at two positions in the models (Fig. 11) so that the weights of material between the thermocouple and initial surface were 1.15 lb/ft² (location A) and 2.30 lb/ft² (location B). The thermocouples were at locations A and B for the 1-min runs and at B for the 2-min run.

Data obtained at the end of 1 min (thermocouple at A) and 2 min (thermocouple at B) are shown in Fig. 12. The temperature rise at each station at the end of each run is referred to the temperature rise of graphite. It is seen that for both heating intervals, the minimum temperature rise occurs with phenolic-nylon.

In view of the fact that the time from the end of significant heating until impact may be several times as large as the time of heating, temperatures have been recorded after as well as during heating. These data are shown in Fig. 13 for station B for a 1-min initial heating load. It should be noted that heat loss in the tunnel under these conditions is primarily by radiation, so that the convective process and combustion occurring during actual re-entry are not simulated. Although both of these processes probably act in opposite directions, only qualitative conclusions are drawn here. It is seen that, with the exception of graphite, the maximum internal temperature occurs after the heating cycle has been terminated.

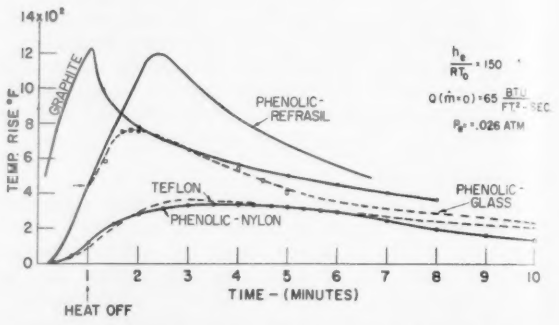

Fig. 13 Temperature histories of material specimens after heat cutoff

The change in position of the temperature rise of Teflon in relation to phenolic-nylon at the end of the 1-min run at stations A and B is of interest (Figs. 12 and 13). The higher temperature of the Teflon at station A probably is due to the greater ablation rate of Teflon in these tests, which brings the surface of the Teflon quite close to station A. The lower temperature of the Teflon at station B indicates that the temperature gradient between station A and station B is greater than that in the case of the phenolic-nylon. Thus, as would be expected, less energy is stored in a material which has a higher ablation rate during the heat pulse. The high surface temperature material will, however, reradiate more of its stored heat after the pulse, so that the penetration of the shield material by heat is reduced. From the data shown in Fig. 13, it appears that this latter effect is responsible for the lower, late-time temperatures in phenolic-nylon. It is possible that the trends shown for Teflon and phenolic-nylon could change for different heating rates, total heating time, shield weight and thickness.

[3] Graphite, types ATJ and ATL; phenolic-nylon, 40 per cent resin by weight; phenolic-Refrasil, 38–42 per cent resin by weight; phenolic-glass, 40–50 per cent resin by weight.

[4] Total carbon contamination approximately 5 per cent by weight.

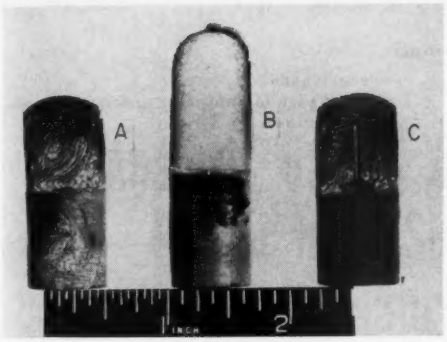

Fig. 14 **Model cross sections—heat soak study: A, phenolic-Refrasil; B, phenolic-nylon; C, phenolic-glass.** p_e = 0.026 atm; H_e/RT_0 = 150; $Q_{\dot{m}=0}$ = 65 Btu/ft²-sec

Table 1 Measured heats of ablation

Material	Q^* (theoretical), Btu/lb	Q^* (experimental),[a] Btu/lb
Teflon	2700	3120
phenolic-nylon	4180	4480
phenolic-Refrasil	...	7530
phenolic-glass	...	9600

[a] Corrected for surface temperature.

Test Conditions
$Q_{(\dot{m}=0)}$ = 65 Btu/ft²-sec
H_e/RT_0 = 150
p_e = 0.026 atm

The measured heats of ablation are shown in Table 1. Although the last two materials exhibit large values, it is not evident that they would be the preferable because of the heat conduction problem, particularly in the case of graphite.

The measured heat of ablation of Teflon is somewhat higher than the value obtained during high heat flux conditions (Fig. 5), probably since heat is conducted into the material faster than it ablates, resulting in

$$\dot{m}\Delta H_p < (K\,\partial T/\partial x)_{pw}$$

Thus, the measured heat of ablation in this test should be larger than the steady-state value in which

$$\dot{m}\Delta H_p = (K\,\partial T/\partial x)_{pw}$$

Nonsteady conduction could also account qualitatively for the value of Q^* for phenolic-nylon, which is larger than the theoretical prediction.

Sections of the models tested are shown in Fig. 14. The formation of a thin layer of solidified glass may be observed on the surface of the phenolic-glass model during the latter portion of the 2-min heating cycle; thus basic phenomenological differences in the ablation process with time are to be expected.

The significant variation in behavior with heating rate for some nonhomogeneous materials is shown in Figs. 15 for melamine glass. Total heat pulses were essentially identical; maximum heating rates differed by a factor of 14. Major differences in characteristics of the char layer are clearly evident. In the case of the low value of maximum heat transfer rate, an extensive fibrous char structure of pyrolyzed plastic exists, covered on the surface by molten reinforcing material. In the case of the high value of the maximum heating rate, the higher ablation rate clearly limited the depth of the remaining char layer, resulting in a higher mass loss, but a relatively undisturbed remaining structure.

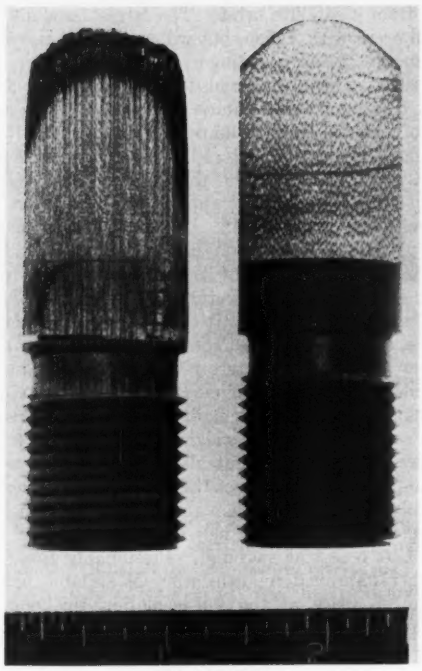

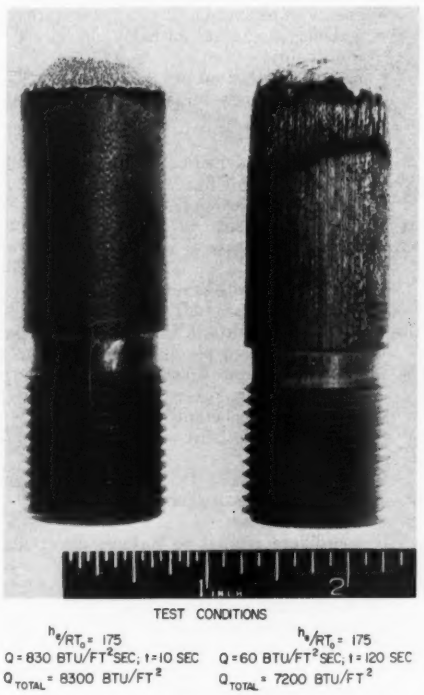
TEST CONDITIONS
h_e/RT_0 = 175
Q = 830 BTU/FT²SEC; t=10 SEC
Q_{TOTAL} = 8300 BTU/FT²
h_e/RT_0 = 175
Q = 60 BTU/FT²SEC; t=120 SEC
Q_{TOTAL} = 7200 BTU/FT²

Figs. 15 Comparison of material behavior at high and low ablation rates

Conclusions

On the basis of the analyses and experiments discussed, it appears that very little ablation of the materials considered will occur during the ballistic re-entry of a blunt nonlifting

vehicle from a satellite orbit. The largest amount of ablation will occur with Teflon, but will amount to less than 3 lb per ft² for the re-entry heating cycle considered.

The selection of the materials for heat protection can therefore be based on other criteria. Foremost of these is the weight of material required for self-insulation, since it appears likely that the ablation material also can serve effectively as the thermal insulator. On this basis, both Teflon and phenolic-nylon qualitatively appear to be the most suitable of the materials investigated. If we also consider structural integrity, the phenolic-nylon has advantages over Teflon, since the recrystallization of Teflon and the concurrent expansion present serious structural problems.

On the basis of conservative estimates, an initial Teflon thickness of 1 in. would be more than adequate to maintain the inner surface temperature rise to a value below 200 F. The same weight of phenolic-nylon would have equivalent performance. The best available heat sink material would require not only a larger weight to absorb the total heat transferred to the body, but also a considerable weight of insulation material to protect the payload from overheating. It is probable, therefore, that an ablation heat shield structure will be approximately half the weight of that required for the best heat sink material. Presumably this ratio can be further improved by utilization of suitable lightweight insulation in place of the self-insulation thickness of the ablation material.

Nomenclature

B = frequency factor for depolymerization
$C_H(\dot{m})$ = Stanton number in the absence of combustion
C_0 = concentration of oxygen
C_p = specific heat at constant pressure
E = energy of activation of depolymerization
H = gaseous stagnation enthalpy, including chemical enthalpy
ΔH_0 = heat of combustion per unit mass of oxygen
ΔH_p = enthalpy change, initial to surface temperature of plastic $= H_{pw}(g) - H_{p0}(s) = \int_{T_0}^{T_w} C_{pp}(s)dt\Delta H_v$
ΔH_v = heat of depolymerization per unit volume for plastic; latent heat of vaporization
K = thermal conductivity
M = molecular weight
$\dot{m}$ = mass transfer rate $= \rho_p \dot{x}$ for steady-state ablation
p = pressure
Q = heat transfer rate to surface
Q^* = heat of ablation $= Q\ (\dot{m} = 0)/\dot{m}_w$
$Q_{(\dot{m}=0)}$ = heat transfer rate in the absence of mass transfer
Q_p = energy absorbed per unit volume due to pyrolysis
$(\Delta Q/\Delta \dot{m})_w$ = change in energy transfer per unit change charge in interphase mass transfer for no combustion
R = universal gas constant
R_B = nose radius of the re-entry satellite
t = time
T = temperature
u = tangential velocity parallel to surface
$\vec{v}$ = velocity vector
x = coordinate normal to surface, direction into the material
$\dot{x}$ = ablation rate
α = thermal diffusivity
α_{vap} = vaporization coefficient
β = stagnation point velocity gradient
Γ = fraction of material ablated which is gaseous
ϵ = total surface emissivity
μ = viscosity
Ξ = fraction of virgin plastic that enters gas phase during surface combustion of char layer
ρ = density

Subscripts

aero = aerodynamic
e = outer edge of gaseous boundary layer, stagnation conditions
g = gas
0 = initial
p = plastic
t = total
vp = virgin plastic
w = wall

References

1 Allen, H. J. and Eggers, A. J., Jr., "A Study of the Motion and Aerodynamic Heating of Missiles Entering the Earth's Atmosphere at High Supersonic Speeds," NACA RM A58D28, Aug. 25, 1953.

2 Kemp, N. H. and Riddell, F. R., "Re-Entry Heat Transfer to Satellite Vehicles," JET PROPULSION, vol. 27, part I, Feb. 1957, pp. 132–137.

3 Romig, M., "Stagnation Point Heat Transfer for Hypersonic Flight," JET PROPULSION, vol. 26, no. 12, Dec. 1956, pp. 1098–1101; Addendum, vol. 27, no. 12, Dec. 1957, p. 1255.

4 Scala, S. M., "The Thermal Protection of a Re-entry Satellite," ASME Aviation Conference, Los Angeles, March 9–12, 1959; *also* ARS JOURNAL, vol. 29, no. 9, Sept. 1959, pp. 670–72.

5 Masson, D. J. and Gazley, C., Jr., "Surface-Protection and Cooling Systems for High-Speed Flight," *Aeron. Engng. Rev.*, vol. 15, no. 11, Nov. 1956, pp. 46–55.

6 Sutton, G. W., "The Temperature History in a Thick Skin Subjected to Laminar Heating During Re-Entry Into the Atmosphere," JET PROPULSION, vol. 28, no. 1, Jan. 1958, pp. 40–45.

7 Sutton, G. W., "The Ablation of Reinforced Plastics in Supersonic Flow," *J. Aero/Space Sci.*, vol. 27, no. 5, May 1960.

8 Scala, S. M. and Sutton, G. W., "The Two-Phase Hypersonic Laminar Boundary Layer—A Study of Surface Melting," Proc. Heat Transfer and Fluid Mechanics Institute, Stanford Univ. Press, Calif., June 1958, pp. 231–248.

9 Bethe, H. H. and Adams, M. C., "A Theory for the Ablation of Glassy Materials," Avco Research Laboratories, Rep. 38, Nov. 1958.

10 Lees, L., "Similarity Parameters for Surface Melting of a Blunt Nosed Body in a High Velocity Gas Stream," ARS JOURNAL, vol. 29, no. 5, May 1959, pp. 345–353.

11 Gruntfest, I. J., "Behavior of Reinforced Plastics at Very High Temperatures—Part 2," *Modern Plastics*, vol. 37, no. 8, April 1959, pp. 137–148, 204.

12 Georgiev, S., Hidalgo, H. and Adams, M., "On Ablation for Recovery of Satellites," Avco Research Laboratory, Research Rep. 47, March 6, 1959; *also* Proc. 1959 Heat Transfer and Fluid Mechanics Institute, Stanford Univ. Press, Calif.

13 "Thermal Protection of Structural Propulsion, and Temperature Sensitive Materials for Hypersonic and Space Flight," Chicago Midway Laboratories Data Rep. CML-DR-M152-2, Oct. 21, 1958.

14 Stewart, J. D., "Transpiration Cooling: An Engineering Approach," General Electric Co., Missile and Space Vehicle Dept., Philadelphia, Pa., TIS Document no. R59SD338, May 1959.

15 Friedman, H., "The Mechanism of Polytetrafluoroethylene Pyrolysis," A.C.S. Meeting, Atlantic City, N. J., Sept. 1959. To be published in *J. Polymer Sci.*

16 Knuth, E., "Compressible Couette Flow with Diffusion of a Reactive Gas, from a Decomposing Wall," in "Proc. 1958 Heat Transfer and Fluid Mechanics Institute," Stanford University Press, Calif.

17 Sutton, G. W., "Adiabatic Wall Temperature Due to Mass Transfer Cooling With a Combustible Gas," JET PROPULSION, vol. 29, no. 2, Feb. 1959, pp. 136–137.

18 Sutton, G. W., "Combustion of a Gas Injected into a Hypersonic Laminar Boundary Layer," in "Proc. Seventh International Combustion Symposium," Butterworths Sci. Pub., London, 1958.

19 Goodman, T. R., "The Heat Balance Integral and Its Application to Problems Involving a Change of Phase," Trans. ASME, vol. 80, no. 2, Feb. 1958, pp. 335–342.

20 Gerstein, M. and Coffin, K. P., "Combustion of Solid Fuels," in "High Speed Aerodynamics and Jet Propulsion, Vol. II," Princeton University Press, 1956.

21 Scala, S. M., "Surface Combustion in Dissociated Air," JET PROPULSION, vol. 28, no. 5, May 1958, pp. 340–341.

22 Fanucci, J. and Lew, H., "Effect of Mass Transfer and Body Forces on Two Phase Boundary Layer," General Electric Co., Missile and Space Vehicle Dept., Philadelphia, Pa., TIS Document no. R59SD380, April 1959.

23 Scala, S. M., "Sublimation in a Hypersonic Environment," *J. Aero/-Space Sci.*, vol. 27, no. 1, Jan. 1960, pp. 1–12.

24 Scala, S. M., "Vaporization of a Refractory Oxide During Hypersonic Flight," Proc. 1959 Heat Transfer and Fluid Mechanics Institute, UCLA, June 1959, pp. 181–192.

25 Scala, S. M. and Vidale, G. L., "Vaporization Processes in the Hypersonic Laminar Boundary Layer," to appear in *International J. Heat and Mass Transfer*, vol. 1, no. 1, 1960.

26 Scala, S. M., "A Study of Hypersonic Ablation," in "Proc. Tenth Int. Astronautical Congress, London," Springer-Verlag, Vienna, 1959.

Analysis of the Ablation of Plastic Heat Shields That Form a Charred Surface Layer

R. J. BARRIAULT[1] and J. YOS[2]

Research and Advanced Development Div., Avco Corp., Wilmington, Mass.

The ablation of plastic heat shields that form a charred surface layer under extreme aerodynamic heating is analyzed. The model chosen for this type of ablation consists of a porous outer layer through which there is a counterflow of gases from the thermal decomposition of the plastic. The charred layer is backed by a semi-infinite layer of the undecomposed solid. The transpiring gases are considered to be in thermal equilibrium with the skeleton of the porous material. The heat transfer equations are set up, and the steady-state solution obtained. The formulas for the steady-state temperature distributions, charred layer thickness and heat of ablation in terms of model parameters and variables of the thermal environment are derived. An approximate formula is also derived for the induction time of the nonsteady phase of ablation.

Description of the Model

UNDER conditions of extreme aerodynamic heating, heat shielding may be accomplished by consumption of the shielding material (1).[3] This is known as ablation. During the ablation of many materials containing organic matter, such as plastics or resins, a porous charred layer is formed on the surface (2,3). This layer may attain a thickness of several millimeters in the quasi-steady state. It complicates the heat transfer problem not only because it introduces a second phase between the original solid and the boundary layer, but also because it contains a counterflow of gases from the decomposing solid.

In addition to the usual outside heat transfer surface next to the aerodynamic boundary layer, we have in this case another boundary to consider between the charred layer and the original solid where a sharp change in properties occurs as well as an absorption of heat ΔH_c by chemical decomposition. We can therefore expect a discontinuity in the temperature gradient at that second interface. During ablation, both interfaces will be moving. In the transient phase, the two interface velocities will be unequal.

The geometry of the model and the temperature distributions are illustrated schematically in Fig. 1. The frame of reference T, X is considered fixed relative to the material of the original uncharred plastic. Another frame of reference T''_l, X''_l is specified to move with the front surface of the charred layer at $x = s_l$. A third frame of reference T'_s, X'_s is specified to move with the back surface of the charred layer (i.e., the front surface of the original solid) at $x = s_s$. We therefore have the relation

$$L = s_s - s_l \qquad [1]$$

between the thickness of the charred layer L and the locations of the two surfaces, which are given by

$$s_s = \int_0^t v_s(t)\, dt \qquad [2]$$

$$s_l = \int_0^t v_l\,(t)\, dt \qquad [3]$$

where $v_s(t)$ and $v_l(t)$ are the velocities of the front surfaces of the solid and the layer, respectively.

We will assume that the charring process is such that

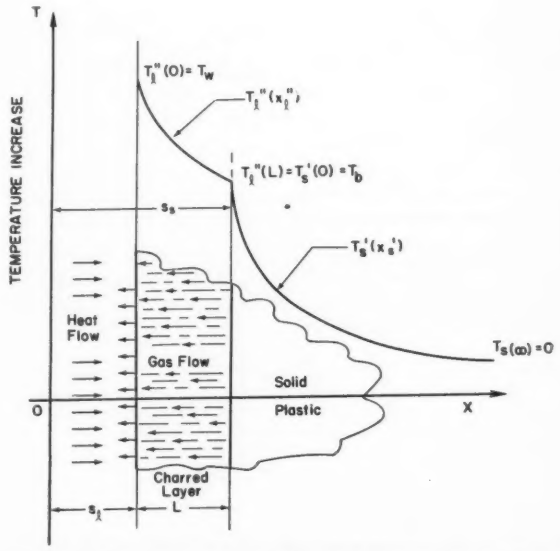

Fig. 1 Schematic illustration of the model for ablation of plastics that form a charred layer, with temperature distribution

Received March 8, 1960.

[1] Chief, Physical Chemistry Section.

[2] Senior Scientist, Theoretical Physics Group.

[3] Numbers in parentheses indicate References at end of paper.

voids are formed in the plastic in such a way that there is no overall shrinkage and that the material points in the two solid phase structures do not move relative to each other. We can therefore use a common, fixed frame of reference for the two solid phases. One of the consequences of this assumption is that

$$m_g = m_s(\rho_s - \rho_l)/\rho_s \quad [4]$$

$$m_s = \rho_s v_s \quad [5]$$

We also need to make some assumptions about the structure and properties of the porous charred layer and about the nature of the gas flow and its interaction with the solid skeleton of the layer. These assumptions are that the size of the voids which constitute the porosity of the charred layer is sufficiently small, compared with the charred layer thickness, so that the counterflowing gases are always at the same temperature as the solid skeleton at corresponding points where they are in contact, regardless of the magnitude of the temperature gradient. Weinbaum and Wheeler (4) have analyzed the problem without the latter assumption and showed that the gas temperature rises very quickly (within a layer about one pore diameter in thickness) after it enters at the back of the porous structure. We also assume that the gas flow is unimpeded by the porous layer; this means that the flow rate and gas pressure are not functions of the coordinate x. We will neglect heat transfer by radiation across the voids and by back diffusion in the gas stream.

Finally, we will assume that the thermal and physical properties of the three phases are constants, independent of temperature. We will, in particular, define the properties of the porous layer, such as its density ρ_l, thermal conductivity K_l and heat capacity C_l, to include the gas enclosed in its pores under conditions of no gas flow.

It is the assumption of constant properties in particular that make the model an idealized one. These properties are expected to vary with temperature and/or depth in the material (3). For engineering estimates of ablation behavior, however, it will be justified to use the formulas so derived with average or equivalent-model values of the basic parameters. Moreover, this ideal model can be expected to demonstrate the essential characteristics of real material ablation in a general way if not in detail.

Ablation Without Charred Layer Formation

The heat transfer relations for a body that ablates without forming a liquid or charred layer are known (5). They will be reviewed here since they form part of the solution of the present problem. The discussion will also serve as an introduction to the important concepts of ablation used in the analysis of our model.

Heat Transfer Relations in a Frame of Reference That Is Stationary With Respect to the Material of the Body

In Fig. 2, the coordinate system T, X is stationary with respect to the material of the body. The conventional heat transfer equations for a one-dimensional case are applicable in this coordinate system

$$k\frac{\partial^2 T}{\partial x^2} = \frac{\partial T}{\partial t} \quad [6]$$

$$k = K/\rho C \quad [7]$$

$$q(x) = -K(\partial T/\partial x) \quad [8]$$

where

T = temperature increment above initial temperature
t = time
ρ = density
C = heat capacity
K = thermal conductivity
$q(x)$ = heat flux in the positive direction at the station x

K, C and ρ are assumed to be constants. In this frame of reference, ablation is represented by the motion of the boundary condition at the surface of the solid $q(x_0)$ which must allow for heat absorbed by any phase changes that may occur.

In later discussions, it will be useful to consider the heat flux at x in terms of the increase in enthalpy H in the region to the right of a fixed vertical surface at x

$$H = \rho C\int_x^\infty T(x)dx = \int_0^t \frac{dH}{dt}\,dt \quad [9]$$

Since enthalpy must be conserved, the rate of increase in H must equal the heat flux across the surface

$$q(x) = \frac{dH}{dt} = \rho C\int_0^\infty \frac{\partial T(x)}{\partial t}\,dx \quad [10]$$

Heat Transfer Relations in a Frame of Reference That Moves With the Ablating Surface

In Fig. 2, the coordinate system T',X' is moving with respect to the stationary system T,X (and with respect to the material of the body) at a speed $v(t)$ which need not be constant. The relationship between coordinates in the two frames of reference is therefore given by the two equations

$$x' = x - s \quad [11]$$

$$s = \int_0^t v(t)dt \quad [12]$$

The temperature is the same at corresponding points in the two coordinate systems at all times. Therefore all slopes and curvatures are the same at corresponding points in the two systems. The time derivatives of T are different in the two systems and are related by the usual equation for the convective change (6)

$$\frac{\partial T(x)}{\partial t} = \frac{\partial T'(x')}{\partial t} - v(t)\frac{\partial T(x)}{\partial x} \quad [13]$$

The equation for the convective change, when applied to the heat flux as defined by Equation [10], leads to the relationship between the heat fluxes in the two frames of reference

$$q'(x') = q(x) - \rho C v(t) T(x) \quad [14]$$

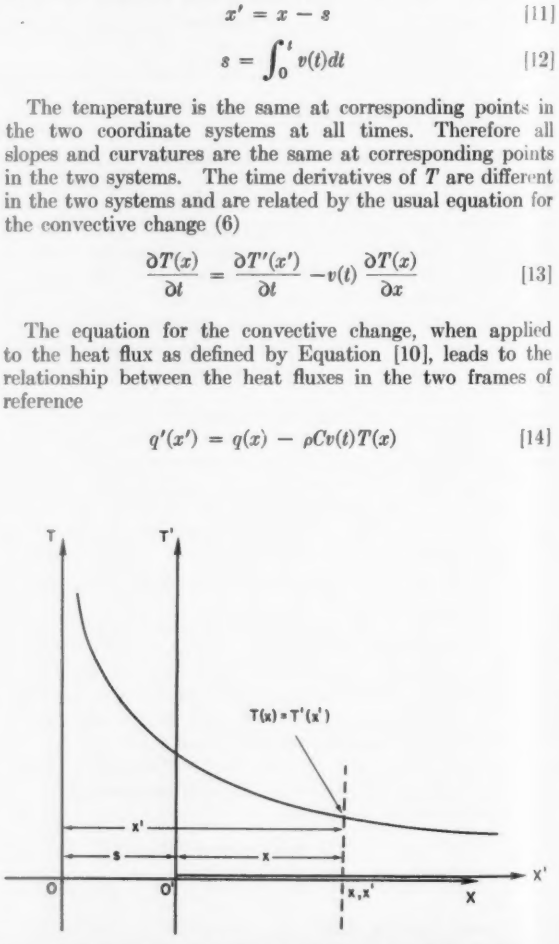

Fig. 2 Temperature distribution in heat transfer system in two frames of reference moving with respect to each other

$\rho Cv(t)T(x)$ is the rate of enthalpy loss across the surface at x' in the T',X' coordinate system due to the material's relative backward motion.

In order to obtain the heat transfer equations in this coordinate system, one merely needs to substitute Equations [13 and 14] in Equations [6 and 8] with $x = x'$. The form of the boundary conditions will be discussed in the next section.

Ablation With Vaporization Under Aerodynamic Heating Conditions

In the case of vaporization during ablation under aerodynamic heating, the net aerodynamic heat input is a boundary condition that moves with the ablating surface and can be related to $q'(0)$ which is given by (7,8,9)

$$q'(0) = q(\text{aerodynamic}) - q(\text{transpiration}) - q(\text{radiation}) - m_v H_T \quad [15]$$

where

$$q(\text{aerodynamic}) = C_{H0}\rho_e U_e(h_e - h_s) \quad [16]$$

$$q(\text{transpiration}) = m_v\eta(h_e - h_s) \quad [17]$$

$$q(\text{radiation}) = \sigma\epsilon[T'(0)]^4 \quad [18]$$

$$m_v = \rho v(t) \quad [19]$$

ρ_e = gas density at edge of boundary layer
η = constant of the gas
m_v = mass flow or ablation rate
H_T = latent heat of vaporization plus the sensible enthalpy of solid at $T'(0)$

q(transpiration) represents the "transpiration" or "blowing" effect, which is the amount that the aerodynamic heating rate is reduced by the countercurrent of gases from the vaporization of the solid. This is a complex phenomenon that has been the subject of much theoretical analysis (7). Rigorous solutions of the boundary layer equations are very cumbersome and require extensive material properties that are usually not available. Fledderman (8) has suggested Equation [17] is an approximation of sufficient accuracy for simple engineering analysis. The constant η varies approximately as $M^{-1/3}$ or $M^{-1/4}$, where M is the molecular weight of the gas.

From Equations [8 and 14], we can write the boundary condition at the surface for the heat transfer equations in the stationary frame of reference as

$$-K\left.\frac{\partial T}{\partial x}\right|_s = (C_{H0}\rho_e U_e - m_v\eta)(h_e - h_s) - \sigma\epsilon[T(s)]^4 + \rho Cv(t)T(s) - m_v H_T \quad [20]$$

The sensible enthalpy was included in H_T to keep Equation [20] in a form related to Equation [14]. There will be a cancellation of sensible enthalpy between the last two terms of Equation [20]. This complication arises from the introduction of a phase change into the model.

Because of Equations [13 and 14], we can write the differential equations for the temperature distribution in the moving frame of references as

$$k\frac{\partial^2 T'}{\partial x'^2} + v(t)\frac{\partial T'}{\partial x'} = \frac{\partial T'}{\partial t} \quad [21]$$

$$q'(x') = -K(\partial T'/\partial x') - \rho Cv(t)T'(x') \quad [22]$$

The upstream boundary condition is

$$-K\left.\frac{\partial T'}{\partial x'}\right|_0 = (C_{H0}\rho_e U_e - m_v\eta)(h_e - h_s) - \sigma\epsilon[T'(0)]^4 + \rho\, Cv(t)T'(0) - m_v H_T \quad [23]$$

Quasi-Steady-State Relations

For the quasi-steady-state solution, we let $\partial T'/\partial t = 0$ in Equation [21], integrate twice and evaluate the constants of integration from the boundary conditions

$$T'_*(0) = \text{surface temperature} \quad [24]$$

(Subscript * designates steady-state condition.)

$$T'_*(\infty) = 0 \quad [25]$$

The result is the familiar relation (5)

$$T'_*(x') = T'_*(0)\exp(-x'/\lambda) \quad [26]$$

The characteristic depth λ is given by

$$\lambda = K/v_{s*}\rho C \quad [27]$$

From Equation [10], we therefore get

$$q_*(s) = \rho Cv_{s*}T_*(s) = Cm_{s*}T_*(s) \quad [28]$$

and from Equation [14] we get

$$q'_*(0) = 0 \quad [29]$$

The heat stored in the body in the steady state is

$$H_* = \rho C\lambda T'_*(0) = T'_*(0)K/v_{s*} \quad [30]$$

from Equation [9].

These results indicate that in a practical case the heat flux into the surface of the body is initially equal to the net heat flux to a cold surface in either frame of reference. The heat flux into the body in the stationary frame of reference $q(s,t)$ decreases asymptotically to $cm_{s*}T_*(s)$ as time goes on and the steady state is approached. The heat flux into the body in the moving frame of reference $q'(0,t)$ asymptotically approaches zero as time goes on.

Induction Time for the Nonsteady Phase

The steady state of ablation represents a limit that is approached asymptotically, and the time to reach the steady state is therefore infinite. The characteristic time τ' for this transient nonsteady phase is sometimes taken as the ratio of the heat stored in the body to the heat input rate (5)

$$\tau' = \lambda\rho CT_*(s)/q(0,0) \quad [31]$$

There is another quantity, which we will call the induction time τ, that has considerable practical importance. It is the intercept, on the time axis, of the extrapolated steady-state position-vs.-time curve of the ablating surface. This is illustrated in Fig. 3.

The two quantities τ' and τ are equal in the special case where radiation losses from the surface and hot wall corrections for the aerodynamic heating are neglected. In this case, the total amount of heat q_c^* carried away from the body per unit mass of ablated material is constant for all time. The total sensible heat H per unit area which has accumulated in the body at any time t is then equal to the total heat flux $q(0,0)t$ into the body from the time heating started minus the total heat $\rho q_c^* s$ which has been carried away by ablation. Thus

$$H = q(0,0)t - \rho q_c^* s \quad [32]$$

After sufficiently long times, s is given by

$$s_*(t) = v_*(t - \tau) \quad [33]$$

and

$$H = q(0,0)t - \rho q_c^* v_*(t - \tau) = q(0,0)\tau \quad [34]$$

since

$$q(0,0) = \rho q_0^* v_* \quad [35]$$

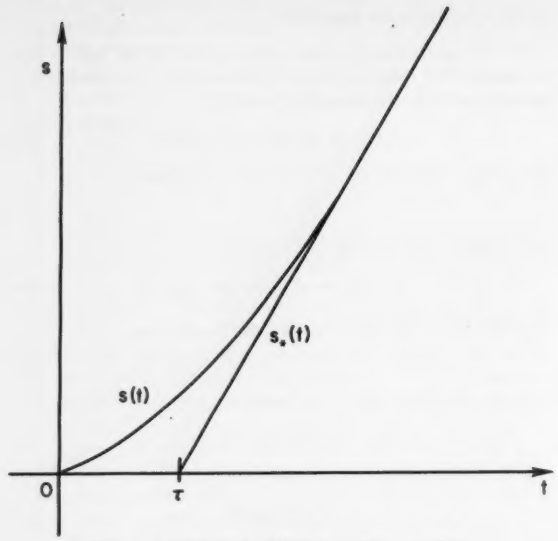

Fig. 3 Location of ablating surface vs. time

Thus the induction time τ is just the time which would be required to accumulate the heat stored in the steady-state temperature distribution of the body, if no heat were carried away by ablation.

Heat Transfer in the Porous Charred Layer

The heat transfer equation for the porous charred layer of the model we specified earlier can be written (in the stationary frame of reference) simply as (10)

$$\frac{\rho_l C_l \partial T_l}{\partial t} = \frac{K_l \partial^2 T_l}{\partial x_l^2} + C_{pg}\left[m_g - \rho_g\left(\frac{\rho_s - \rho_l}{\rho_s}\right)v_s\right]\frac{\partial T_l}{\partial x_l} \quad [36]$$

The second term on the right-hand side of the equation is simply the convective term for the gas flow. The heat capacity and conduction contributions of the gas are included in C_l and K_l.

The boundary conditions in the stationary frame of reference for the layer in our composite system (i.e., the layer plus the semi-infinite solid in back) are

$$q_l(s_l,t) = -K_l(\partial T_l/\partial x_l)_{x_l=s_l} \quad [37]$$

$$T_l(x_l,0) = 0 \quad [38]$$

$$-K_l(\partial T_l/\partial x_l)_{x_l=s_s} = q_s(s_s,t) + m_s\Delta H_c \quad [39]$$

where

$q_l(s_l,t)$ = heat flux in stationary frame of reference at front surface of the layer
$q_s(s_s,t)$ = heat flux at the front surface of the solid, i.e., heat flux into the solid body in the stationary frame of reference
ΔH_c = heat of charring the solid to form the gas and the layer material

For the boundary conditions at the back surface of the layer (Eq. [39]), we assume that the isothermal decomposition reaction

$$\text{solid} \xrightarrow[T'_s(0)]{\Delta H_c} \text{gas} + \text{layer} \quad [40]$$

occurs; and that the layer material is generated at the decomposition temperature (i.e., the front surface temperature of the solid). The consequence of this is that $T''_l(L) = T'_s(0)$. Therefore, the heat flux coming into the back surface from inside the layer is accounted for by ΔH_c and further heat transfer into the undecomposed solid.

Early in the ablation process, we will have $m_g = m_s = m = 0$, until the front surface of the solid reaches its decomposition temperature. Until this occurs, we will have only one solid phase, and the heat transfer situation will be that of a simple semi-infinite body subjected to a slowly changing heat flux.

For the boundary condition at the outside surface (i.e., Eq. [37]), we need to use relations like the ones in Equations [15–19 and 23]. In our present notation, these are

$$q_l(s_l,t) = (C_{H0}\rho_e U_e - m_{eT}\eta_T)(h_e - h_s) - \sigma\epsilon_l[T''_l(0,t)]^4 - \phi m_l \Delta H_l \quad [41]$$

$$-K_l\left[\frac{\partial T''_l(x''_l)}{\partial x''_l}\right]_{x''_l=0} = -K_l\left[\frac{\partial T_l(x_l)}{\partial x_l}\right]_{x_l=s} = q_l(s_l,t) \quad [42]$$

where

$$m_{eT} = m_g + \phi m \quad [43]$$

$$m_l = \rho_l v_l(t) \quad [44]$$

ϕ is the fraction of the layer material vaporized ($1 - \phi$ being eroded or otherwise lost without vaporizing).

The transformation of Equation [41] to the doubly primed frame of reference (that moves with the front face of the layer) is accomplished by means of equations like [13 and 14]. The result is

$$K_l\frac{\partial^2 T''_l}{\partial x''^2_l} + \left\{C_{pg}\left[m_g - \rho_g\left(\frac{\rho_s - \rho_l}{\rho_s}\right)(v_s - v_l)\right] + C_l m_l\right\}\frac{\partial T''_l}{\partial x''_l} = \rho_l C_l \frac{\partial T''_l}{\partial t} \quad [45]$$

$$q_l(s_l,t) = -K_l(\partial T''_l/\partial x''_l)_{x''_l=0} \quad [46]$$

$$T''_l(x''_l,0) = 0 \quad [47]$$

$$-K_l(\partial T''_l/\partial x''_l)_{x''_l=L} = q_s(s_s,t) + m_s\Delta H_c \quad [48]$$

The considerations discussed in the previous section apply to the solid back phase in our composite model, except for the boundary condition at the outside surface which is now determined by Equation [39] with

$$q_s(s_s,t) = -K_s[\partial T_s(x_s)/\partial x_s] \quad [49]$$

For both phases, then, the boundary condition at the interface is determined by an interaction with the phase adjacent to it.

Steady-State Solution

In the steady state, $\partial T''_l/\partial t$ is zero in Equation [45] for the charred layer. The steady-state solution $T''_{l*}(x_l)$ can then be obtained by two integrations and evaluation of the constants of integration from the specified boundary conditions (10).

The first integration gives us (after combining constants)

$$\left.\frac{\partial T''_l}{\partial x''_l}\right|_* = B\exp\left(\frac{-x''_l}{\delta_{l*}}\right) \quad [50]$$

$$\delta_{l*} = K_l/(m_{g*}C_{pg} + m_{l*}C_l) \quad [51]$$

which can be used in Equation [48] with the steady-state value of $q_s(s_s,t)$ given by Equation [28]. Converted to our present notation, the latter is a constant given by

$$q_{s*}(s_s,t) = C_s m_{s*} T_{b*} \quad [52]$$

where $T_{b*} = T'_{s*}(0)$, the steady-state back surface temperature of the layer. This yields the value of the overall constant B

$$B = -K_l^{-1} (C_s m_{s*} T_{b*} + m_{s*} \Delta H_c) \exp (L_*/\delta_{l*}) \quad [53]$$

A second integration yields the final result

$$T''_{l*}(x''_l) = A + B' \exp (-x''_l/\delta_{l*}) \quad [54]$$

where

$$B' = -B\delta_{l*} \quad [55]$$

For this composite model, the net aerodynamic heat input

$$q(\text{net}) = C_{H0}\rho_e(h_e - h_s) - \sigma\varepsilon_l[T''_l(0, t)]^4 \quad [64]$$

is

$$q(\text{net}) = q''(\text{body}) + \phi m_l \Delta H_l + m_s \Delta H_c + (m_l C_l + m_g C_{pg}) \times [T''(0) - T''(L)] + m_s C_s T'_s(0) + m_{cT}\eta_T(h_e - h_s) \quad [65]$$

where $q''(\text{body})$ is the rate at which heat is stored in the body in establishing the temperature distribution. The approach to the steady state can be represented by the condition

$$\lim_{t \to \infty} q'' \ (\text{body}) = 0$$

The steady-state heat of ablation is therefore

$$q^* = \frac{q_*(\text{net})}{m_{s*}} = \phi \left(\frac{m_{l*}}{m_{s*}}\right) \Delta H_l + \Delta H_c + \left[\left(\frac{m_{l*}}{m_{s*}}\right) C_l + \left(\frac{m_{g*}}{m_{s*}}\right) C_{pg}\right] [T_{w*} - T_{b*}] + C_s T_{b*} + \frac{\eta_T m_{cT*}}{m_{s*}} (h_e - h_s) \quad [66]$$

or

$$q^* = \phi \left(\frac{\rho_l}{\rho_s}\right) \Delta H_l + \Delta H_c + \left\{\left(\frac{\rho_l}{\rho_s}\right) C_l + \left[\frac{(\rho_s - \rho_l)}{\rho_s}\right] C_{pg}\right\} [T_{w*} - T_{b*}] + C_s T_{b*} + \frac{\eta_T m_{cT*}}{m_{s*}} (h_e - h_s) \quad [67]$$

The constant A can be evaluated at $x''_l = 0$ where $T''_{l*}(0) = T_{w*}$ is the steady-state surface temperature of the layer

$$A = T_{w*} - B' \quad [56]$$

Putting $x''_l = L_*$ in Equation [54] and combining with Equation [56], we get the relation which determines the steady-state wall temperature T_{w*} in terms of the decomposition temperature T_{b*}, the ablation rates and the other model parameters

$$T_{w*} = T_{b*} + B' [1 - e^{-L_*/\delta_{l*}}] \quad [57]$$

Equation [57] can be solved for L_* to give the result

$$L_* = \left(\frac{K_l}{m_{s*}}\right)\left(\frac{\rho_s}{\rho_l}\right)\left[C_{pg}\left(\frac{\rho_s}{\rho_l} - 1\right) + C_l\right]^{-1} \times \ln\left\{\frac{(T_{w*} - T_{b*})(\rho_l/\rho_s)[C_{pg}(\rho_s/\rho_l - 1) + C_l]}{(C_s T_{b*} + \Delta H_c)} + 1\right\} \quad [58]$$

after substitutions for B' and B from Equations [53 and 55]. It is evident from this result that the dependence of the steady-state thickness of the charred layer on external conditions is expressed by the fact that it is simply inversely proportional to the ablation rate m_{s*} since all other quantities in Equation [58] are parameters of the model.

Equation [54] can therefore also be written as

$$T''_{l*}(x''_l) = T_{w*} - \left[\frac{T_{w*} - T_{b*}}{1 - \exp(-L_*/\delta_{l*})}\right] [1 - e^{-x''_l/\delta_{l*}}] \quad [59]$$

In the steady state, the thickness of the layer L_* is a constant, and we also have the equality

$$v_{l*} = v_{s*} \quad [60]$$

Or, with the help of Equation [4], we can convert this to

$$\rho_s m_{l*} = \rho_l m_{s*} = m_{g*}\rho_l\rho_s(\rho_s - \rho_l)^{-1} \quad [61]$$

We also have the relation

$$m_{s*} = m_{g*} + m_{l*} \quad [62]$$

The steady-state temperature distribution in the solid is the same as that obtained in the section "Quasi-Steady-State Relations" (3). In our composite model notation, this is

$$T'_s(x'_s) = T_{b*} \exp [-x'_s v_{s*}\rho_s C_s/K_s] \quad [63]$$

From the practical standpoint, it is to be hoped that Equations [58 and 67] can be used in calculating engineering estimates of important ablating properties of plastic-containing heat shield materials. Data on the various parameters in these equations are presently not available. This points up the need for experimental studies to provide such data and to create a better understanding of how they are related to other material properties so that approximate values can be estimated without recourse to elaborate measurements. The present formulation develops the basic concepts, but is not necessarily complete in all details. It should serve as the basis for refinements of further research.

Induction Time for the Composite Model

The induction period, defined previously for a system vaporizing without layer formation, is also applicable to more complex models, such as the one under discussion. We will now deduce the corrections to Equation [34] that are needed for the present model of ablation.

For this purpose, we will start with the heat conduction equation in a coordinate system fixed with respect to the ablating surface

$$\frac{\partial}{\partial t}(\rho_b h_b) = \frac{\partial}{\partial x}\left[K_b \frac{\partial T}{\partial x} + (\rho_b h_b v_l + \rho_g h_g v_g)\right] \quad [68]$$

This is a generalized equation which reduces to Equation [45] for the charred layer and Equation [21] for the original solid. In this equation, the enthalpy of the gas $\rho_g h_g$ is neglected in comparison to the enthalpy $\rho_b h_b$ of the solid material of the body, and v_l (the velocity of the wall) is neglected in comparison to v_g (the velocity of the gas). Conservation of mass provides the relation

$$\rho_g v_g = (\rho_s - \rho_b) v_s \quad [69]$$

where v_s is the velocity of propagation of the charred layer in the laboratory coordinate system. In our present model of the ablation process, the density of the solid body is a step function, equal to ρ_s in the undecomposed material and to ρ_l in the charred layer.

It is also of interest to obtain the equation for the total heat H stored in the body, above that originally present. This quantity is related to the specific enthalpy of the body by the definition

$$H \equiv \int_0^\infty (\rho_b h_b - \rho_s h_0) dx \quad [70]$$

so that, by integrating Equation [68] over x, one obtains

$$\frac{dH}{dt} = -K_l \left.\frac{\partial T}{\partial x}\right|_{x=0} - [(\rho_l h_{b_w} - \rho_s h_{b_0})v_l + (\rho_s - \rho_l)h_{g_w} v_s] \quad [71]$$

The boundary condition at the ablating surface is (neglecting radiation losses)

$$-K_l \left.\frac{\partial T}{\partial x}\right|_{x=0} = q - \rho_l v_l[h_v + \eta(h_s - h_s)] - (\rho_g v_g)_{x=0}\, \eta_g (h_s - h_s) \quad [72]$$

where

q = aerodynamic heat flux to surface in the absence of ablation

$\rho_l v_l[h_v + \eta(h_s - h_s)]$ = amount that this heat flux is reduced by vaporization and transpiration of the solid material in the charred layer

$\rho_g v_g \eta_g (h_s - h_s)$ = amount heat flux is reduced by transpiration of gaseous decomposition products formed during charring

It is assumed that all the ablated material is vaporized and that the radiation and hot wall effects are unimportant. Combining Equations [69, 71 and 72] gives

$$q = v_l\{\rho_l[h_v + \eta(h_s - h_s) + h_{b_w}] - \rho_s h_{b_0}\} + (\rho_s - \rho_l)v_s[\eta_g(h_s - h_s) + h_{g_w}] + dH/dt \quad [73]$$

The "intercept" induction time as defined earlier and in Fig. 3, is

$$\tau = \int_0^\infty \left(1 - \frac{v_l}{v_{l*}}\right) dt \quad [74]$$

where the integration begins at the time the heat flux q is turned on. The steady-state ablation velocity v_{l*} can be obtained from Equation [73], since in the steady-state $dH/dt = 0$ and $v_s = v_l = v_{l*}$. Substitution of the value of v_{l*} so obtained into Equation [74] gives

$$\tau = \int_0^\infty \frac{1}{q}\left(q - v_l\{\rho_l[h_v + \eta(h_s - h_s) + h_{b_w}] - \rho_s h_{b_0} + (\rho_s - \rho_l)[\eta_g(h_s - h_s) + h_{g_w}]\}\right)dt \quad [75]$$

After a substitution for q from Equation [73], this reduces to

$$\tau = \int_0^\infty \frac{1}{q}\left\{(\rho_s - \rho_l)(v_s - v_l)\,[\eta_g(h_s - h_s)] + h_{g_w} + \frac{dH}{dt}\right\} dt \quad [76]$$

If we neglect the time dependence of the surface temperature, Equation [76] reduces to

$$\tau = \frac{1}{q}(\rho_s - \rho_l)\,[\eta_g(h_s - h_s) + h_{g_w}]\,L_* + \frac{H_*}{q} \quad [77]$$

Here $L_* = \int_0^\infty (v_s - v_l)dt$ is the thickness of the charred layer in the steady state, and H_* is the heat stored in the body in the steady state. H_* may be evaluated from the steady-state heat conduction equation (i.e., Eq. [68] with the left-hand side set equal to 0)

$$\frac{d}{dx}\left\{K_b \frac{dT_*}{dx} + [\rho_b h_b v_{l*} + (\rho_s - \rho_b)\, h_g v_{l*}]\right\} = 0 \quad [78]$$

or

$$K_b \frac{dT_*}{dx} + [\rho_b h_b v_{l*} + (\rho_s - \rho_b)h_g v_{l*}] = \text{constant} \quad [79]$$

The constant may be evaluated from conditions at $x = \infty$ and is equal to $\rho_s h_{b_0} v_{l*}$; hence we have

$$(\rho_b h_b - \rho_s h_{b_0})v_{l*} = -K_b(dT_*/dx) - (\rho_s - \rho_b)h_g v_{l*} \quad [80]$$

Integrating over x and using Equation [70], we get

$$H_* = \frac{1}{v_{l*}}\int_{T_0}^{T_{w*}} K_b dT - (\rho_s - \rho_l)\int_0^{L_*} h_g dx \quad [81]$$

so that the induction time is

$$\tau = \frac{1}{q v_{l*}}\int_{T_0}^{T_{w*}} K_b dT + \frac{1}{q}(\rho_s - \rho_l) \times \left[\eta_g(h_s - h_s)L_* + \int_0^{L_*}(h_{g_w} - h_g)\, dx\right] \quad [82]$$

Physically, Equation [82] shows that the induction time τ is the sum of two terms; the first of these is simply the induction time for a material which does not char; the second is the additional time required to supply the heat carried off by the gases evolved from the charred layer. The factor $(\rho_s - \rho_l)L_*$ in this term is the mass of the evolved gases per unit area; the factor $[\eta_g(h_s - h_s) + (1/L_*)\int_0^{L_*}(h_{g_w} - h_g)\, dx]$ is the average enthalpy absorbed by these gases per unit mass.

It is of interest to note that we have made no assumptions about the way in which the body approaches the steady state, and that in fact the induction time (Eq. [82]) depends only on the final state of the system and not at all on the way in which this final state is attained. This is a consequence of the definition of τ which depends only on the asymptotic steady-state line $S_*(t)$ in Fig. 3 and not on how the asymptote is approached. Physically, this result is due to the fact that we have assumed that the amount of heat carried away by each bit of ablating material is independent of surrounding conditions, so that the total heat required to establish any state of the system does not depend on the path by which that state is reached. If radiative or hot wall effects were considered, or if the fraction of ablated material which vaporized varied with time, this would no longer be true, and it would not be possible to obtain as simple a formula as Equation [82] for the induction time.

Acknowledgments

The authors are indebted to Drs. W. L. Bade, H. Bethe, S. Georgiev, R. John and H. L. Schick for many helpful discussions and advice. The work was supported by the U. S. Air Force under Contract AF 04(647)-305.

Nomenclature

$*$	= steady state when used as a subscript
C_{H_0}	= Stanton number
C_l	= heat capacity of the layer material (including gases in it)
C_{pg}	= constant-pressure heat capacity of the gaseous decomposition products
C_s	= heat capacity of the original solid
ΔH_c	= heat of decomposition of the original solid to form gas and charred layer
ΔH_l	= heat of vaporization (or decomposition) of the charred layer per unit mass
ϵ	= total emissivity of the solid surface
ϵ_l	= total emissivity of the surface of the layer
h_b	= specific enthalpy of the body
h_e	= stagnation specific enthalpy of gas at the edge of the boundary layer
h_0	= specific enthalpy of the solid under initial conditions
h_s	= specific enthalpy of gas at surface of body
k_l	= thermal diffusivity of the layer with $m_g = 0$
k_s	= thermal diffusivity of the solid
K_l	= thermal conductivity of the layer with $m_g = 0$
K_s	= thermal conductivity of the solid

L = thickness of charred layer
m_g = mass rate of gas formation
m_l = mass rate of ablation at front of layer
m_s = mass rate of decomposition of the original solid
m_{sT} = $m_g + \phi m_l$
η_g = transpiration coefficient for gaseous decomposition products alone
η_T = transpiration coefficient for mixture of all gases produced (i.e., from decomposition of solid and vaporization of layer)
q^* = steady-state heat of ablation
$q(x, t)$ = heat flux in stationary frame of reference at station x and time t
$q_s(s_s, t)$ = heat flux into undecomposed solid in the stationary frame of reference
$q'_s(x'_s, t)$ = heat flux in primed frame of reference at station x'_s in the solid at time t
$q''_l(x''_l, t)$ = heat flux in doubly primed frame of reference at station x''_l in the layer and at time t
ρ_b = density of the body (equal to ρ_s in original solid and ρ_l in charred layer)
ρ_l = bulk density of charred layer
ρ_s = density of original solid
σ = Stefan-Boltzmann radiation constant
s_l = location of front surface of layer in stationary coordinate system
s_s = location of back surface of layer (i.e., front surface of original solid)
t = time
τ = induction period of nonsteady phase of ablation
T_e = temperature of the gas at the edge of the boundary layer
T_v = vaporization temperature
T_w = temperature of the gas in the boundary layer at the wall, also temperature of front surface of layer (wall temperature)
$T_l(x_l, t)$ = temperature in stationary frame of reference at station x_l in layer at time t
$T_s(x_s, t)$ = temperature in stationary frame of reference at station x_s in solid at time t
T'_s, X'_s = temperature-position coordinate axes moving with the back surface of the layer (i.e., the front surface of the original solid)
$T'_s(x'_s, t)$ = temperature in primed frame of reference at station x'_s in the solid at time t
T''_l, X''_l = temperature-position coordinate axes moving with the surface of the layer
$T''_l(x''_l, t)$ = temperature in doubly primed frame of reference at station x''_l in layer at time t
U_e = velocity of gas at edge of boundary layer
v_g = velocity of the ablating gas
v_l = velocity of front surface of layer (velocity of the wall)
v_s = velocity of back surface of layer (front surface of original solid)
x_l = coordinate along surface normal in layer in stationary frame of reference
x'_s = coordinate along surface normal in T'_s, X'_s frame of reference
x''_l = coordinate along surface normal in T''_l, X''_l frame of reference

References

1 Gruntfest, I. J. and Shenker, L. H., "Behavior of Materials at Very High Temperatures," *Ind. Engng. Chem.*, vol. 50, 1958, p. 75A.

2 Gruntfest, I. J. and Shenker, L. H., "Behavior of Reinforced Plastics at Very High Temperatures," *Modern Plastics*, vol. 35, 1958, p. 155.

3 Gruntfest, I. J., Shenker, L. H. and Saffire, V. N., "Behavior of Reinforced Plastics at Very High Temperatures—Part 2," *Modern Plastics*, vol. 36, 1959, p. 137.

4 Weinbaum, S. and Wheeler, H. L., Jr., "Heat Transfer in Sweat-Cooled Porous Metals," *J. Appl. Phys.*, vol. 20, 1949, p. 113.

5 Landau, W. G., "Heat Conduction in a Melting Solid," *Quart. Appl. Math.*, vol. 8, 1950, p. 81.

6 Condon, E. U. and Odishaw, H., "Handbook of Physics," McGraw-Hill Publishing Co., N. Y., 1958, pp. 3–4, 5–71.

7 Lees, L., "Convective Heat Transfer With Mass Addition and Chemical Reactions," paper presented at Third Combustion and Propulsion Colloquium, AGARD, NATO, Palermo, Sicily, March 17–21, 1958.

8 Fledderman, R. G., "Heat Transfer to a Vaporizing, Ablating Surface," *J. Aero/Space Sci.*, vol. 26, 1959, p. 604.

9 Fay, J. A., Riddell, F. R. and Kemp, N. H., "Stagnation Point Heat Transfer in Dissociated Air Flow," JET PROPULSION, vol. 27, no. 6, June 1957, p. 672.

10 Mayer, E. and Bates, J. G., "Transpiration Cooling in Porous Metal Walls," JET PROPULSION, vol. 24, 1954, p. 366.

1960-61 ARS Meeting Schedule

Date	Meeting	Location	Abstract Deadline
Sept. 27–30	Power Systems Conference	Santa Monica, Calif.	Past
Oct. 10–12	Human Factors and Bioastronautics Conference	Dayton, Ohio	Past
Nov. 3–4	Electrostatic Propulsion Conference	Monterey, Calif.	Past
Dec. 5–8	ARS Annual Meeting and Astronautical Exposition	Washington, D.C.	Past
Feb. 1–3	Solid Propellant Rocket Conference	Salt Lake City, Utah	Sept. 30
March 13–15	Testing Conference	Los Angeles, Calif.	Oct. 17
April 5–7	Lifting Re-Entry Vehicles: Structures, Materials, and Design Conference	Palm Springs, Calif.	Oct. 31
April 26–28	Detonation and Deflagration Phenomena Conference	Palm Beach, Fla.	Nov. 28
May 22–24	National Telemetering Conference	Chicago, Ill.	Jan. 16
June 7–9	ARS Semi-Annual Meeting	Los Angeles, Calif.	Feb. 1
Aug. 21–23	International Hypersonics Conference	Cambridge, Mass.	
Aug. 23–25	Biennial Gas Dynamics Symposium	Evanston, Ill.	
Oct. 9–13	ARS SPACE FLIGHT REPORT TO THE NATION	New York, N.Y.	May 2

Send all abstracts to Meetings Manager, ARS, 500 Fifth Ave., New York 36, N.Y.

Measurements of Heat Transfer and Friction Coefficients for Helium Flowing in a Tube at Surface Temperatures up to 5900 R

MAYNARD F. TAYLOR[1] and THOMAS A. KIRCHGESSNER[2]

NASA,
Lewis Research Center
Cleveland, Ohio

Measurements of average heat transfer and friction coefficients and local heat transfer coefficients were made with helium flowing through electrically heated smooth tubes with length-diameter ratios of 60 and 92 for the following range of conditions: Average surface temperature from 1457 to 4533 R, Reynolds number from 3230 to 60,000, heat flux up to 583,200 Btu per hr per ft^2 of heat transfer area, and exit Mach number up to 1.0. The results indicate that, in the turbulent range of Reynolds number, good correlation of the local heat transfer coefficients is obtained when the physical properties and density of helium are evaluated at the surface temperature. The average heat transfer coefficients are best correlated on the basis that the coefficient varies with $[1 + (L/D)^{-0.7}]$ and that the physical properties and density are evaluated at the surface temperature. The average friction coefficients for the tests with no heat addition are in complete agreement with the Kármán-Nikuradse line. The average friction coefficients for heat addition are in poor agreement with the accepted line.

THE IMPORTANCE of nuclear reactors as a power source for aircraft and space vehicles has stimulated interest in convective heat transfer from high temperature surfaces. The resulting large ratio of fuel element temperature to working fluid temperature means a large variation in the properties of the fluid, which influence the heat transfer characteristics. Some work has been done with wall temperatures up to 3460 R using air (1).[3] Heat transfer coefficients for helium flowing through a carbon tube with a maximum inside surface temperature of 5040 R and a corresponding gas temperature of 4640 R are presented in (2).

In order to extend the range of surface temperature reported in (1) and the ratio of surface to fluid bulk temperature of (2), the present investigation was undertaken. In this investigation the wall temperatures were increased to the limit of the tungsten and molybdenum test sections, and the ratio of surface to fluid bulk temperature was kept as high as possible.

Experimental Apparatus

Arrangement

A schematic diagram of the arrangement of the test section and equipment used in the investigation is shown in Fig. 1. The mixing tanks and test section were housed in a steel containment tank, which was evacuated to about 50 μ of mercury. This was done to minimize oxidation of the refractory metals of the test sections. Pressures lower than 50 μ of mercury were possible but would have resulted in evaporation of the hot metals.

Test Sections

Since the object of this investigation was to obtain heat transfer data at as high a surface temperature as possible, this experiment embraced a number of materials problems. There are only five known metals with melting points above 5000 R: Molybdenum, osmium, tantalum, rhenium and tungsten, in order of increasing melting points. All five materials are subject to rapid oxidation when heated in air. For reasons of availability and high melting point, molybdenum and tungsten were chosen as test section materials. Since molybdenum tubes were available commercially, they were used for the first high temperature tests. Several tubes were made by disintegrating holes through tungsten rods, which were then ground to a uniform wall thickness. Nickel entrance and molybdenum exit flanges were used to connect the test sections to the mixing tanks. The molybdenum test section was equipped with a bellmouth entrance. A right-angle edge approach was used for the tungsten test section entrance. In addition to the refractory metal test sections, a well-instrumented Inconel test section was used to make several runs to check the high temperature heat transfer results.

The dimensions of the various tubes used as test sections in this investigation are shown in Table 1.

Table 1 Dimensions of tubes used as test sections in this investigation

Tube material	ID, in.	OD, in.	Heat transfer length L, in.	L/D
molybdenum	0.191	0.250	11.5	60
tungsten	0.125	0.250	11.5	92
Inconel	0.124	0.188	11.25	91

Presented at the ARS Semi-Annual Meeting, June 8–12, 1959, San Diego, Calif.

[1] Research Engineer. Member ARS.

[2] Research Engineer.

[3] Numbers in parentheses indicate References at end of paper.

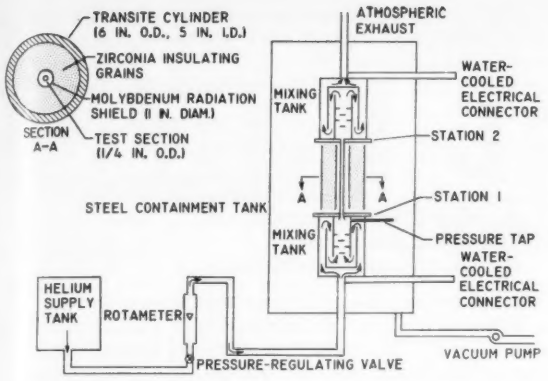

Fig. 1 Schematic diagram showing arrangement of test apparatus

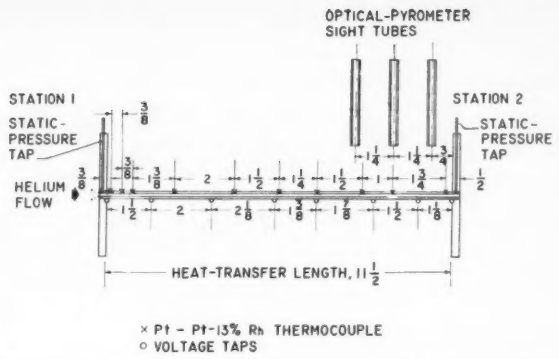

Fig. 2 Typical test section. Thermocouple, optical pyrometer, voltage tap and pressure tap locations shown are for molybdenum test section. (All dimensions in inches)

Instrumentation

The outside wall temperatures of the molybdenum and tungsten test sections were measured with platinum-platinum-13-per cent-rhodium thermocouples spotwelded along the length of the test section and located as shown in Fig. 2. For test section temperatures beyond the range of the thermocouples, a small target optical pyrometer was used. The use of the optical pyrometer is discussed in the Appendix. Some experimentation with tungsten-molybdenum thermocouples was conducted, but the extreme brittleness of the tungsten wire after welding made the use of this thermocouple impractical. The Inconel test section wall temperatures were measured with Chromel-Alumel thermocouples.

The gas temperature was measured before entering and after leaving the test section with platinum-platinum-rhodium thermocouples located downstream of the baffles in the two mixing tanks.

The radiation shield and outside surface of the Transite insulating cylinder were instrumented with platinum-platinum-rhodium thermocouples. Molybdenum wires were spotwelded along the length of the test section to measure voltage drop as a function of distance from the entrance. Static pressure taps were located in the entrance mixing tank and in the entrance and exit flanges of the molybdenum test section. Voltage and static pressure tap locations are shown in Fig. 2. The flanges of the tungsten test section were not instrumented with pressure taps because of the difficulty in getting small holes through the molybdenum flange and the walls of the tungsten tube.

The molybdenum test section was used in obtaining both friction factor and local and average heat transfer data. Since the tungsten test section was not instrumented with voltage or pressure taps, it was used only in obtaining average heat transfer data. The range of conditions for which data were obtained is summarized in Table 2.

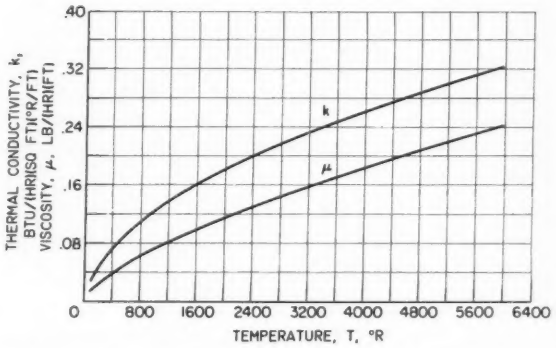

Fig. 3 Variation of thermal conductivity and absolute viscosity of helium with temperature

Method of Calculation

Helium Properties

The variable physical properties of helium used in calculating the Nusselt, Reynolds and Prandtl numbers are shown in Fig. 3 as a function of temperature. In the absence of experimental data, the curves in Fig. 3 were calculated by the methods shown in (3, 4 and 5). The value of specific heat c_p is 1.24 Btu/(lb)(R) and is constant; the ratio of specific heats γ is 1.667, and the gas constant R is 386 ft-lb/(lb)(R).

Friction Coefficients

The average friction coefficient f was calculated by the

Table 2 Summary of range of conditions for which data were obtained

Test section material	Bulk Reynolds number Re_b	Average surface temperature T_s, R	Exit Mach number	Heat flux, Btu/(hr) (ft²)
molybdenum	3750–60,000	530	0.09–0.97	adiabatic
molybdenum	3230–25,230	1457–2334	0.21–0.95	73,100–300,000
tungsten	5375–11,000	1905–4533	0.72–1.0	169,600–383,500
Inconel	15,340–35,100	1606–2057	...	272,400–583,200

method used in (1) wherein

$$f = \frac{\Delta p_{fr}}{4(L/D)(\rho_{av}V^2/2g)} = \frac{g\rho_{av}\Delta p_{fr}}{2(L/D)G^2} \quad [1]$$

where the density ρ_{av} was evaluated at the average static pressure and temperature of the gas as follows

$$\rho_{av} = \frac{1}{R}\left(\frac{p_1 + p_2}{t_1 + t_2}\right) \quad [2]$$

The average friction coefficient was also calculated with the density evaluated at the film temperature, as shown in (1).

Heat Transfer Coefficient

The average heat transfer coefficient h_{av} was computed from the experimental data by the relation

$$h_{av} = \frac{Q}{S(T_s - T_b)} = \frac{wc_{p,b}(T_2 - T_1)}{S(T_s - T_b)} \quad [3]$$

where the temperature of the gas T_b was taken as the arithmetric mean of the total temperatures at the entrance T_1 and the exit T_2 of the test section. The average surface temperature T_s was taken as an integrated average of the local outside wall temperature minus the temperature drop through the wall. The temperature drop through the wall was calculated by the following equation, which is derived in (6)

$$T_s = T_w - \frac{Q}{2\pi Lk_t(r_0^2 - r_i^2)}\left(r_0^2 \ln \frac{r_0}{r_i} - \frac{r_0^2 - r_i^2}{2}\right) \quad [4]$$

where

T_w = average outside wall temperature
k_t = thermal conductivity of the tube material
r_i, r_0 = inside and outside radii of the test section, respectively

In this investigation the temperature drop calculated by Equation [4] was very small compared with the difference between the average inside wall temperature and the helium bulk temperature.

Because the test section temperatures were very high, it was expected that the heat loss to the surroundings would be large. For most runs, less than 20 per cent of the heat generated was lost, according to calculations by the following equation

$$Q_l = Q_e - Q \quad [5]$$

where

Q_l = heat loss to the surroundings
Q_e = electrical heat input
Q = heat transferred to the gas

Most of the heat loss could be accounted for.

It was possible to calculate local heat transfer coefficients by evaluating the various heat losses and then making a heat balance for each increment. The heat loss at the ends of the test section and the radial heat loss for each increment were calculated. These losses accounted for more than 80 per cent of the total heat loss calculated by Equation [5]. Each local heat loss and the end losses were increased by the ratio of total heat loss to the sum of local and end heat losses. The rates of incremental electrical heat generation and heat conduction into and away from each increment were calculated and used along with the heat losses to set up a heat balance for each increment. From this heat balance the rate of heat transfer to the gas could be calculated for each increment. Starting at the entrance of the test section, the bulk temperature of the gas leaving the first increment could be calculated. This was repeated for each succeeding increment. The local bulk temperature and local surface temperature were used to calculate a local heat transfer coefficient. The local and average heat transfer coefficients were used to calculate Nusselt numbers.

Results and Discussion

Axial Wall Temperature Distribution

Three representative axial outside wall temperature distributions for the tungsten test section showing thermocouple and optical pyrometer temperature measurements appear in Fig. 4. The experimental data as indicated are summarized in Table 3. (*Continued on page 889*)

Table 3 Experimental results

Run	Q_e/S, Btu/(hr) (ft²)	Q/S, Btu/(hr) (ft²)	w, lb/hr	p_1, lb/ft² abs	p_2, lb/ft² abs	T_1, R	T_2, R	T_b, R	T_s, R
				Molybdenum test section					
1	93,200	73,100	3.0	2374	2099	580	1514	1047	2259
2	132,200	109,200	7.5	2976	2056	565	1130	848	1738
3	187,000	173,500	14.5	4305	2063	560	1021	791	1497
4	266,000	208,000	19.2	5349	2088	560	978	769	1457
5	191,000	159,200	7.6	3202	2093	572	1383	978	2257
6	362,500	300,000	5.9	5674	2198	560	1193	871	2334
				Tungsten test section					
7	227,000	169,600	5.0	...	...	615	1465	1040	1905
8	461,500	307,000	7.2	...	...	620	1690	1155	2499
9	753,000	383,500	7.9	...	...	650	2278	1464	3418
10	1,145,000	362,500	4.6	...	...	745	2720	1732	4533
				Inconel test section					
11	324,000	275,400	9.6	...	...	530	1230	880	1606
12	320,500	272,400	8.5	...	...	535	1310	923	1688
13	520,000	457,200	16.8	...	...	530	1192	861	1652
14	522,000	486,800	18.4	...	...	525	1165	845	1584
15	600,000	551,700	17.3	...	...	525	1300	912	1869
16	599,000	516,900	15.3	...	...	530	1350	940	1921
17	652,000	583,200	15.7	...	...	526	1430	978	2057